



Uit

NORGES
ARKTISKE
UNIVERSITET

Faculty of Science and Technology
Department of Geosciences

Glacial dynamics and fluid flow processes in Bjørnøyrenna and the Loppa High area, SW Barents Sea

Tor Geir Ødegård Garpestad

Master thesis in Geology, GEO-3900

May 2020



Abstract

During the Late Weichselian glaciation, the Bjørnøyrenna ice stream was the main outlet of the Barents Sea Ice Sheet. In this thesis, a 3D seismic dataset from the Loppa High, located in the main ice stream trunk, has been used to study the glacial sediment package, revealing details on pastglacial dynamics, fluid flow processes and gas hydrate formation.

Three seismic horizons have been interpreted: the seabed, an intra Quaternary horizon and the Upper Regional Unconformity (URU), which corresponds to the base of the Quaternary glacial sediment package. On the intra Quaternary horizon, megascale glacial lineations (MSGSL) and a glacitectonic line of depressions are observed, 10 km apart. The MSGSL are suggested to indicate fast flowing ice and a warm based bed while the glacitectonic line of depressions indicate cold base and slow ice flow velocities. Seismic indications of fluid flow and gas hydrate formation are associated with the glacitectonic line of depressions. We therefore suggest that gas hydrate formation promoted the freeze-on of subglacial material to the base of the ice stream, triggering glacitectonic erosion, excavating the line of depressions. On URU, bedrock ridges and a subglacial meltwater channel are interpreted. The meltwater channel follows the outline of the Bjørnøyrenna Fault Complex which is suggested to be a weakness zone prone to glacial and meltwater erosion. The subglacial meltwater channel is proposed to have accelerated the flow of the overlying ice due to lower basal drag. The surrounding areas on URU consist of bedrock ridges. Their formation is attributed to the differential resistance to glacial erosion of alternating soft and hard interbeds in the underlying bedrock. It is suggested that this created a rough subglacial bed, and this, together with the fact that no landforms indicative of fast flowing ice are observed associated with these bedrock ridges, is consistent with slower ice flow velocities in this area compared to within the meltwater channel.

Table of Contents

1	Introduction	1
1.1	Objectives	1
1.2	Study Area	2
1.3	Tectonic evolution of the SW Barents Sea	4
1.3.1	Paleozoic	4
1.3.2	Mesozoic	5
1.3.3	Cenozoic	6
1.4	Glacial history of the Barents Sea and Bjørnøyarena	8
1.4.1	The first Glaciations (Paleogene and Neogene)	8
1.4.2	Pleistocene	8
1.4.3	Late Weichselian Glaciation	9
1.4.4	Deglaciation of the Late Weichselian glaciation in the SW Barents Sea	12
1.5	Glacier dynamics and landforms in the SW Barents Sea	15
1.5.1	Ice Streams	15
1.5.2	Sticky spots	16
1.5.3	Grounding zone wedges (GZW)	17
1.5.4	Iceberg ploughmarks	20
1.5.5	Glacitectonics	22
1.6	Gas hydrates and Fluid Flow	27
1.6.1	Gas hydrates	27
1.6.2	Fluid Flow	29
2	Data and methods	33
2.1	Dataset	33
2.2	Seismic reflection theory	33
2.3	Seismic resolution	34

2.3.1	Vertical resolution	35
2.3.2	Horizontal resolution.....	36
2.3.3	Vertical and horizontal resolution of the DN14001 survey	38
2.4	Interpretation tools and methods	39
2.4.1	Seismic attributes	40
2.5	Artefacts.....	40
3	Results	42
3.1	Seabed horizon	42
3.1.1	Curved Lineations on the Seabed: Description	44
3.1.2	Curved lineations on the Seabed: interpretation	46
3.2	Upper regional unconformity (URU)	47
3.2.1	Curved ridges: description	50
3.2.2	Curved ridges on the URU surface: interpretation.....	51
3.2.3	Elongated depression.....	51
3.2.4	Elongated depression: interpretation	53
3.2.5	Streamlined Lineations within the Elongated: depression	54
3.2.6	Streamlined lineations within the Elongated: Interpretation.....	55
3.2.7	Circular basin within the elongated depression: Description.....	56
3.2.8	Circular basin within elongated depression: interpretation.....	57
3.2.9	Circular depressions on the URU surface: Description	57
3.2.10	Circular depressions on URU: interpretation	62
3.3	RMS amplitude anomalies along URU surface (bright spots)	63
3.3.1	Bright spots along bedrock ridges: description	64
3.3.2	Bright spots along the bedrock ridges: Interpretation	65
3.3.3	Bright spots related to elongated depression: description.....	66
3.3.4	Bright spots elongated depression: interpretation	68
3.3.5	Bright spots related to circular depressions: description.....	69

3.3.6	Bright spots related to circular depressions: interpretation	69
3.4	Intra Quaternary Horizon.....	69
3.4.1	Curved lineations on the intra Quaternary horizon: description	71
3.4.2	Curved lineations on the intra Quaternary horizon: interpretation	72
3.4.3	Streamlined lineations on the intra Quaternary horizon: description.....	72
3.4.4	Streamlined lineation on the intra-Quaternary horizon: interpretation	73
3.4.5	Line of depressions: description.....	74
3.4.6	Line of depressions: Interpretation.....	76
3.5	RMS amplitude anomalies along the intra horizon surface.....	76
3.5.1	Bright spots related to iceberg ploughmarks: Description	76
3.5.2	Bright spots related to iceberg ploughmarks: Interpretation	77
3.5.3	Bright spots in central parts.....	77
3.5.4	Bright spots in central parts of the intra Quaternary horizon: Interpretation	78
4	Discussion	79
4.1	Observed landforms on URU and Intra-Quaternary horizon	79
4.1.1	Bedrock ridges on URU	79
4.1.2	Elongated depression on URU	81
4.1.3	Contrasting ice flow velocities on URU	83
4.1.4	Line of depressions and MSGL on the Intra Quaternary horizon	85
4.2	Regional ice dynamics of the Bjørnøyrenna ice stream	93
4.2.1	URU	93
4.2.2	Intra Quaternary horizon:	95
5	Conclusion.....	99
	References	101

List of Tables

Table 1 Acoustic velocity, frequency, wavelength and vertical resolution for the two surfaces Intra horizon and URU	39
Table 2 Diameters and relief of circular depressions	59

List of Figures

Figure 1 Bathymetric map of the SW Barents Sea. 3D seismic dataset DH 14001 is marked as a red rectangle. White lines represent geological structures of the Barents Sea, where Loppa High (LH), Bjørnørenna Fault Complex (BFC) and Bjørnøya Basin (BB) is marked in white. Bathymetric map from IBCAO version 3.0. Structural map from NPD-FactMaps.....	3
Figure 2 Paleogeographic map of the Barents Sea in late Cenozoic, illustrating erosion of the Barents Sea. Highest erosion during the late Cenozoic occurred in the area of Svalbard. Red square marks the study area. Figure modified from Worsley, (2008).....	7
Figure 3 LGM, illustrating the British-Irish Ice Sheet (BIIS) Scandinavian Ice Sheet (SIS) and the Svalbard Barents Kara Ice sheet (SBKIS), in this thesis referred to as the Barents Sea Ice Sheet (BSIS). Figure from Hughes et al,(2016)	10
Figure 4 a) Ice flow direction based on them mapping of mega scale glacial linations and a isopach map of the Bjørnøyrenna TMF. b) profile across the Bjørnøyrenna TMF showing the three glacial sediment units GI, GII and GIII. Figure from (Andreassen & Winsborrow, 2009)	12
Figure 5 Deglaciation of the southern Barents Sea devided into five stages. Dataset DN 14001 is marked in red. Figure modified from Winsborrow et al., (2010).....	15
Figure 6 Bathymetric map from Håkjerringdjupet, showing landforms indicating fast flowing ice (MGSL) and glacitectonic landforms indicating slower flowing ice (Source depressions and rafted sediments). Figure from (Winsborrow et al., 2016).....	17
Figure 7 Seismic profile of a grounding zone wedge parallel and perpendicular to the ice flow direction. Figure from Dowdeswell & Fugelli, (2012)	19
Figure 8 Large singular groves and parallel grove sets from Strofjordrenna interpreted as ice berg scour marks. Figure from (Shackleton et al., 2020).....	21
Figure 9 Table of lithological borehole properties. Unit G1 show glaciteconic structures of Cretaceous sedimentary rock in between two units of till. Figure from (Sættem et al., 1992).	22
Figure 10 Hill-hole pair cartoon. Figure from (Evans & Wilson, 2006)	23
Figure 11 Composite ridges cartoon. Figure from (Benn & Evans, 2014)	24

Figure 12 Cupola hills cartoon. Figure from (Benn & Evans, 2014).....	25
Figure 13 Rafts and megablocks cartoon. Figure from (Benn & Evans, 2014).....	26
Figure 14 BSR reflector, figure modify from (Shipley, 1979).....	27
Figure 15 Interpreted BSR in the SW Barents Sea and how they appear in a seismic section. Red square marks dataset DH14001. Figure modified from Vadakkepuliambatta et al., (2017)	29
Figure 16 Indicators of fluids in a hydrocarbon reservoir. Figure from (Løseth et al., 2009) .	30
Figure 17 Indicators of vertical fluid migration. Figure modified from Petersen et al., (2010)	31
Figure 18 Pockmarks and flairs detected on the seabed in the Loppa High area, SW Barents Sea. Figure from (Chand et al., 2012)	32
Figure 19 General relation between depth and frequency, velocity and wavelength. Figure modified from Brown, (2011).	35
Figure 20 Wedge model illustrating interference effect between two high layers of different velocity. Figure modified from Badley & Gibson, (1987).....	36
Figure 21 illustrating the Fresnel zone, Figure modified by Sheriff, (1985).	37
Figure 22 illustrate the Fresnell zone pre and post migration	37
Figure 23 illustrate how midpoints are organized in bins and stacked to improve the signal to noise ratio. The horizontal resolution of a 3D seismic survey equals the bin size. Figure modified from Liner, (1999)	38
Figure 24 Peak frequency analysis for URU and intra Quaternary horizon.	39
Figure 25 Artefacts that can be seen on all three surfaces	41
Figure 26 Overview of the Seabed surface. The surface is subdivided into section a) and section b) and will be further described. Profile a-a`can be viewed in Figure 27.....	43
Figure 27 Seismic inline profile illustrate how the seabed horizon easily can be traced across the dataset.....	44
Figure 28 Small curved lineations on the seabed surface. Profile a - a` show a inline profile crossing 5 small curved lineations	45
Figure 29 Large curved lineations on the seabed surface.	46
Figure 30 Overview map of the URU surface, inline profile a - a` can be seen in Figure 31. Illumination from north west.....	48
Figure 31 Inline profile, showing how the URU horizon changes along the dataset.....	49
Figure 32 Curved ridges located in the northern parts of the URU surface.....	50

Figure 33 Inline profile c – c`, illustrating how syn-form folded Pre-Quaternary strata truncates the URU surface and forms bedrock ridges on the surface.	51
Figure 34 Elongated depression (stippled line) located in the northern parts of the dataset. Variance timeslice from 740 ms (dotted line in profile). Variance maps highlight lateral change in amplitude. Faults appear with high values on a variance map and reveal the Bjørnøyrenna Fault Complex (BFC).....	52
Figure 35 Profile of elongated depression. Section a) crossline cutting the elongated depression from west to east. Section b) Variance time slice from 740 ms showing the Bjørnøyrenna Fault Complex (BFC).Section c), overview maps of the seismic profile in relation to a structure map of the Barents sea provided by NPD.no/factmaps. LH, Loppa High, BFC, Bjørnøyrenna fault complex and BB, Bjørnøya Basin.	54
Figure 36 Streamline lineations along the elongated depression.	55
Figure 37 Circular basin on the URU surface. Dotted lines represent 20 ms above and below the URU surface where RMS amplitudes were extracted from.	56
Figure 38 Hill hole pair cartoon, for comparison with the circular basin on URU. Figure from (Evans & Wilson, 2006).....	57
Figure 39 Circular depressions on the URU surface. RMS amplitude anomalies extracted 20 ms above and below the URU surface are added to the map (yellow-red areas).....	58
Figure 40 circular depression 3	60
Figure 41 Circular depression 5	62
Figure 42 Bright spots associated with the curved ridges on URU	65
Figure 43 Overview of bright spots along the elongated depression on URU. The dotted line marks the outline of the elongated depression	67
Figure 44 Bright spot at the base of the elongated depression. BB Bjørnøya Basin, BFC Bjørnøyrenna fault complex, LH Loppa High	68
Figure 45 Intra Quaternary horizon surface. Area a) contain curved lineations, b) streamlined lineations and c) line of depressions	70
Figure 46 Curved lineations on the intra Quaternary horizon and the seabed. Large lineation set 1 and 2 can be seen on both surfaces	71
Figure 47 Profile a – a` across curved lineations on the Intra Quaternary surface show how the scour marks on the seabed horizon penetrate the seafloor sediments to such a depth that they also scour the intra Quaternary horizon	72
Figure 48 streamlined lineations on the intra-Quaternary horizon	73

Figure 49 Line of depression on the intra Quaternary surface. Three profiles a-a`, b-b` and c-c` are shown next to and along the line of depression to indicate the characteristics of the intra Quaternary horizon at the different areas. A variance time slice from 700 ms reveals faults in the area. The faults can also be seen in the seismic profiles.	75
Figure 50 bright spots on intra horizon in the northern parts of the dataset. Arrows points to where the seabed reflector interferes with the intra horizon. Red areas are RMS amplitude anomalies.....	77
Figure 51 bright spots southern parts of the intra Quaternary horizon. The bright spots on the surface are connected by arrows with the seismic profile.....	78
Figure 52 Conceptual model of bedrock ridges and how they form in the top panels Figure from (Bellwald et al., 2019). The lower two panels show a planar view comparison of the ridges observed by Bellwald et al., (2019) (lower left) and bedrock ridges from our study (lower right).....	80
Figure 53 Collapsing of gas hydrates could result in the formation of curved ridges as observed on the URU surface. a) glacial stage were gas hydrates where stable. b) Post glacial period where the gas hydrates collapsed and formed ridge-depression, rhombohedral ridges on URU. c) Observed rhombohedral ridges on URU by Bellwald et al, 2019. d) Observed curved ridges on URU in our study area. Figure modified from Bellwald et al., (2019)	81
Figure 54 Conceptual model illustrating difference in ice flow velocity over 1) bedrock ridges vs 2) the elongated depression	84
Figure 55 Conceptual model of ice flow velocities on the URU surface.....	85
Figure 56 Blow-out craters observed on the seabed of Bjørnøyrenna (Andreassen et al., 2017) compared to the line of depressions on the intra Quaternary horizon within the study area. See Figure 49 for seismic profiles along the line of depressions.....	88
Figure 57 MSGL and line of depressions on the intra Quaternary horizon compared to MSGL and zone of depressions mapped by (Andreassen & Winsborrow, 2009). Lineation set 2 has the same orientation as the mapped MSGL on the intra Quaternary horizon.....	90
Figure 58 Conceptual model of ice flow and thermal regimes on the intra Quaternary horizon	92
Figure 59 comparing MSGL flowsets interpreted by Piasecka et al. (2016) (a) and ice flow direction of the mapped landforms on URU in our study area (b). Figure modified from Piasecka et al.,(2016)	95
Figure 60 Ice flow direction from the mapped landforms on URU and the Intra Quaternary horizon surface compared to (Winsborrow et al., 2010), (Andreassen & Winsborrow, 2009)	

and (Piasecka et al., 2016). Ice flow direction of the URU is linked to flow set 2 mapped on URU (Piasecka et al., 2016). Ice flow direction on the Intra Quaternary horizon is linked to flow set 13 from (Winsborrow et al., 2010) and flow set 2 from (Andreassen & Winsborrow, 2009). Flow set 2 and zone of depression by Andreassen & Winsborrow, (2009) is viewed in Figure 57. 97

Acknowledgement

Da er to lærerike år på masterstudiet plutselig over. Det føles godt å fullføre mastergraden men, tiden i Tromsø vil aldri bli glemt.

Først og fremst vil jeg takke min svært dyktige veileder, Monica Winsborrow. Tusen takk for svært god veiledning og din tilgjengelighet gjennom hele prosessen. Videre vil jeg takke min veileder Stefan Bünz, for god hjelp med tekniske utfordringer underveis.

Tusen takk til min gode venn Erik Steinsland for en god innsats med korrekturlesning, takk til mine medstudenter for faglige diskusjoner og fine øyeblikk. Jeg vil også rette en stor takk til min fantastiske kjæreste Regine Hagen for korrekturlesning, støtte og oppmuntring gjennom hele prosessen.

Jeg vil også takke Bjarte Selsaas for et godt samhold i tiden med hjemmekontor.

1 Introduction

1.1 Objectives

The aim of this thesis is to investigate interactions between glacial dynamics and fluid flow processes in the Loppa High Area, south western Barents Sea, using 3D seismic data. By studying the Quaternary sediment package this thesis will map the distribution of glacial landforms and sediments, identify indicators of fluid flow and look into any relations between glacial dynamics, fluid flow and formation of gas hydrates during the late Weichselian glaciation and deglaciation. This will be achieved through the following objectives:

- To reconstruct the dynamics of the Bjørnøyrenna Ice Stream in the Loppa High area
- To map the distribution of fluid flow and shallow gas indicators in the Loppa High area
- To investigate the interaction between shallow gas, fluid flow and deeper hydrocarbon reservoirs
- To investigate the potential for gas hydrate formation in the Loppa High region under glacial, deglacial and present day conditions
- To investigate the interaction between ice stream dynamics, fluid flow and gas hydrates

1.2 Study Area

In this thesis, a 3060 km² 3D seismic cube (DH14001) from the SW Barents Sea between Bjørnøya Island and mainland Norway (21°19'34,151"E 72°44'36,721"N) is investigated to get a broader understanding of glacial dynamics in the SW Barents Sea (Figure 1). The Barents Sea is located within the Arctic Circle and covers the shelf area between northern Norway and Svalbard in the west, and the Kola Peninsula, Nova Zemlya and Franz Joseph land in the east. The shelf expands over an area of 1,4 million km² and is one of the widest continental shelves on the planet (Vorren et al., 2011). The bathymetry of the Barents Sea reveals several shallow banks and over deepened troughs. Water depth on the banks alters from 0 – 200 meters while the troughs are as deep as 600 meters. The largest trough is Bjørnøyrenna located in the SW Barents Sea, it is about 150 km wide, 600 km long and water depths ranges from 200 m to 600 m (Figure 1). The Barents Sea has been glaciated multiple times over the Quaternary, most recently during the Late Weichselian, when Bjørnøyrenna hosted one of the largest ice streams to drain the Barents Sea Ice Sheet (Winsborrow et al., 2010). Bjørnøya is therefore an important feature regarding glacial dynamics in the SW Barents Sea. The primary controls of these bathymetric features are linked to large-scale tectonic events from the Late Cenozoic uplift and Quaternary glaciations and will be discussed in the following paragraphs.

Within the 3D cube, water depths alters from 500 meters towards center of Loppa High to 615 meters in the North West of the cube (Figure 1).

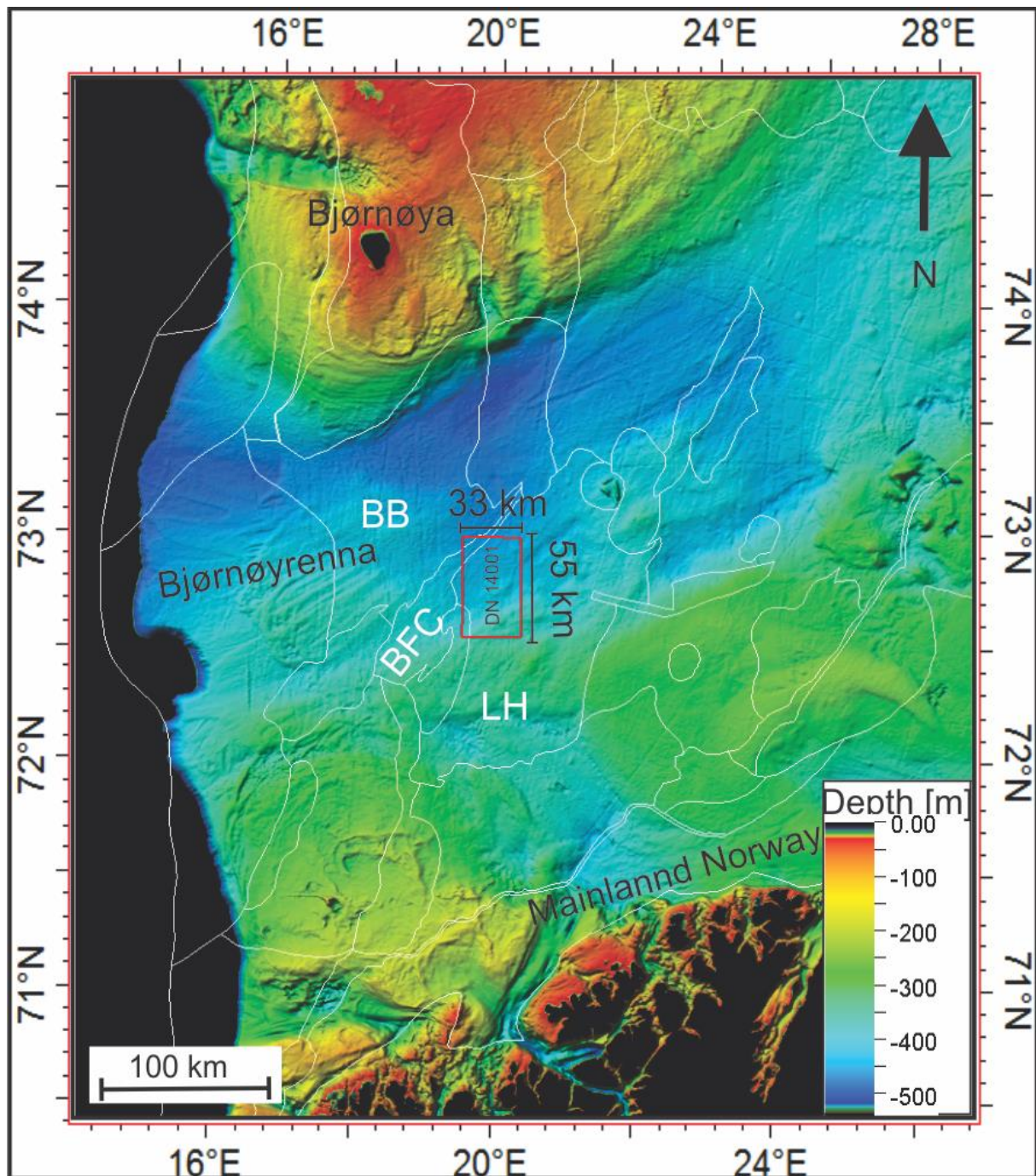


Figure 1 Bathymetric map of the SW Barents Sea. 3D seismic dataset DH 14001 is marked as a red rectangle. White lines represent geological structures of the Barents Sea, where Loppa High (LH), Bjørnøyrenna Fault Complex (BFC) and Bjørnøya Basin (BB) is marked in white. Bathymetric map from IBCAO version 3.0. Structural map from NPD-FactMaps.

Structurally the 3D cube is located on the Loppa High and bordering Bjørnøya basin in the NW (Figure 1). This structural high is originated from a series of rift basins terminated by

faults formed during Carboniferous (Ramberg et al., 2007). In Cenozoic the Loppa High experienced a series of uplift and erosional events, which resulted in sand and carbonate sedimentation on the rim of the Loppa High (Ramberg et al., 2007). These sands and carbonates have proved to be good hydrocarbon reservoirs. For example, the Gotha discovery by Lundin, proved oil and gas deposits in Permian karstified carbonates at 2281 meters (NPD, 2018). These deposits are not the main objective of this thesis, but they are an indication of hydrocarbon systems in the area and is an important factor regarding fluid flow and shallow gas deposits. Fluid flow and shallow gas deposits may also have affected glacial dynamics in the area and is an important aspect in this thesis.

From a glacial dynamics perspective, the Bjørnøya (Figure 1) is an important feature of the Barents Sea. Over multiple glaciations Bjørnøya hosted ice streams, which drained large volumes of ice, meltwater and sediment from much of the Barents Sea Ice Sheet (BSIS) (Andreassen & Winsborrow, 2009). By applying 3D seismic data, the Quaternary package will be investigated to gain knowledge about subglacial environment and factors that controlled glacial dynamics in this area.

The glacial sediments are the focus of this thesis, where internal structures and horizons within the glacial package will be further discussed and interpreted. The thickness of the glacial sediment package on the Barents Sea shelf varies from 0 milliseconds (ms) to 300 ms two way travel time (TWT) (Vorren et al., 1990) and is separated from the underlying preglacial bedrock by the Upper Regional Unconformity (URU) (Vorren et al., 1989). Within the 3D cube the URU horizon appears as a strong continuous reflector in the northern parts, and is less strong and less continuous in the southern parts.

1.3 Tectonic evolution of the SW Barents Sea

The tectonic evolution of the SW Barents Sea needs to be mentioned to better be able to discuss glacial dynamics and relation to fluid flow and gas hydrates within Bjørnøya. This chapter briefly describe the tectonic evolution of the SW Barents Sea through the Paleozoic, Mesozoic and Cenozoic.

1.3.1 Paleozoic

The Barents Sea basement dates back to the last period of the Caledonian mountain orogeny. At this time the Barents Sea was merged with northern Greenland and the Arctic parts of

Canada in the West, and Novaya Zemlya in the east (Ramberg et al., 2007). At the beginning of Carboniferous the Barents Sea area was located just north of equator and comprised the northern parts of Laurasia continent (Ramberg et al., 2007). During the Carboniferous and Permian, Svalbard and the Barents Sea drifted through several climatic zones before ending up in its present location (Ramberg et al., 2007). In the late Paleozoic most of the Barents Sea was affected by crustal extensional where the general rifting was migrating westward (Faleide et al., 1993). In the SW Barents Sea this caused the formation of rifts and pull apart basins. Later in the Mesozoic, tectonic activity followed these rift structures and they played an important role in forming the structure of the present SW Barents Sea.

1.3.2 Mesozoic

The SW Barents Sea in the early Mesozoic was tectonically relatively stable until the Mid-Jurassic. In Mid-Jurassic, the tectonic activity can be divided in two stages: Late Mesozoic rifting and basin formation, and Early Tertiary rifting and opening of the Norwegian Greenland Sea. These two stages are also known as Mid Kimmerian tectonic phase and the Late Kimmerian tectonic phase. The Late Mesozoic rifting and basin formation followed pre-existing structural elements formed in the late Paleozoic times. This resulted in normal faulting and development of several rift basins, for example the Bjørnøya, Harstad and Tromsø Basin (Faleide et al., 1993). At the same time, eustatic sea level rise led to deep marine conditions (Faleide et al., 1993) and sedimentation of organic rich shales along the basin flanks and intrabasinal highs in the Oxfordian and the Kimmerian (Faleide et al., 1993). These Late Jurassic sediments are known to have produced hydrocarbons, and play an important role regarding petroleum deposits and fluid flow processes in the SW Barents Sea. A relatively short time after deposition of carbon rich deposits in the Mid-Jurassic, rapid subsidence led to 5-6 km thick sedimentary infilling of the Bjørnøya, Tromsø and Harstad Basins in the early Cretaceous (Faleide et al., 1984). In Late Cretaceous to early Cenozoic the North Atlantic rift continued into the SW Barents Sea (Faleide et al., 1993). The North Atlantic rifting led to more normal faulting and potentially generated several migration pathways for fluids.

Later on in the Mesozoic deep-seated normal faulting along weaknesses in the Caledonian basement formed the Ringvassøy-Loppa fault Complex and the Bjørnøyrenna Fault Complex (Faleide et al., 1984). During the Cenozoic, these two fault complexes are suggested to have

acted as weakness zones, more prone to glacial erosion. This could have been a controlling factor regarding ice sheet dynamics in this area and promoted the formation of Bjørnøyarena. In the Late Cretaceous, an inversion changed the extensional regime to a compressional regime in the Bjørnøya Fault Complex. This led to thrust faulting and caused uplift of the Loppa High which lasted into the Early Cenozoic (Gabrielsen et al., 1997). In the Cenozoic the large glaciations play a major role in forming the SW Barents Sea.

1.3.3 Cenozoic

Rifting in the North Atlantic during Late Cretaceous- early Cenozoic led to opening of the Norwegian – Greenland Sea. This tectonic event led to reactivation of regional faults in the Western Barents Sea, resulting in a westward tilting, subsidence of the Barents Sea Shelf and developing of several platforms and basins. In addition, a series of uplift and glacial erosion events affected the whole Barents Sea shelf area causing large scale sedimentation along the western margin (Figure 2) (Lasabuda et al., 2018). Reactivation of faults created new migration paths for fluids and uplift and erosion caused, older hydrocarbon traps to leak. In the late Cenozoic, large glaciations were the primary control on the geological development of the SW Barents Sea. These caused large scale erosion and will be further discussed in the following sections.

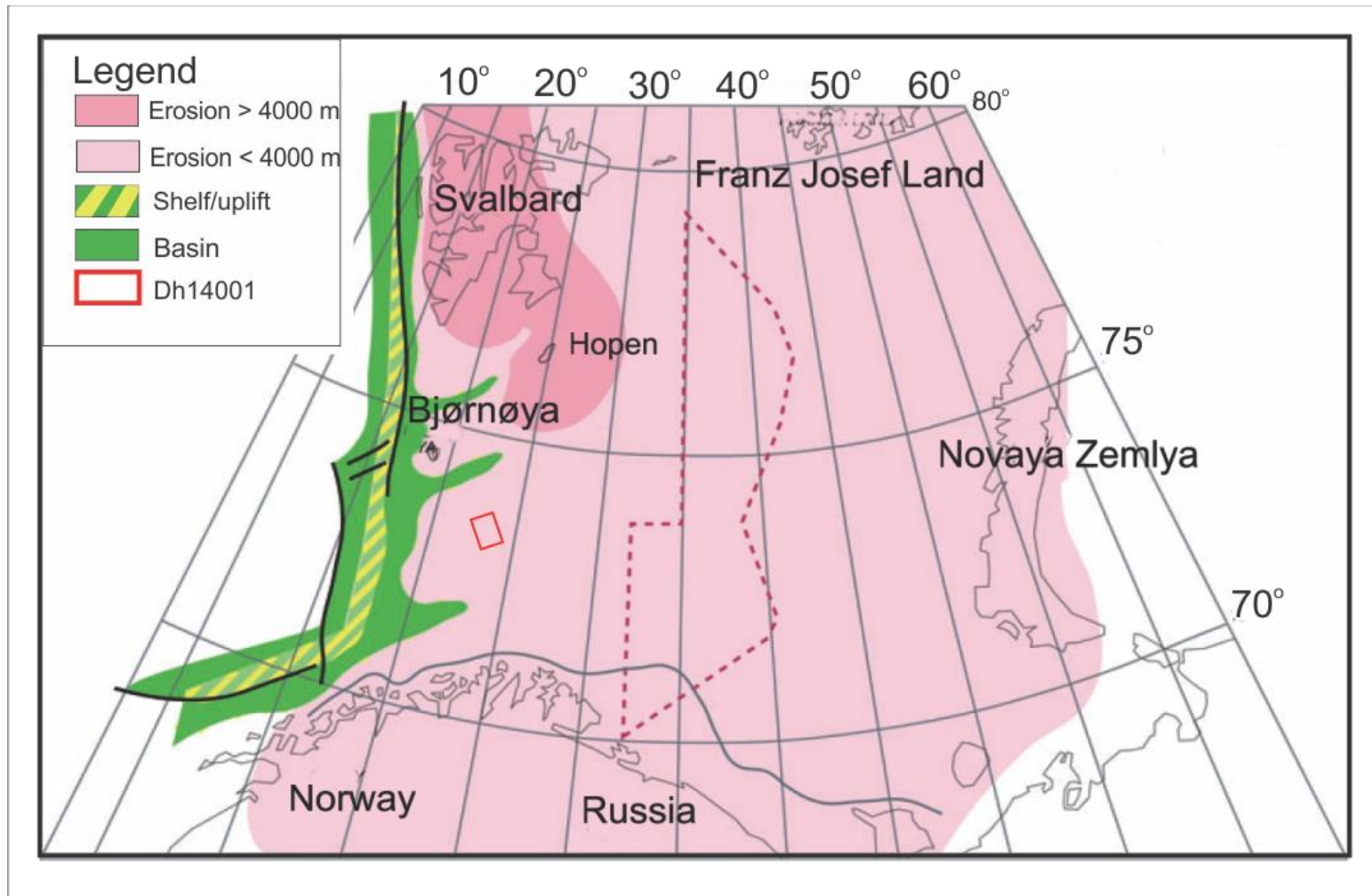


Figure 2 Paleogeographic map of the Barents Sea in late Cenozoic, illustrating erosion of the Barents Sea. Highest erosion during the late Cenozoic occurred in the area of Svalbard. Red square marks the study area. Figure modified from Worsley, (2008)

1.4 Glacial history of the Barents Sea and Bjørnøyareenna

1.4.1 The first Glaciations (Paleogene and Neogene)

As earlier mentioned (1.3 Tectonic evolution of the SW Barents Sea) the Barents Sea drifted from the Equator to the Arctic during the Carboniferous and Permian. Later on in Paleogene and Neogene, opening of the Norwegian Sea and the formation of the Alps, Pyrenees and the Himalayas took place. This respectively changed the ocean circulation pattern, and prevented exchange of tropical and Arctic air masses. These events provoked a colder period for the Barents Sea which started in the Paleogene (Ramberg et al., 2007). By studying ice rafted debris (IRD) (Stickley et al., 2009) suggested a climatic switch in the middle Eocene (46 Ma). The climate changed from warmer sea ice-free condition, to a colder climate with seasonal winter sea-ice (Stickley et al., 2009). However, it was not until the Pliocene that the first Barents Sea Ice Sheet (BSIS) formed. Several glaciations have been recorded since, but just how many is still discussed. Solheim (1996), suggest that sixteen glacial advances have reached the north western margin of the Barents Sea, and whilst along the western Barents Sea margin it is suggested that grounded ice reached the shelf edge at least eight times (eg. Andreassen et al. 2004, (Knies et al., 2009).

1.4.2 Pleistocene

The extension of the early Pleistocene glaciations in the Barents Sea is largely unknown, but numerical modelling from (Butt et al., 2002) suggests that the continental shelf was ice-free at this time. This is supported by glacial sediments from the same age on the western paleo-shelf break, indicating that there was rivers connecting the shelf break and the glaciers (Vorren et al., 2011). There are also evidence recorded of mountain glaciers on Spitsbergen between 2.6 and 1.6 Ma (Butt et al., 2000). In the later parts of the early Pleistocene, the first well-documented shelf-edge glaciation occurred (Andreassen et al., 2007). By investigating regional scale sea floor geomorphology and geomorphology from 3D seismic data it has been concludes that grounded ice extended to the SW Barents Sea shelf break several times during the last million years and probably as fast-flowing ice streams (Andreassen et al., 2007). In Bjørnøyareenna, several sets of Mega Scale Glacial Lineations (MSGL), formed by ice streams have been mapped on buried horizons within the pre-Late Weichselian sedimentary package (Andreassen & Winsborrow, 2009). As well as MSGL, large irregular depressions with the

same orientation as the MSGL have also been mapped and interpreted to be subglacial sediment blocks and rafts which has been removed and by fluctuating ice stream activity (Andreassen & Winsborrow, 2009).

1.4.3 Late Weichselian Glaciation

The Late Weichselian is the most recent glacial period, reaching its maximum at the Last Glacial Maximum (LGM) ~23 ka – 21 ka (Hughes et al., 2016). At that time, the Barents Sea Ice Sheet (BSIS) was coalescent with the British-Irish Ice Sheet (BIIS), and the Scandinavian Ice Sheet (SIS) which together formed the Eurasian Ice Sheet Complex (EISC) (Figure 3) (Patton et al., 2017). The EISC was at that time the third largest ice sheet complex on the planet, with a lateral span of 4500 km and responsible for 20 meters of eustatic sea-level lowering (Hughes et al., 2016). The maximum extent of the LGM (Figure 3) is mapped based on ice-contact landforms such as till deposits, stratigraphy and moraines (Hughes et al., 2016). However, the maximum extent of the Eurasian ice sheet occurred at different times in different sectors.



Figure 3 LGM, illustrating the British-Irish Ice Sheet (BIIS) Scandinavian Ice Sheet (SIS) and the Svalbard Barents Kara Ice sheet (SBKIS), in this thesis referred to as the Barents Sea Ice Sheet (BSIS). Figure from Hughes et al, (2016)

For the BSIS, the timing and the maximum extent has been discussed over the past decades. Based on landform mapping from several studies, Jakobsson et al., (2014) suggest the LGM extent in the Barents Sea follows the western shelf break from the mainland Norway in the south and all the way up to the northern most point of Svalbard (Jakobsson et al., 2014).

Eastwards it continue following the shelf break north of Franz Josef Land and the Kara Sea. The Eastern ice margin is set just east of Novaya Zemlya (Figure 3), however the eastern margin is less studied and the extent here remains uncertain.

Regarding the Southwestern Barents Sea, several cross shelf troughs such as Storfjordrenna, Kveithola and Bjørnøyareнна worked as major drainage routes for the BSIS during the Late Weichselian, where Bjørnøyrenna was the largest and is the focus of this thesis. During the Late Weichselian glaciation, Bjørnøyrenna hosted fast flowing ice which caused large-scale erosion where glacial sediments were deposited on the shelf, building out the Bjørnøyrenna trough mouth fan (TMF), a unique glacial archive (Landvik et al., 1998). Studies of the seismic stratigraphy of the Bjørnøyrenna TMF suggest that it consists of three main sediment packages GI, GII and the uppermost GIII (Figure 4) (Andreassen & Winsborrow, 2009). The lower most GI is interpreted to be shelf-margin glacialfluvial to glaciomarine sediments (Andreassen & Winsborrow, 2009), consistent with distal glacial input. The second is interpreted as large scale mass-movement deposits from slides and slumping, marking the onset of shelf edge glaciations, and the uppermost GIII is interpreted as glacial debris flow indicating shelf-edge ice streaming (Andreassen & Winsborrow, 2009).

Within Bjørnøyrenna, imprints of megascale glacial lineations (MSGSL) mapped on the paleo-seafloor indicate fast flowing ice from the Late Weichselian glaciation (Piasecka et al., 2016). The lineations that has been interpreted to represent the Late Weichselian glaciation are observed on the Seabed surface, intra Quaternary horizons and the Upper Regional Unconformity (URU). URU represent the base of the glacial sedimentary pack and has lies about 57 – 63 m below the present seafloor in central Bjørnøyrenna (Piasecka et al., 2016).

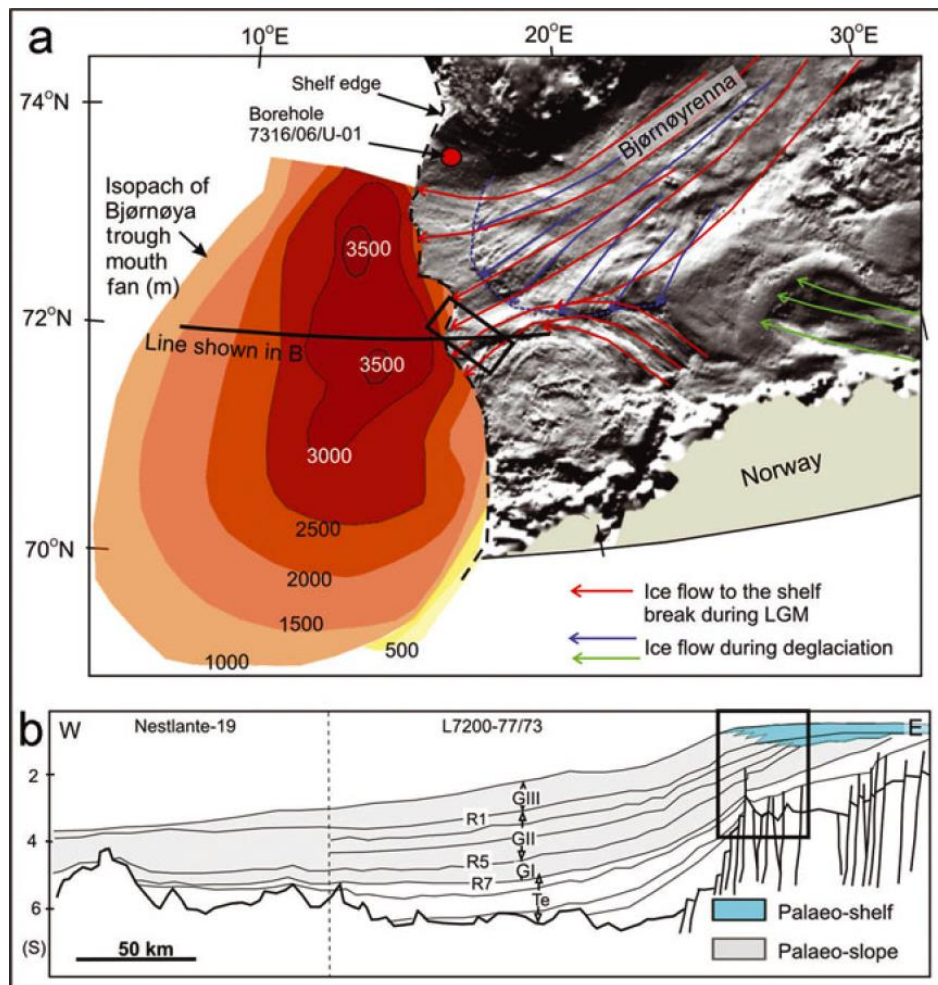


Figure 4 a) Ice flow direction based on their mapping of mega scale glacial lineations and a isopach map of the Bjørnøyrenna TMF. b) profile across the Bjørnøyrenna TMF showing the three glacial sediment units G1, GII and GIII. Figure from (Andreassen & Winsborrow, 2009)

1.4.4 Deglaciation of the Late Weichselian glaciation in the SW Barents Sea

The retreat of the Late Weichselian EISC glaciation is suggested to have started ~24 ka BP, however the deglaciation was highly asynchronous with rapid retreats, standstills and re-advances occurring at different places on the EISC at different times (Hughes et al., 2016). For the South Western Barents Sea the ice margin has been recorded to have reached the shelf break two times during the Late Weichselian glaciation, first time before 22 Ka BP and the second time around 19 Ka BP (Winsborrow et al., 2010). After 19 ka BP initial retreat over the Western Barents Sea and along the Atlantic margin occurred and is believed to have been triggered by global eustatic sea level rise. This caused a major increase in icebergs calving in the cross shelf troughs, including Bjørnøyrenna causing a considerable loss of ice volume. Most of the Barents Sea Ice Sheet is thought to have been ice free by ~15 Ka BP (Vorren &

Laberg, 1996). The deglaciation of the SW Barents Sea included periods of standstills and re-advances and has been divided into five stages (Winsborrow et al., 2010).

Stage 1, represent the second Late Weichselian maximum event where the whole Barents Sea continent was glaciated. Ice drainage of the Barents Sea Ice Sheet was dominated by the Bjørnøyrenna ice stream. MSGL related to this time period have been mapped in Bjørnøyrenna and reached all the way to the shelf break at ~19 Ka BP (Figure 5) (Winsborrow et al., 2010).

Stage 2, is related to the start of the deglaciation and began with significant retreat of the ice margin in the Southern Barents Sea. The ice margin at this point is marked by grounding zone wedges which have been observed in Håkjerringdjupet and Bjørnøyrenna and marks as a period of retreat followed by readvance of the ice streams ~17 ka BP (Figure 5) (Winsborrow et al., 2010).

Stage 3, A significant change in the dynamics of the Barents Sea Ice sheet occurred where the center of maximum ice volume shifted eastward. At this point the deepest areas of the Bjørnøyrenna ice stream were ice free, but still active. A grounding zone wedge located 250 km from the shelf edge marks the ice margin at this stage ~16 Ka BP (Figure 5) (Winsborrow et al., 2010).

Stage 4 and 5, where the Southern Barents Sea ice disappeared and the ice margin was now located in the outer fjord areas in Northern Norway (Figure 5) (Winsborrow et al., 2010)

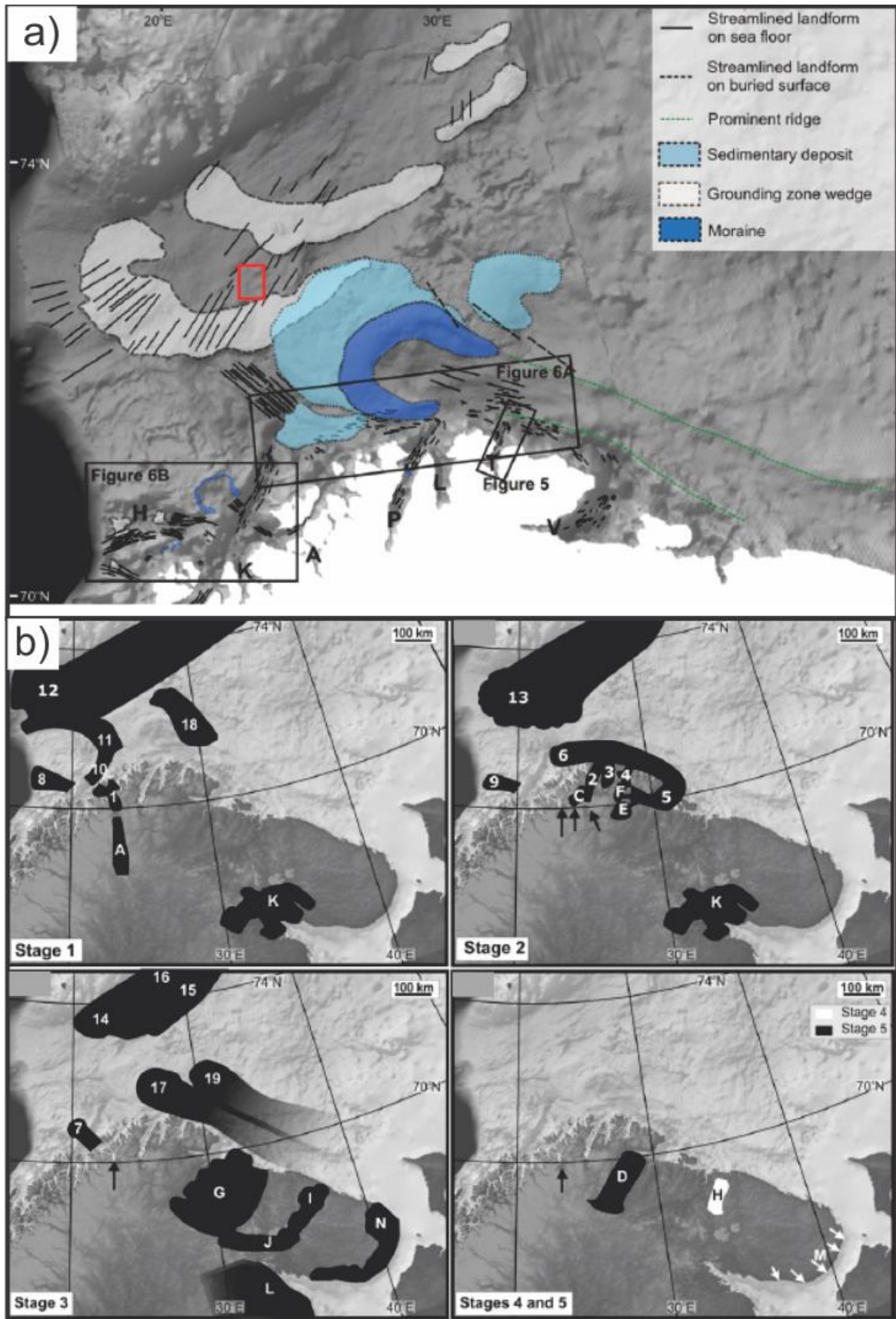


Figure 5 Deglaciation of the southern Barents Sea divided into five stages. Dataset DN 14001 is marked in red. Figure modified from Winsborrow et al., (2010)

However, a recent study on the collapse of the Eurasian ice sheet, suggests that the marine-based sector of Eurasian ice sheet collapsed over only 500 years. For Bjørnøyrenna they suggest that main parts where deglaciated from 14.71 to 14.57 Ka BP (Brendryen et al., 2020).

1.5 Glacier dynamics and landforms in the SW Barents Sea

1.5.1 Ice Streams

Ice streams are defined as regions of a grounded ice sheet with much higher flow velocities (often > 300 m/year) than the surrounding ice (Stokes & Clark, 1999). Most ice sheets will have one or several ice streams working as drainage areas for the ice sheet and the ice streams can either be constrained by topography or by slower moving ice (Bennett, 2003). An ice stream will start forming in areas with the least basal resistance. These areas can be weakness zones such as fault complexes, topographical lows or a combination. Topographical lows are favorable for fast flowing ice for several reasons. As the ice thickness increases in topographical lows, the driving stress at the bed increases which again enhancing the internal deformation as defined by Glens Flow Law (Paterson, 2016). Thicker ice also means better insulation and increased basal temperature. This may lead to basal melting and lubrication, which enhance bed slip. Meltwater will also drain towards topographic lows and give a positive feedback on flow velocity (Bennett, 2003). Bjørnøya is an example of an paleo ice stream, which was working as a drainage outlet of the Barents Sea Ice Sheet during the LGM and the deglaciation (Andreassen & Winsborrow, 2009).

In palaeo-ice sheets, the location of ice streams can be inferred based on the nature and type of glacial landforms and sediments. A key landform diagnostic of ice streaming is megascale glacial lineations, which have been identified widely on palaeo and contemporary ice stream beds (e.g. (Stokes & Clark, 1999), (King et al., 2009)). Megascale glacial lineations have been mapped on the seabed and buried surfaces of Bjørnøyrenna. These have been described to have reliefs up to 10 m, width ranging from 50 – 360 m and lengths up to tens of km long (Andreassen & Winsborrow, 2009). The Bjørnøyrenna has hosted several generations of ice streams and therefore there are multiple sets of MSGL with different orientations within the Quaternary succession (Figure 4) (Andreassen & Winsborrow, 2009). An intra horizon (GII)

(Figure 4) can be imaged and contain three sets of MSGL. These represent ice flowing towards the shelf during LGM (red arrows Figure 4) and northwest and southwest flowing ice during the deglaciation (Green and blue arrows). These landforms are characteristic for fast flowing ice and often reflects “warm-base ice” (Stokes, 2018). Cold base ice can be associated with the opposite, slower moving ice within an ice stream, such areas are called “sticky spots”.

1.5.2 Sticky spots

As mentioned, ice streams are fast flowing ice, which drain large-scale ice sheets. However ice streams are complex and the resistance of the bed are rarely uniform (Stokes, 2018). Within an ice stream, high friction areas are referred to as “sticky spots” and work as an anchor for the ice stream (Stokes, 2018), playing a fundamental role in determining their velocity and stability. The origin of such sticky spots have been discussed, and there are several plausible explanations.

Large bedrock bumps or ridges, taller than the till thickness can penetrate into the base of the ice stream and thereby work as a sticky spot (MacAyeal et al., 1995). As an example, MacAyeal (1995) suggested that a 1m tall hemispherical bump which constitute 1 % of the basal bed where the iceflow velocity is 450 m/yr will be able to support 10 kPa of shear stress (MacAyeal et al., 1995). Discontinuity of the basal till layer could have the same effect, but is suggested to support a lot less stress than a bedrock ridge bump (Stokes, 2018). Micro earthquakes and regions with stiffer beds are more likely to support basal sliding compared to areas with thick till deposits (Stokes, 2018) . These areas are suggested to be small clusters of micro earthquakes in stiff/low porosity sediments (Stokes, 2018). As well as basal friction, ice thickness anomalies can force surface water in around the underlying area away and cause till stiffening (Stokes, 2018). The saturation of fluids and especially gas hydrates within the till deposits has in later years been suggested to have a till stiffening effect (Winsborrow et al., 2016).

Gas hydrates can have a stiffening effect on subglacial sediments, and in that way increase basal friction. This has been observed by looking at gas hydrate hosting sediments from the Mackenzie Delta, Northern Canada which show that the shear strength increases by an eightfold compared to non-gas hydrate hosting sediments (Winters et al., 2004). In Håkjerringdjupet ice stream, results show that local patches of stiff gas hydrate hosting

sediment above shallow bedrock have been increasing basal friction and enhancing the resistance of the overlying ice flow (Figure 6) (Winsborrow et al., 2016). High shear-strength sediments result in glacitectonic thrusting, source depressions and subsequent depositing of hydrate bearing sediments as hill-hole pairs visible on the modern sea floor (Figure 6) (Winsborrow et al., 2016). Gas hydrates and fluid flow are therefore an important part of understanding glacial dynamics in the SW Barents Sea. This topic will be further explained in upcoming sections.

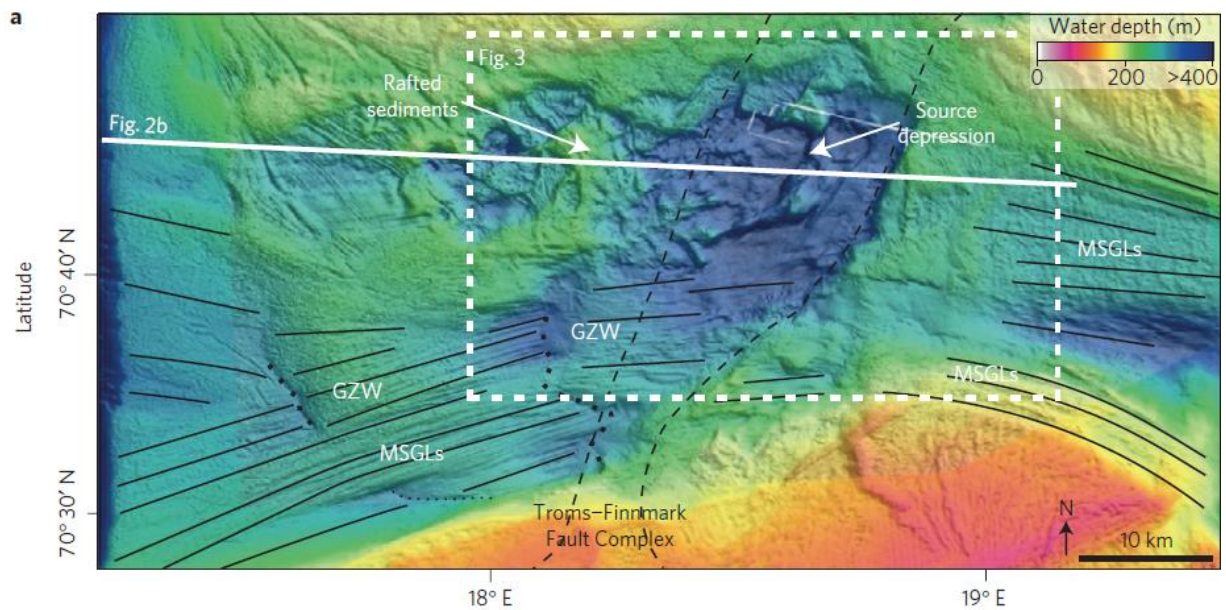


Figure 6 Bathymetric map from Håkjerringdjupet, showing landforms indicating fast flowing ice (MSGs) and glacitectonic landforms indicating slower flowing ice (Source depressions and rafted sediments). Figure from (Winsborrow et al., 2016)

1.5.3 Grounding zone wedges (GZW)

Grounding zone wedges are sedimentary ridges deposited during ice sheet retreats across polar continental shelves and are often related to periodic retreat, halt or re-advance events (Dowdeswell & Fugelli, 2012). These landforms can vary in size and shape, however typically grounding zone wedges are approximately 5 – 20 km long, 50 – 100 meter thick and have a lateral width of several tens of kilometers (Dowdeswell & Fugelli, 2012). These dimensions are dependent on sediment flux, duration of the halts, sub-ice cavity shape and the width of the ice stream (Dowdeswell & Fugelli, 2012). In a seismic section, they appear as asymmetric, with a steep ice distal side and often chaotic internal structure (Figure 7), probably as a result of deposition of diamictic debris (Dowdeswell & Fugelli, 2012). Viewed perpendicular to the flow direction, the grounding zone wedge is more symmetric with some

internal structures (Figure 7). Reflectors often truncate the base of grounding zone wedges, indicating erosion during formation of these landforms.

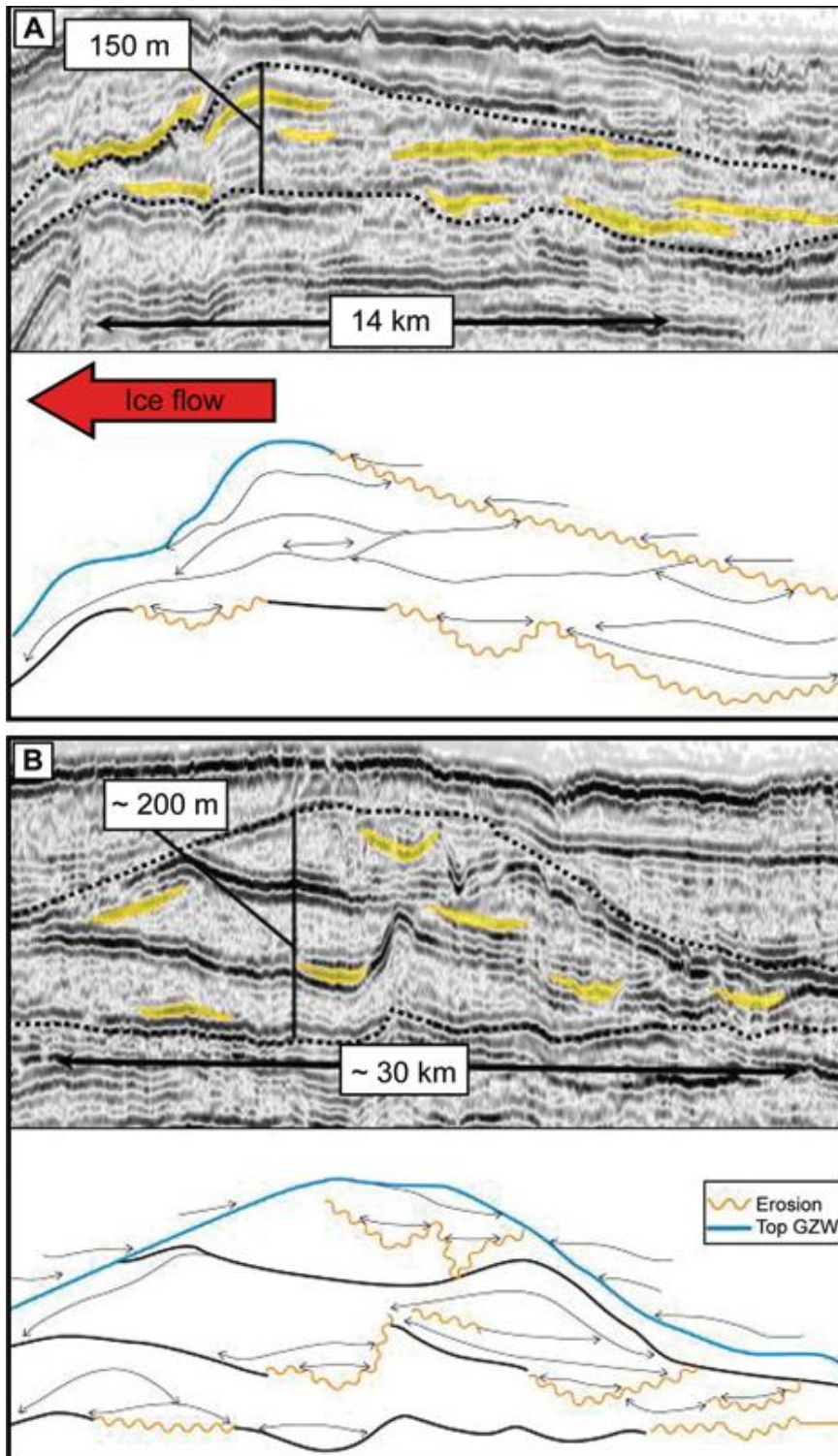


Figure 7 Seismic profile of a grounding zone wedge parallel and perpendicular to the ice flow direction. Figure from Dowdeswell & Fugelli, (2012)

Along the Norwegian coast and the western Barents Sea, grounding zone wedges are found on the beds of several palaeo-ice streams, marking positions of ice stream stillstands and readvances during deglaciation. In Bjørnøyrenna, a well-developed series of grounding zone wedges provide evidence for multiple periods of ice margin stillstands or readvances during the deglaciation (Figure 5). Some of these grounding zone wedges have MSGs on their upper surface, indicating ice streaming continued during their deposition (Winsborrow et al., 2010).

1.5.4 Iceberg ploughmarks

The Barents Sea shelf is relatively shallow (hundreds of meters) and was even shallower during LGM due to large water masses stored on land as ice resulting in lower sea level. Icebergs from marine based ice streams, if large enough, once calved from the ice margin, may plough the soft seabed sediments creating iceberg ploughmarks as they drift driven by ocean currents and wind. Such ploughmarks are a characteristic feature of glaciated continental.

Single-keeled ice berg ploughmarks have been described as large curvilinear and small curvilinear grooves and has been observed on the sea floor of the Barents Sea (Figure 8) (Shackleton et al., 2020) . Smaller ploughmarks appear in all directions and regularly cross-cuts each other (Figure 8). They are described to be typically <1 m wide and <2 meter deep. Large curvilinear groovers are described to be 2 m deep and with lengths up to 7,6 km. Cross cutting is also common for larger single keeled ploughmarks (Figure 8).

Multi-keeled icebergs ploughmarks are also found on the seabed in Storfjordrenna (Figure 8). These have a wide range of widths from 300 m to 4,6 km (Shackleton et al., 2020). How many grooves per set is variable and does not necessary correlates with the width of the ploughmark. The width and number of grooves usually diminishes with an increase in waterdepth (Shackleton et al., 2020). They are believed to be from large tabular iceberg calvings off an ice-stream terminus associated with a grounding zone (Shackleton et al., 2020). These large scour marks are also seen on buried surfaces as they penetrate the Quaternary sediments from the seabed and down a paleo seabed surface.

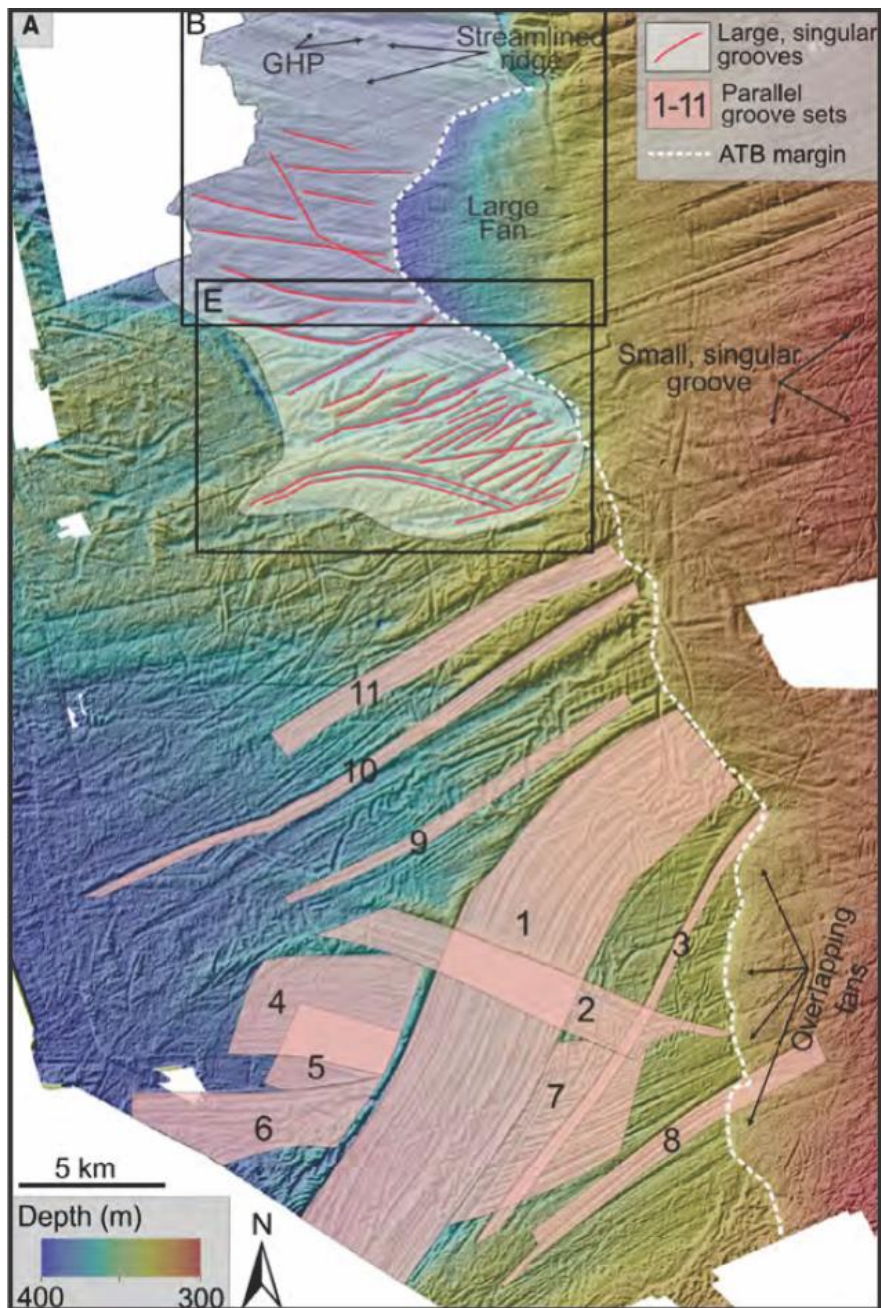


Figure 8 Large singular grooves and parallel groove sets from Storfjordrenna interpreted as ice berg scour marks. Figure from (Shackleton et al., 2020)

1.5.5 Glacitectonics

Glacitectonism is defined as the large scale displacement of sub and pro glacial material, where both ductile and brittle deformation of sediment and/or bedrock may occur (Benn & Evans, 2014). These landforms are related to compressional dominated flow within glaciers and ice streams, and have therefore been associated with cold-based and/or high frictional resistance subglacial conditions.

Sedimentary coring from the outer Bjørnøyrenna found evidence for glacitectonically displaced Cretaceous bedrock (Figure 9), with a borehole penetrating a unit of Cretaceous rocks in-between two units of glacial till. This represent a rare example of direct evidence for a glacitectonic raft/megablock (Sættem et al., 1992).

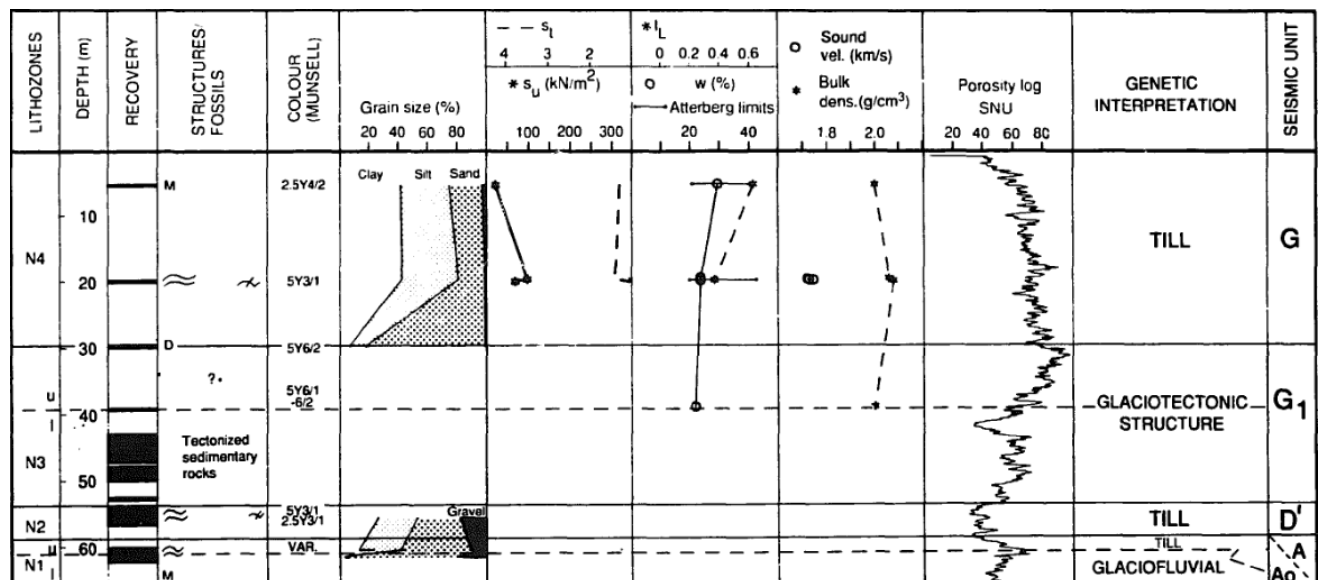


Figure 9 Table of lithological borehole properties. Unit G1 show glacitectonic structures of Cretaceous sedimentary rock in between two units of till. Figure from (Sættem et al., 1992).

In the SW Barents Sea, a series of studies has mapped evidence of glacitectonic landforms (e.g. (Sættem et al., 1992), (Winsborrow et al., 2016)) where the most characteristic are:

- Hill hole pairs
- Composite ridges and thrust block moraines
- Cupola hills
- Mega blocks and rafts

Hill-hole pairs form by ice thrusting, where ice eroded material is picked up and moved a short distance in ice-distal direction. The deposits typically form a discrete ice-thrust hill, and consist of Quaternary sediments or consolidated pre-Quaternary sedimentary rocks (Figure 10) (Sættem, 1990). A short distance ice-proximal from the ice-thrust hill, a basin forms (Figure 10). Such basin can be water filled lakes in terrestrial settings and often have the same size and shape as the ice-thrust hill (Evans & Wilson, 2006). In terms of size and volume, hill hole pairs typically ranges from 1 km² to 100 km² and 30 m to 200 m in structural relief (Sættem, 1990). Hill-hole pairs commonly follows a boundary between consolidated and soft unconsolidated sediments, and may also follow the boundary between frozen and non-frozen sediments (Winsborrow et al., 2016). The process responsible for these landforms has been discussed in earlier studies. Clayton and Moran, (1974) suggest that hill-hole pairs form subglacially near the glacier terminus where the glacier bed is frozen. As the glacier starts to move, subglacial material is ripped off and deposited downstream (Sættem, 1990). A study on regulation of ice stream flow from Håkjerringdjupet by (Winsborrow et al., 2016), suggest that hill-hole pairs on ice stream beds may represent the geological imprints of sticky spots and that sub glacial gas hydrates formation may promote the glacitectonic deformation.

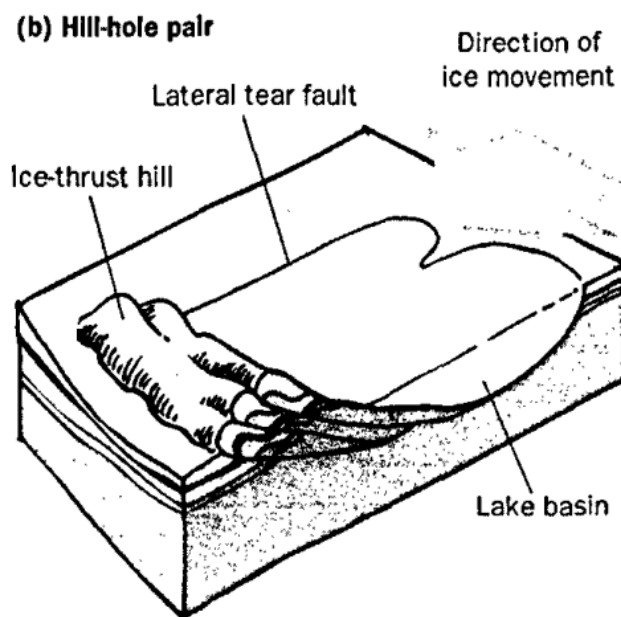


Figure 10 Hill-hole pair cartoon. Figure from (Evans & Wilson, 2006)

Composite ridges (thrust block moraines) form by excavating and elevating of proglacial material (Figure 11). Such ridges are composed of several imbricated slices of up-thrust

bedrock and/or unconsolidated sediments, usually interlayered and overlaid by glacialfluvial sediments (Benn & Evans, 2014).

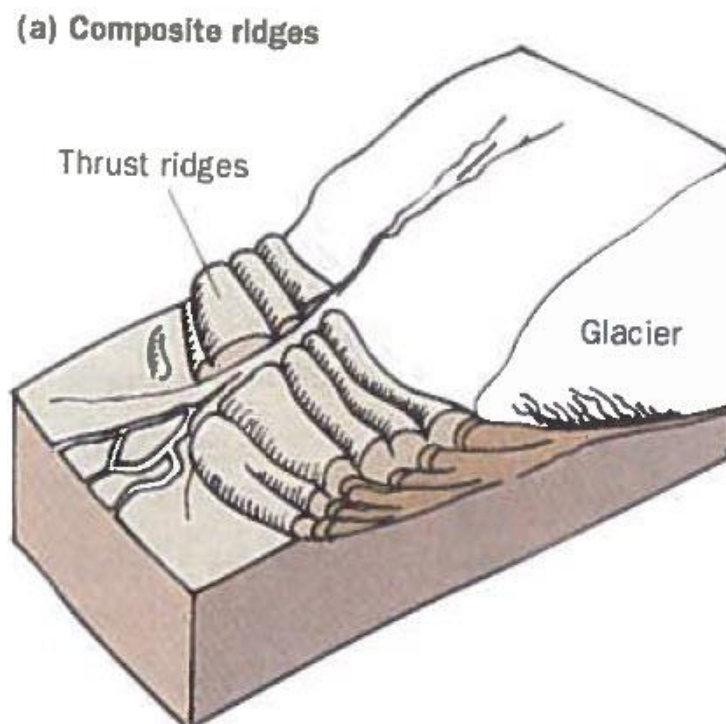


Figure 11 Composite ridges cartoon. Figure from (Benn & Evans, 2014)

Cupola hills are irregular hills with glacitectonic characteristic (Figure 12). In general, these features are smoothed and or overridden versions of hill-hole pairs or composite ridges (Evans & Wilson, 2006). Typically they have dome-like morphology, areal span of 1-15 km and 20-200 meter height. The internal structure are ice thrust, detached and deformed flows of Quaternary or older strata which truncates underlying structures (Benn & Evans, 2014). These structures are overprinted by a carapace of till and often covered by flutes oriented in ice flow direction. On the intra horizon GI in Bjørnøyrenna, cupola hills are observed buried within a sequence of till (Sættem et al., 1992). Cupola hills are interpreted to be connected to grounded ice forming the ice thrust hills, which thereafter are overprinted and buried by sedimentation from moving ice (Sættem et al., 1992).

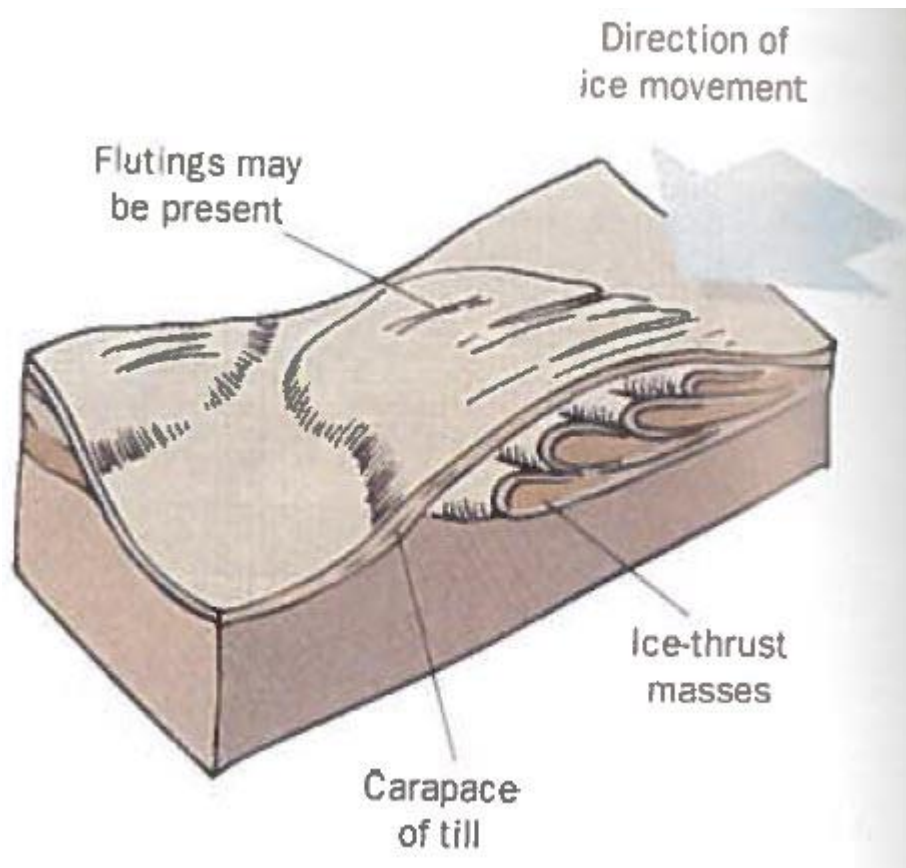


Figure 12 Cupola hills cartoon. Figure from (Benn & Evans, 2014)

Megablocks and rafts are large blocks or slabs of unconsolidated strata transported from their original position by glacial action (Benn & Evans, 2014). The mechanism for this type of glaciers erosion has been discussed. Freeze-on to the base of a cold base ice sheet is one of the theories, but failure within the strata is also a plausible explanation. In a seismic section these features may be mistaken for bedrock outlines as they often appear as flat topped buttes or plateaus (Figure 13) (Benn & Evans, 2014). Megablocks has been observed aligned in long chains parallel to the ice flow direction in Bjørnøyrenna with sizes varying from hundreds of square meters, to several square kilometers in areal (Andreassen & Winsborrow, 2009). The megablocks and rafts are overprinted by MSGGL, which is interpreted to represent a change from slower moving ice to fast flowing ice. Till stiffening, due to subglacial freezing has been invoked to explain this change in sub-ice stream conditions (Andreassen & Winsborrow, 2009).

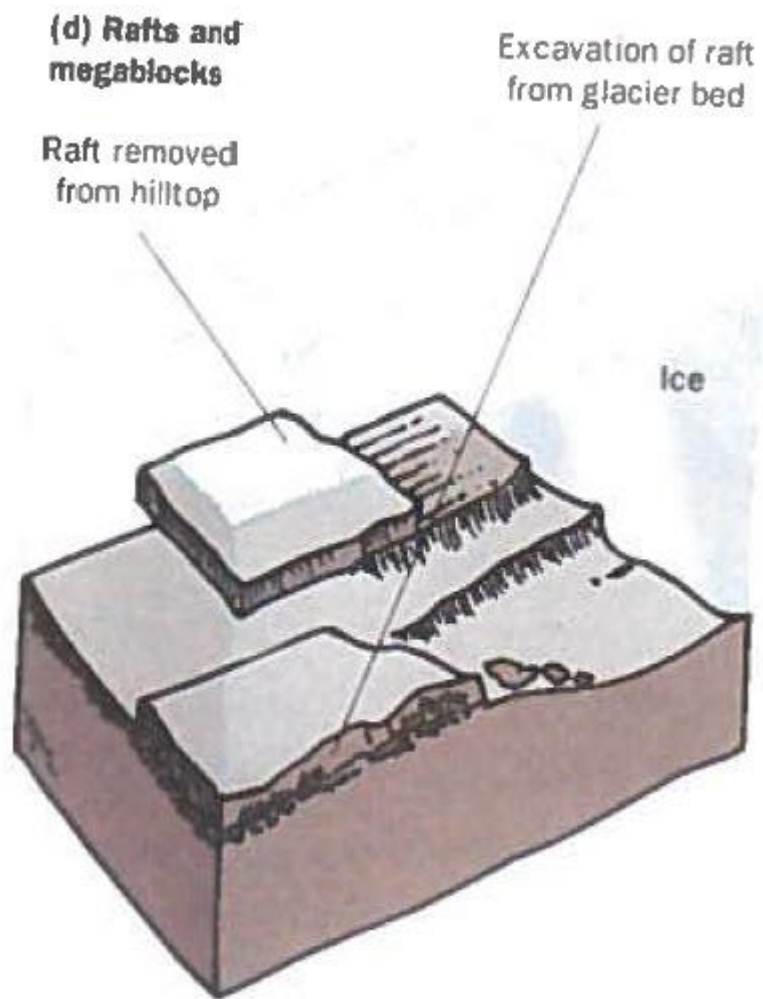


Figure 13 Rafts and megablocks cartoon. Figure from (Benn & Evans, 2014)

1.6 Gas hydrates and Fluid Flow

1.6.1 Gas hydrates

Gas hydrates are solid compounds of water and gas, in which the water molecules enclose molecules of natural gas (Kvenvolden, 1988). They form under specific pressure-temperature conditions, often found beneath the seabed along continental margins, but also on land in permafrost regions (Kvenvolden, 1988). Such conditions may also be expected beneath ice sheets. Propane, ethane and carbon dioxide may be found as hydrates, however methane is considered to be the most abundant hydrate (Kvenvolden & McMennamin, 1980). In the marine environment, the stability of hydrates is controlled by bottom water temperature, geothermal gradient, seabed pressure, composition of gas and pore water salinity. These parameters define areas where hydrates are stable, also called the gas hydrate stability zone (GHSZ) (Kvenvolden & McMennamin, 1980). The base of this zone often appear as a strong reversed reflector, in a seismic section it is referred to as the bottom-simulating reflector (BSRs) (Figure 14) (Vadakkepuliyaambatta et al., 2017). Below the BSR are accumulations of free gas, which can be leakage from deeper hydrocarbon reservoirs. In a seismic section free gas or shallow gas accumulations can appear as bright spots.

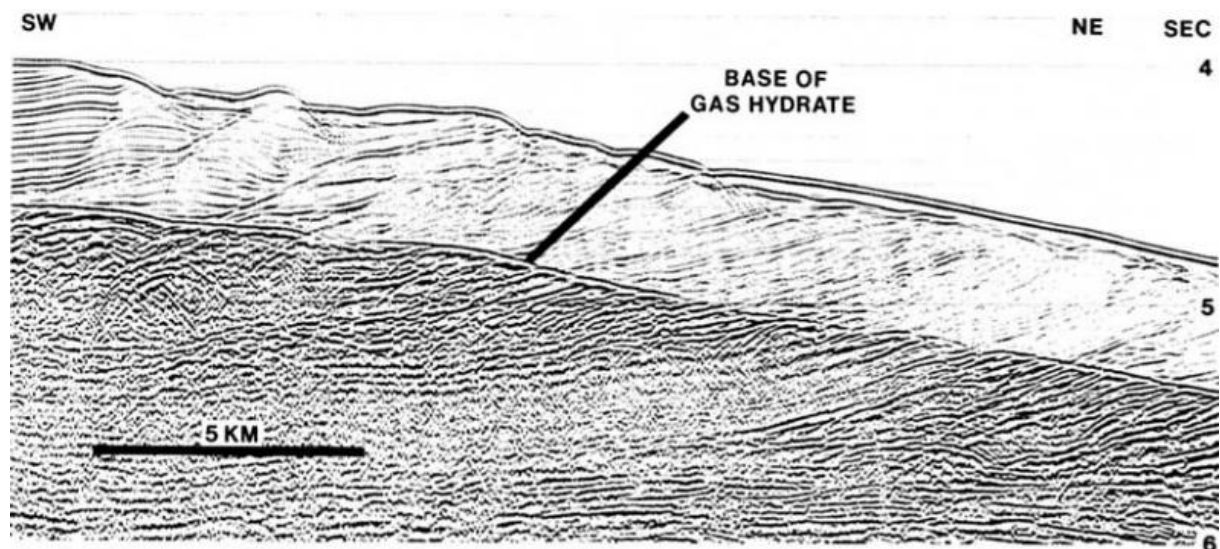


Figure 14 BSR reflector, figure modify from (Shipley, 1979)

During the LGM, higher pressures and lower temperatures cause a much deeper gas hydrate stability zone. In some areas of the SW Barents Sea it has been modeled to be 600 m thick (Chand et al., 2012). However, today the gas hydrate stability zone has thinned due to the melting of the Barents Sea Ice Sheet and gas hydrates are therefore only observed in local areas (Vadakkepuliambatta et al., 2017). The gas hydrate stability zone in the SW Barents Sea is also highly variable due to high-order hydrocarbons, salt tectonics and heat flow. Uplift and erosion from the Cenozoic has also caused hydrocarbon traps to leak potential free gas. Today the BSR is primarily observed nearby focused fluid flow features, such as faults and gas chimneys (Figure 15) (Vadakkepuliambatta et al., 2017). In the Bjørnøya Basin the stability condition has proven suitable for gas hydrates. However, gas compositions data from wellbores in the area indicate highly variable gas composition (Vadakkepuliambatta et al., 2017).

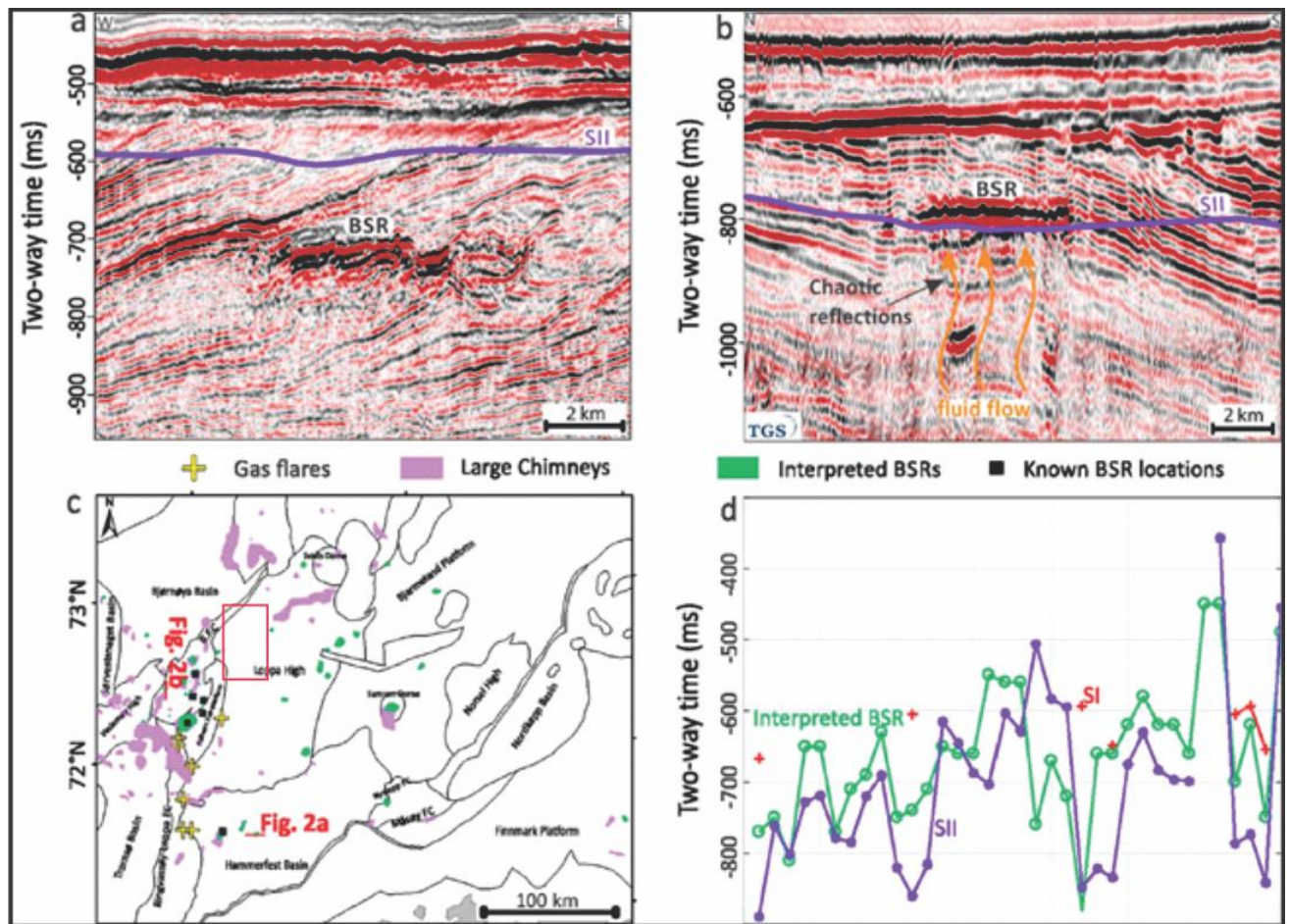


Figure 15 Interpreted BSR in the SW Barents Sea and how they appear in a seismic section. Red square marks dataset DH14001. Figure modified from Vadakkepuliambatta et al., (2017)

1.6.2 Fluid Flow

The term fluid flow includes all migration processes from the deeper geosphere to the water column. The fluids can occur as gas or liquid and are often hydrocarbons. Fluid flow is proposed to contribute with large quantities of methane and other greenhouse gasses into the water column and potentially the atmosphere, which possibly can contributing to a global scale climate change (Chand et al., 2012). As well as the climatic aspect, fluid flow processes and gas hydrate have also been suggested to affect glacial dynamics during the glaciations as

mentioned earlier. Fluid flow processes are often associated with sub-seafloor hydrocarbon reservoirs, trapped gas under gas hydrates or due to dissolving of gas hydrates (Chand et al., 2012).

In a seismic section there are several indicators to look for when searching for fluids and fluid flow. Anomalies in the seismic data are common for indicating fluids where the simplest type of fluid flow related anomalies are lateral variations. Such anomalies can be local increased or reduced amplitude strength, continuity, frequency or AVO (amplitude vs offset) (Løseth et al., 2009). Example of these anomalies can be seen in Figure 16 where bright spots represent amplitude anomalies and dim spot and phase reversal represent an anomaly in continuity. The abundance of gas will often cause a bright spot. This is due to the low acoustic velocity of gas which results in a great contrast in acoustic impedance from the non-gas filled sediments. A phase reversal can appear as a reflector enters a hydrocarbon reservoir. This affect the reflection coefficient of the reflector and can cause the amplitude to reverse from negative to positive or opposite. A dim spot is similar to a phase reversal, However, the change in acoustic impedance is not enough to reverse the signal, resulting in a low amplitude signal, or a dim spot. A flat spot often represent fluid contact boundaries caused by density differences in a reservoir and is therefore often flat. For example, water to gas where the gas will lay on top of the water, which appear as a flat reflector in a seismic profile (Figure 16).

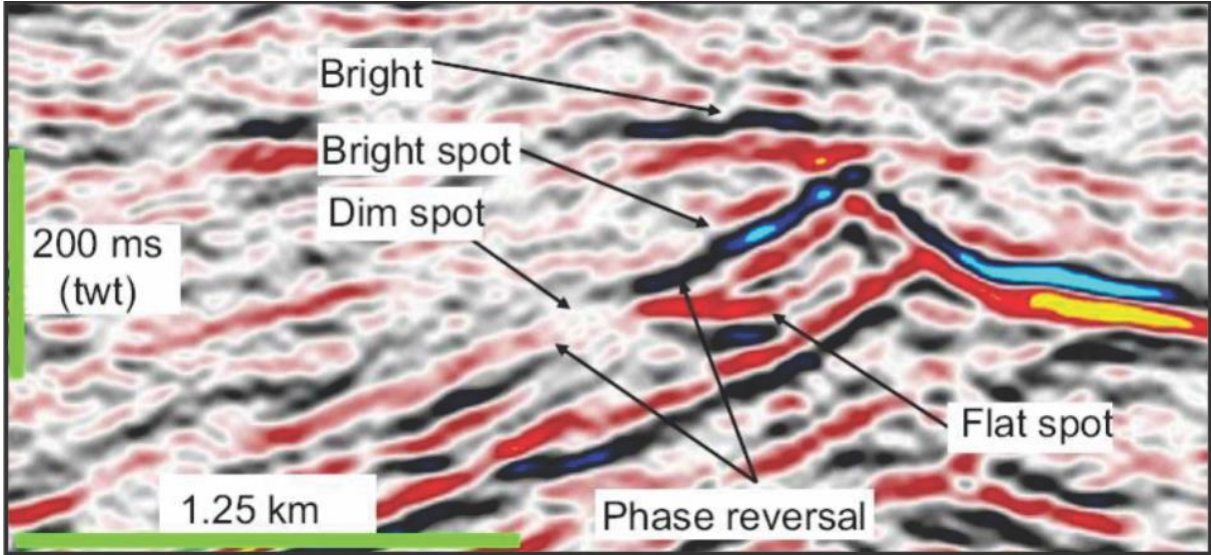


Figure 16 Indicators of fluids in a hydrocarbon reservoir. Figure from (Løseth et al., 2009)

Evidence of vertical fluid migration often appear as chimneys or pipes (Figure 17). These structures are vertically zones of acoustic transparency or disrupted reflections as well as high amplitude anomalies (Petersen et al., 2010) (Figure 17). These features are often found in relations to pockmarks on the seabed or on a buried surface.

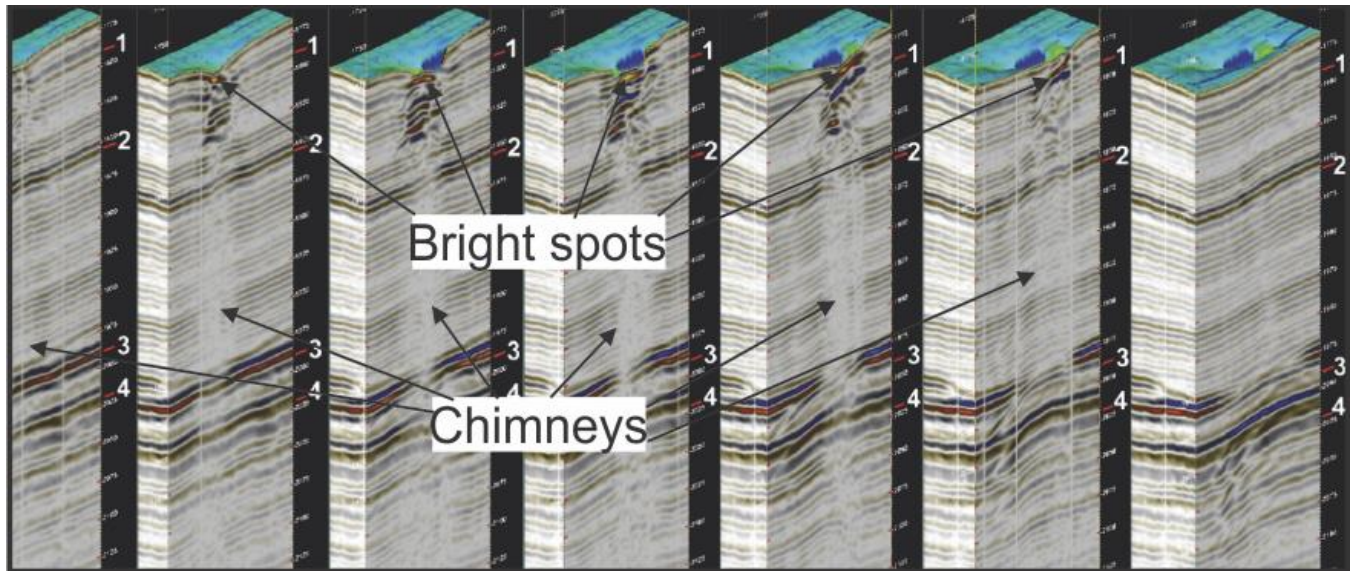


Figure 17 Indicators of vertical fluid migration. Figure modified from Petersen et al., (2010)

There are several indications for fluid flow and seepage in the SW Barents Sea. Pockmarks located on the seabed can indicate former or present leakage of fluids (Figure 18). These landforms are circular depressions often around 35 m in diameter and up to 2 m deep (Chand et al., 2012). In the Loppa High area, pockmarks occur randomly on the seabed, but have also been found in association with iceberg ploughmarks (Figure 18) (Chand et al., 2012). Pockmarks on the seabed are observed to cut glaciomarine sediments a few milliseconds underneath the seabed, arguing that they formed by seeping of fluids (Chand et al., 2012). Hydroacoustic water column data from the same study has also been used for detecting present acoustic gas flairs. The flairs are up to 200 m tall and they are often found outside of pockmark areas (Figure 18).

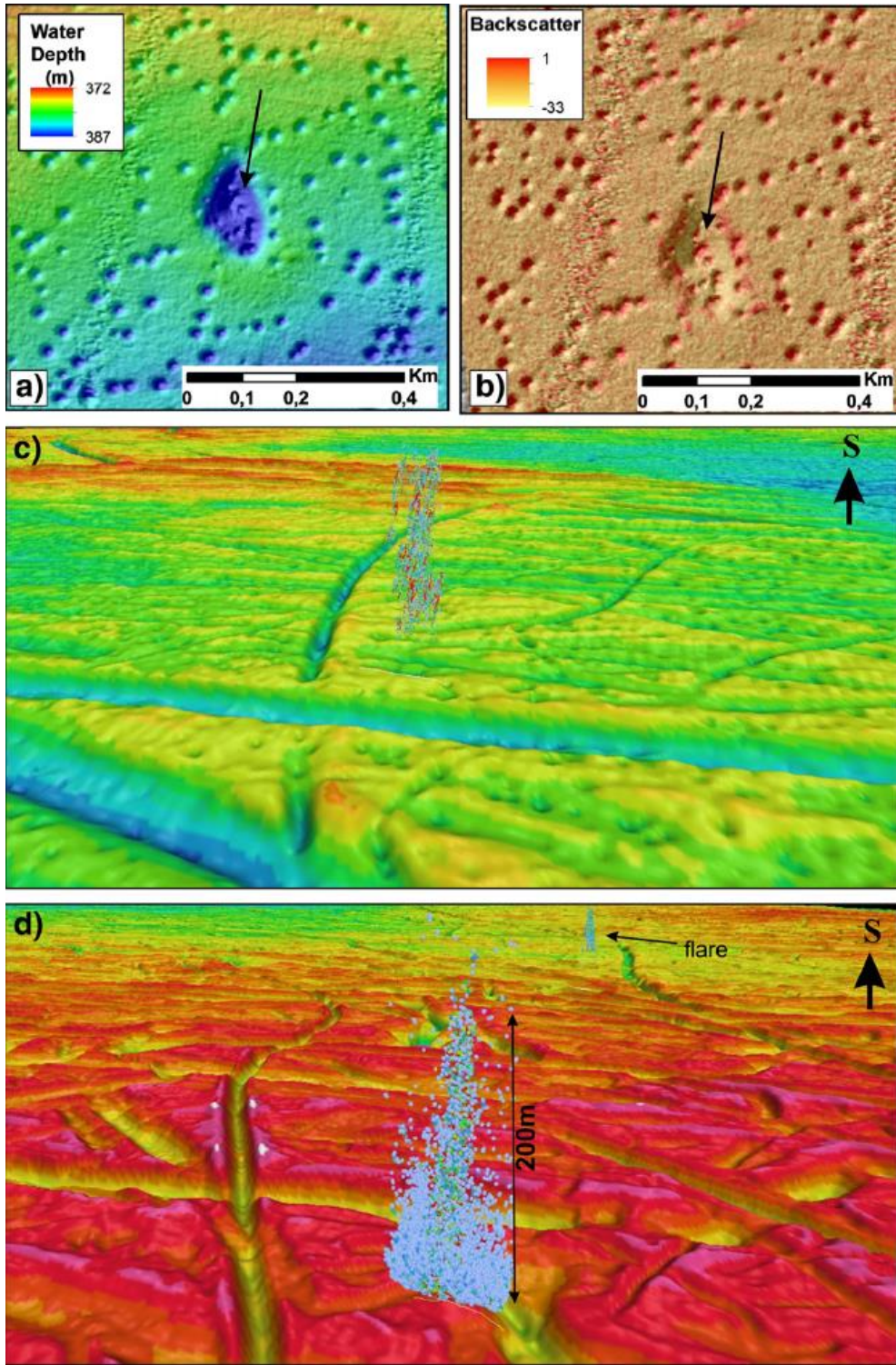


Figure 18 Pockmarks and flairs detected on the seabed in the Loppa High area, SW Barents Sea. Figure from (Chand et al., 2012)

2 Data and methods

2.1 Dataset

This study is based on industry 3D seismic dataset DN 14001 located on the confluence of the Loppa High, Bjørnøyrenna Fault Complex and the Bjørnøya Basin. The seismic dataset was acquired for “Det Norske Oljeselskap as”, 26 May – 24 July 2014 and lies within exploration license 715 on the Norwegian Continental Shelf.

2.2 Seismic reflection theory

Seismic reflection is a geophysical method used to map geological structures in the subsurface. By generating an acoustic pulse with an artificial source, the acoustic energy propagates into the subsurface and reflects from different interfaces referred to as reflectors. The energy reflected is then recorded by one or more receivers where the travel time from the source to the receiver is measured along with the amplitude of the signal. The acoustic properties of a material are defined as the acoustic impedance (z) and is a product of the acoustic velocity (v) and the density (ρ) (equation 1). The velocity is often the most important factor. For example in a porous sandstone, the content of the pore fluid will affect the velocity much more than the density of the rock.

Equation 1:
$$z = v * \rho$$

Where z = acoustic impedance, v = acoustic velocity and ρ = density of the material

The strength of the reflecting signal is dependent on the acoustic impedance contrast between two materials. This is defined as the reflection coefficient (R) and usually represent bedding planes, unconformities and or pore content in a porous rock. The reflection coefficient (R) is a relation between acoustic impedance between two layers (z_1 and z_2) and is given by the equation:

Equation 2:
$$R = \frac{(z_2 - z_1)}{(z_2 + z_1)}$$

Where R = reflection coefficient, z_1 = acoustic impedance of overlaying material, z_2 = acoustic impedance underlying material

The reflection coefficient can be both negative and positive and in general $z_2 > z_1$ indicate positive reflection coefficient and “softer rock” overlaying “harder rock”. However, there are many exceptions. For example fluid content in a porous sand stone. If a gas filled sandstone overlies water filled sandstone, this will result in a lower acoustic impedance for the gas filled sand vs the water filled sand and therefore result in a negative reflection coefficient even though the “hardness” of the two layers are roughly the same.

2.3 Seismic resolution

Seismic resolution is defined as the minimum distance two objects must have to be detected as two separate objects (Sheriff, 1985). There are two aspects of seismic resolution, vertical and horizontal both of which are dependent on the dominant seismic wavelength of the survey. The wavelength (λ) is given by equation 3:

Equation 3:
$$\lambda = v/f$$

Where λ = wavelength, v = acoustic velocity and f = dominant frequency

Thus, wavelength is dependent on acoustic velocity and the frequency of the signal. In general, the acoustic velocity increases and the frequency decreases with depth (Figure 19), resulting in longer wavelengths, hence the resolution decreases with depth which means that objects that are deeper in the sub surface needs to be larger to be detected in a seismic image compared to those in shallow subsurface (Brown, 2011). This applies for both aspects of resolution, vertical and horizontal resolution.

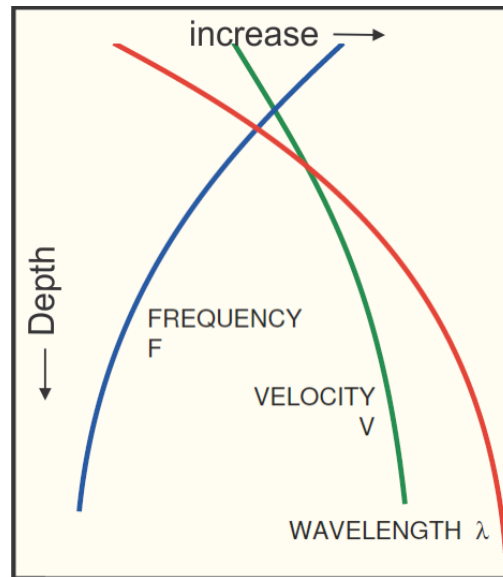


Figure 19 General relation between depth and frequency, velocity and wavelength. Figure modified from Brown, (2011).

2.3.1 Vertical resolution

The vertical seismic resolution is defined as the minimum vertical distance two interfaces must have between each other and still be imaged as two separate interfaces in a seismic section. This is also called the resolvable limit and is defined by (Sheriff, 1985). The vertical resolution is defined as:

Equation 4:
$$Vr = \frac{\lambda}{4}$$

Vr = vertical resolution and λ = wavelength

Figure 20 illustrate how the thickness of $\frac{1}{4} \lambda$ appear in a seismic section. $\frac{1}{2} \lambda$ is the point where there is no interference between the two interfaces (Figure 20). $\frac{1}{4} \lambda$ however, is where there is maximum interference and the smallest vertical distance where the two interfaces can be distinguished from each other. At distances smaller than $\frac{1}{4} \lambda$, the wavelets will have negative interference and thus cannot be distinguished as two separate layers. At $\frac{1}{30} \lambda$ is the minimum interference where there will be no reflection (Figure 20).

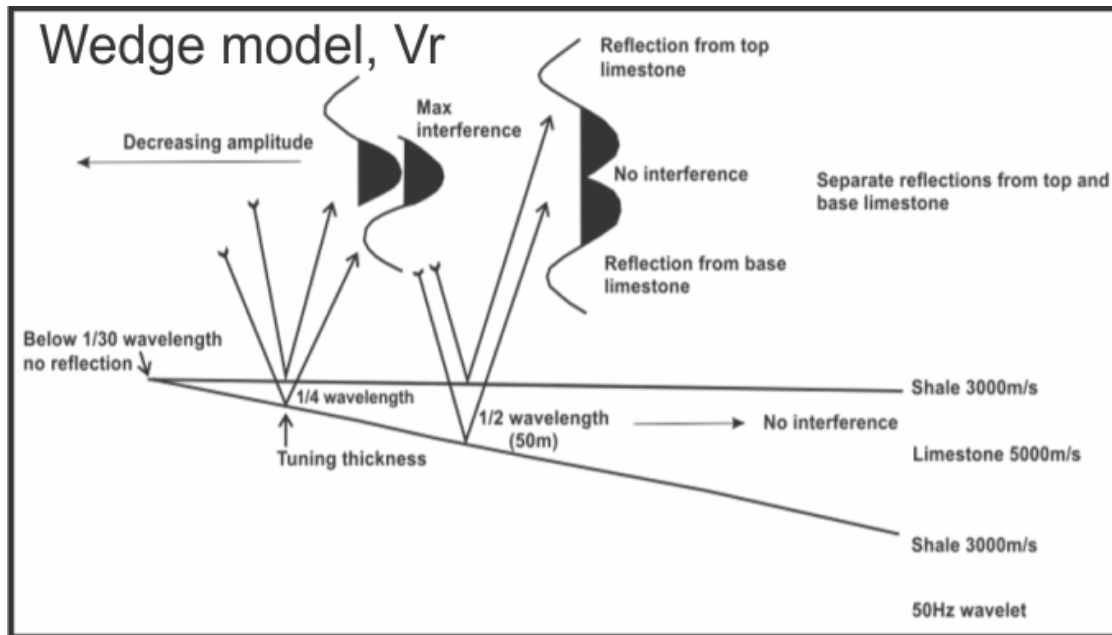


Figure 20 Wedge model illustrating interference effect between two high layers of different velocity. Figure modified from Badley & Gibson, (1987).

2.3.2 Horizontal resolution

The horizontal resolution is also known as the lateral resolution and refers to the minimum lateral distance between two objects where they can still be separately detected in a seismic image. For unmigrated seismic data, the horizontal seismic resolution is defined as the radius of the Fresnel zone (Figure 21). However, an acoustic pulse propagates in wave fronts rather than single rays which results in several wave fronts reflecting on the same reflector and at different times. This zone is limited by $\frac{1}{4} \lambda$, where the first wave front arrives at the reflector $\frac{1}{4} \lambda$ before the last (Figure 21 a). This zone is called the first Fresnel zone. However, the Fresnel zone is approximated from the following equation:

Equation 5:
$$rf = \frac{v}{2} * \sqrt{\frac{t}{f}}$$

Where rf = radius of Fresnell zone, v = acoustic velocity, t = two way travel time and f = dominant frequency

If the frequency decreases and the velocity increases, the wavelength and the diameter of the first Fresnel zone increases as well as the horizontal resolution decreases (Figure 21 b).

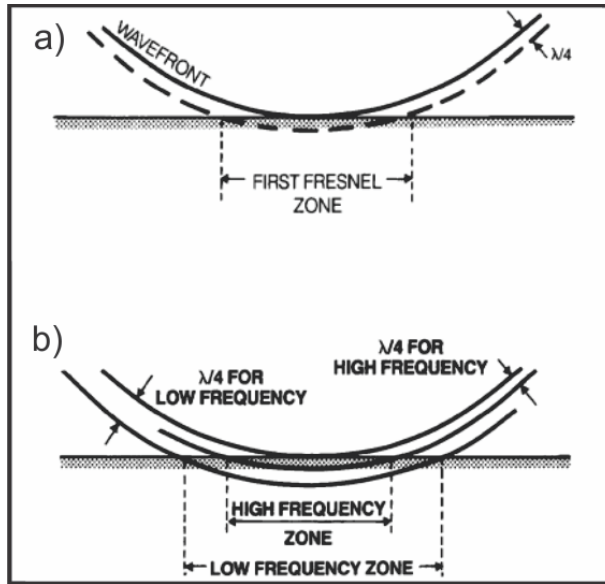


Figure 21 illustrating the Fresnel zone, Figure modified by Sheriff, (1985).

Migration is a seismic processing technique used to increase the horizontal resolution. 2D migration collapses the Fresnel zone in inline direction and the resolution is now basically determined by the receiver spacing of the seismic array (Kearey et al., 2013). In xline direction, the horizontal resolution will still be equal to the Fresnel zone for 2D data (Figure 22).

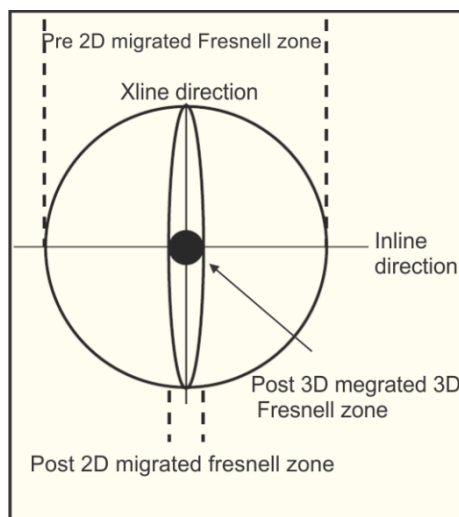


Figure 22 illustrate the Fresnell zone pre and post migration

For this thesis 3D seismic data is used. Here the data is sorted into discrete areas also known as bins. All the midpoints that fall within the same bin area are stacked to one stacked trace and represent that bin (Figure 23). The inline and crossline interval decide the size of the bin

area and the horizontal resolution for a migrated 3D seismic survey is therefore equal to the bin spacing of the survey (Liner, 1999).

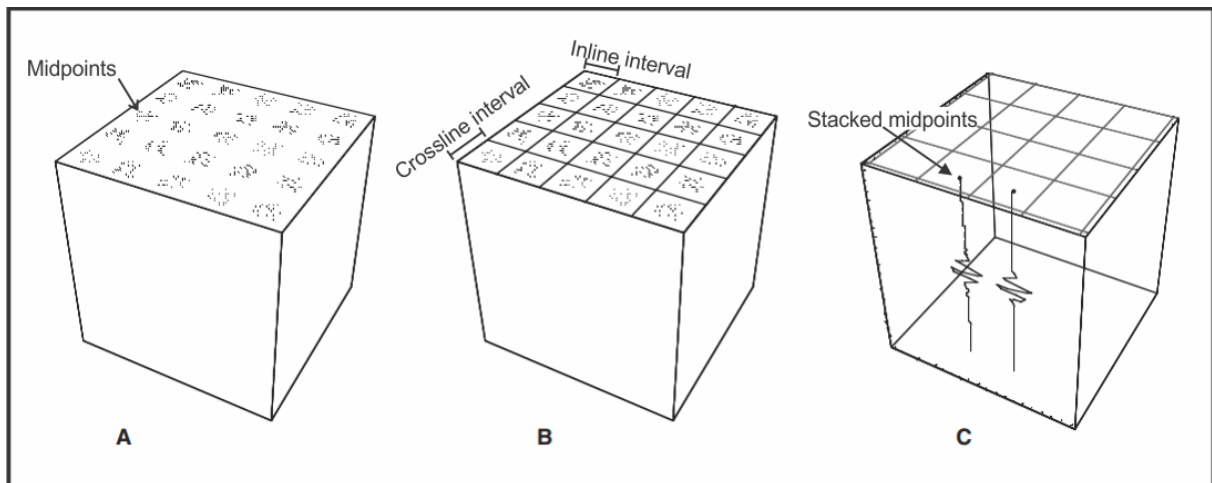


Figure 23 illustrate how midpoints are organized in bins and stacked to improve the signal to noise ratio. The horizontal resolution of a 3D seismic survey equals the bin size. Figure modified from Liner, (1999)

2.3.3 Vertical and horizontal resolution of the DN14001 survey

The vertical and horizontal resolution for the 3D seismic dataset used in this study was calculated using equations 3, 4 and 5 and the results are listed in Table 1. To be able to determine the wavelength the peak frequency is determined from each surface. This is done by a peak frequency analysis from the surfaces. In this study, the peak frequency is measured from to be 50 Hz for the URU surface and 54 Hz for the intra Quaternary horizon surface (Figure 24). The velocity for Quaternary glaciegenic sediments is set to 2000 m/s (Andreassen et al., 2007). The horizontal resolution for DN14001 is defined by the bin spacing of the survey. In this case the inline interval is 6,249m and the crossline interval is 6,250 m. The bin spacing and the horizontal resolution is therefore 6,25 m.

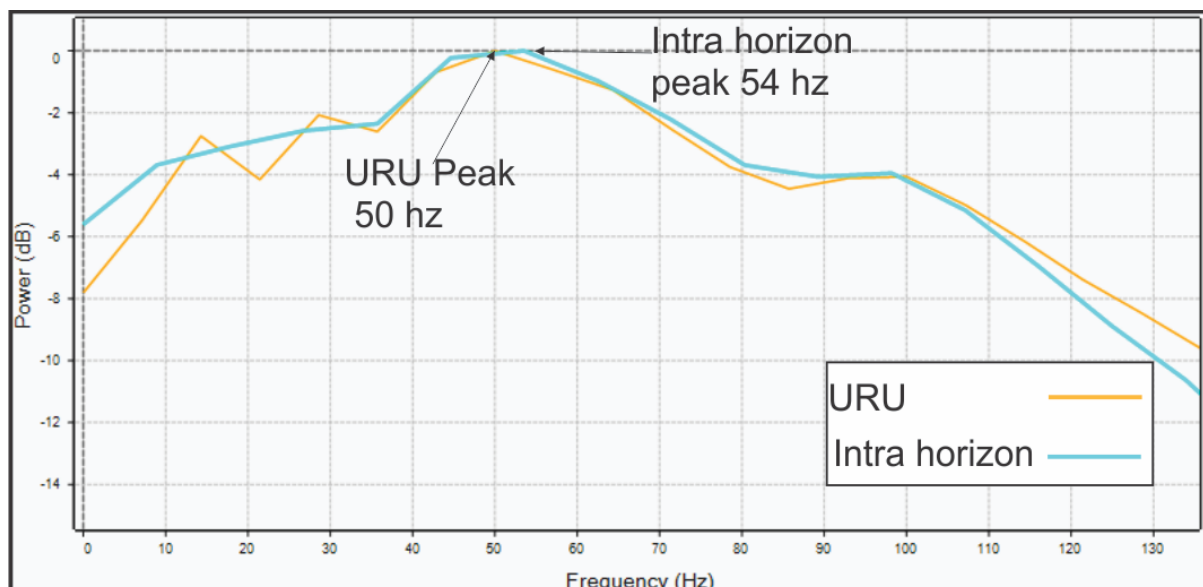


Figure 24 Peak frequency analysis for URU and intra Quaternary horizon.

Table 1 Acoustic velocity, frequency, wavelength and vertical resolution for the two surfaces Intra horizon and URU

Surface	Velocity [m/s]	Depth [s]	Frequency [hz]	Wavelength [m]	$V_r = \frac{\lambda}{4}$ [m]	Hr, pre migration [m]	Hr, post migration [m]
Intra horizon	2000	0,63	54	37	9,25	108,01	6,5
URU	2000	0,65	50	40	10	114,02	6,5

2.4 Interpretation tools and methods

In this thesis, Petrel 2019 software has been the main program for visualization and interpretation of the data. Within Petrel different tools and attributes have been used for seismic interpretation. Fledermaus has also been used for visualization of surfaces and to generate cross profiles over landforms. Corel draw 2017 has been the main tool for making and modifying Figures.

2.4.1 Seismic attributes

Seismic attributes are quantitative measures of a seismic characteristic of interest and are used to enhance different aspects of geological features (Chopra & Marfurt, 2005). Different types of attributes can be applied to surfaces or volume in form of “surface attributes” and “volume attributes”.

RMS amplitude is a type of attribute applied to surfaces in this thesis. It sums the root mean square of all the trace samples within a given search window. This attribute is useful to map features arising from high amplitudes. Features with high anomalies can be large bedrock clasts within a sedimentary unit. Gas accumulations and BSR also results in high amplitude reflections. RMS amplitude attribute has been applied to the intra Quaternary horizon surface and the URU surface.

Variance attribute emphasizes lateral discontinuities of amplitude and is good for mapping geological features that have an abrupt lateral change (Pigott et al., 2013). This can typically be faults, river channels or lenses of coarser material. Gas accumulations will also be emphasized in a variance volume. Variance volume attribute has been generated where time slices is used for mapping of faults and pock marks.

2.5 Artefacts

The DN14001 survey used in this thesis contain artefacts which can be seen as inline troughs and ridges and can be traced from south to north in the eastern parts of the dataset. They are also seen on all the three interpreted surfaces (Figure 25). In a seismic section they could be misinterpreted as faults (Figure 25). The artefacts are believed to be a result of bad processing and a lack of tidal static corrections.

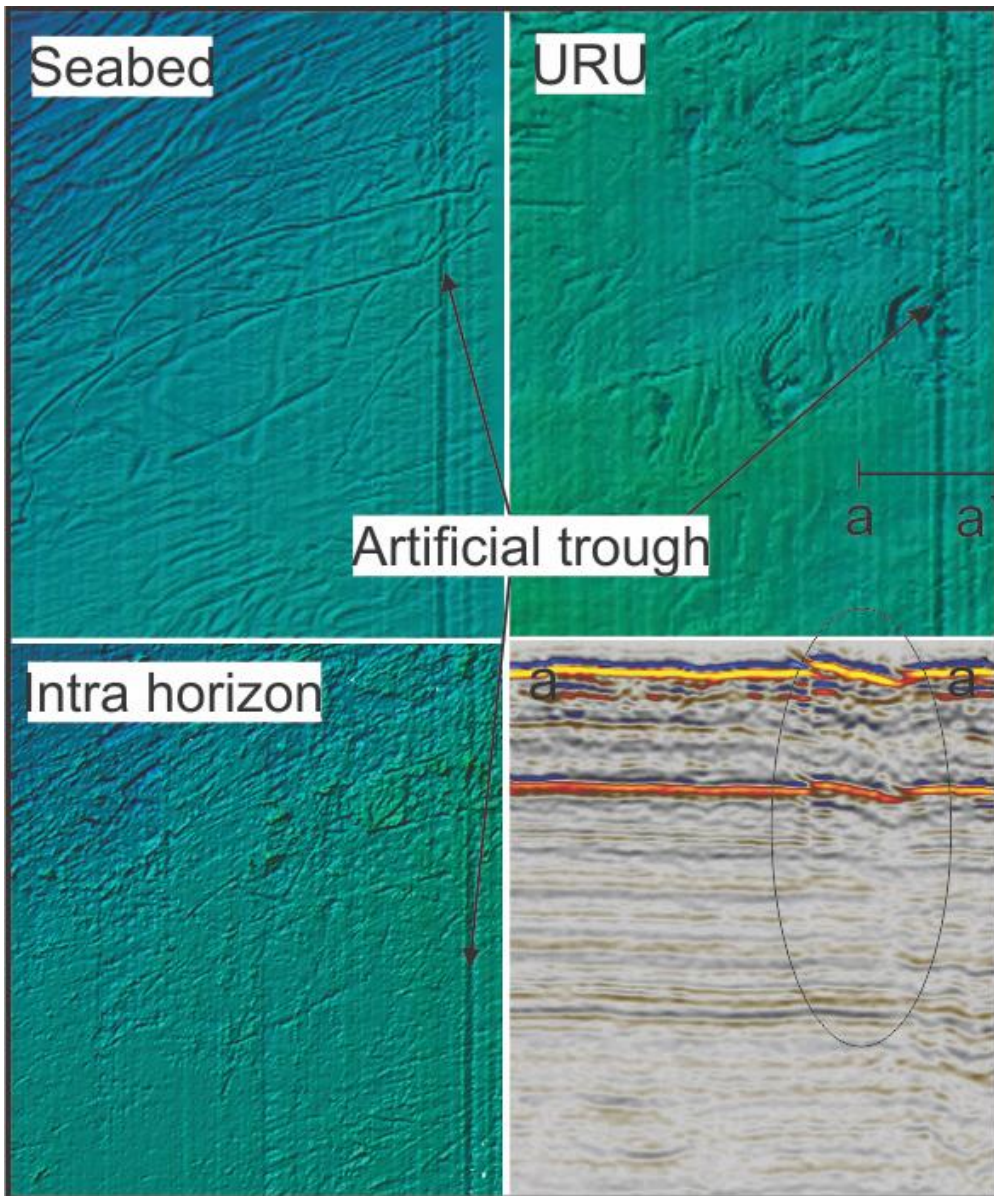


Figure 25 Artefacts that can be seen on all three surfaces

3 Results

This chapter presents the results of the seismic analysis of the DN14001 dataset. Three different horizons have been interpreted. These are the seabed horizon, the upper regional unconformity (URU) and an intra Quaternary horizon. Along with these horizons, several time slices from different seismic attributes volumes are used to present the results of this study.

3.1 Seabed horizon

The seabed horizon is identified as the stratigraphically uppermost, strong positive reflector, and can easily be traced over the entire dataset (Figure 26 and 27). The seabed horizon was converted from two way travel time (TWT) to depth by assuming a constant acoustic velocity of 1500 m/s (the acoustic velocity of seawater). The water depth of the seabed gradually deepens towards the north-west, reaching a maximum depth of 470 meter. The shallowest areas are in the south-east where the water depth is 350 meters (Figure 26). The dominant geomorphic feature observed on the seabed surface are curved lineations. They are observed in different sizes, shapes and orientations and will be described in the following section.

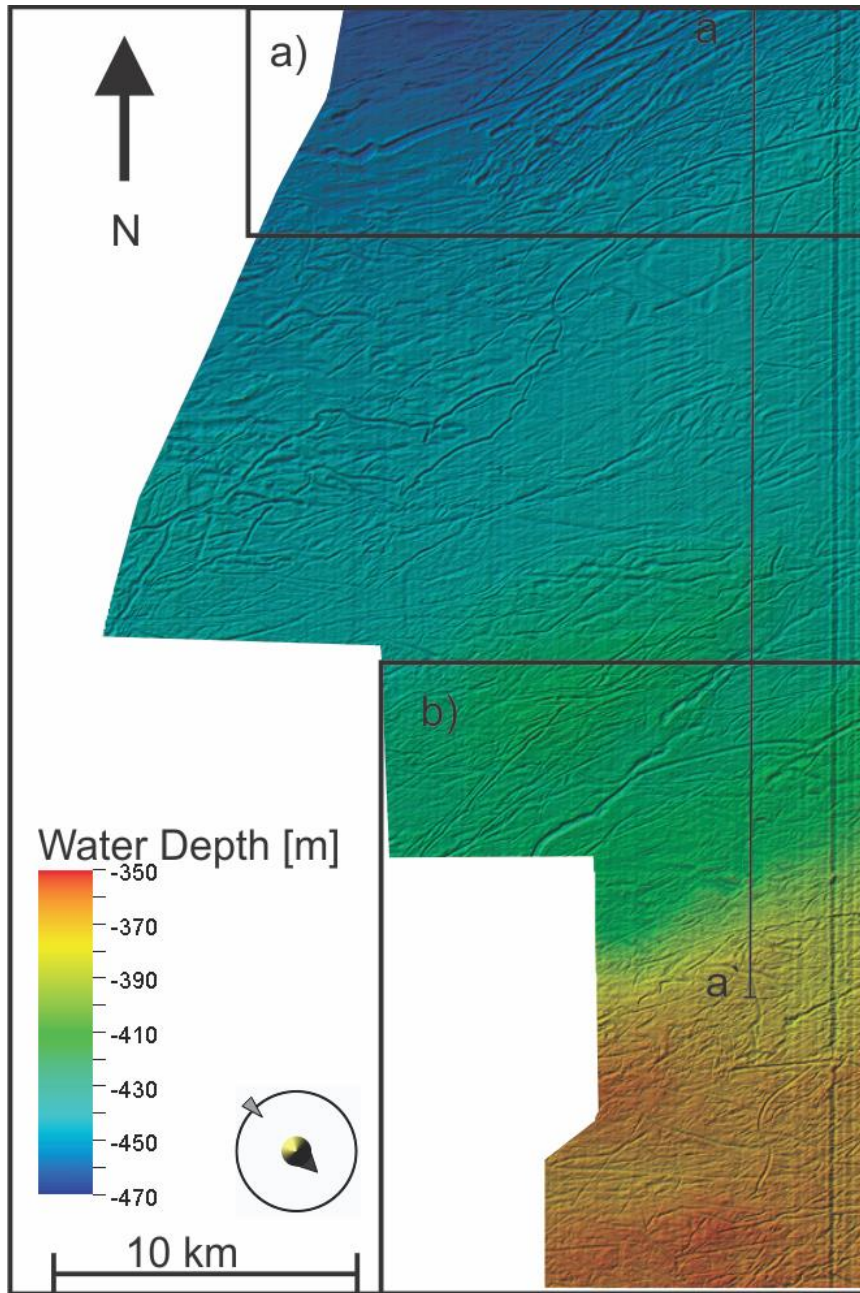


Figure 26 Overview of the Seabed surface. The surface is subdivided into section a) and section b) and will be further described. Profile a-a' can be viewed in Figure 27

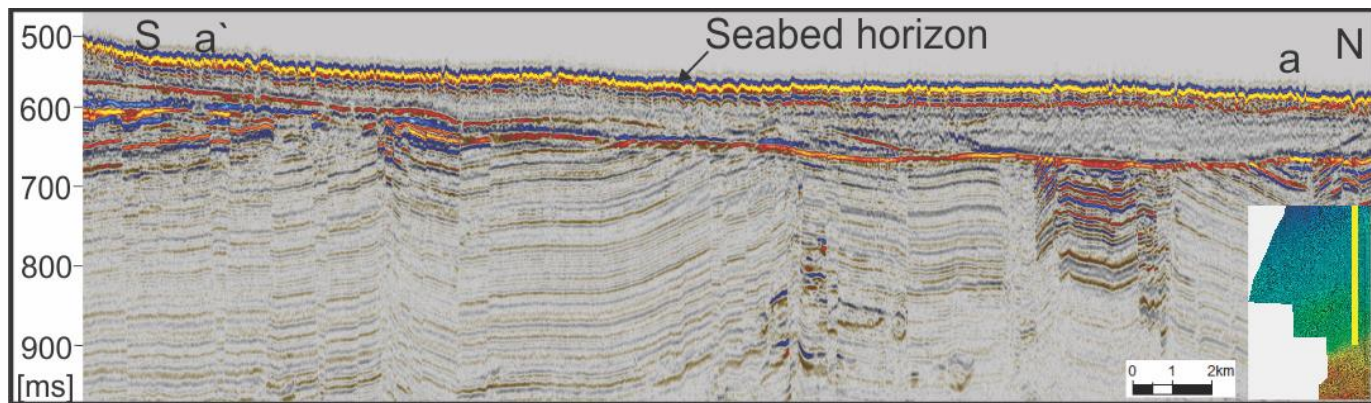


Figure 27 Seismic inline profile illustrate how the seabed horizon easily can be traced across the dataset

3.1.1 Curved Lineations on the Seabed: Description

Two types of curved lineations are found on the seabed surface. The size, depth and distribution divides them into two categories, small and large curved lineations.

Small curved lineations are distributed all over the seabed surface. However they are most abundant in the shallow southern parts of the surface. The small curved lineations have a length from 920 – 12600 meters (Figure 28), but they are difficult to measure as they are overprinted by other curved lineations. The relief varies, and is observed to be from 4 ms to 20 ms (TWT) and thus effect the top 20 ms of glacial strata. Their orientation are rather random, and are observed in all orientations. However, the general trend of the small curved lineations are north-east, south-west.

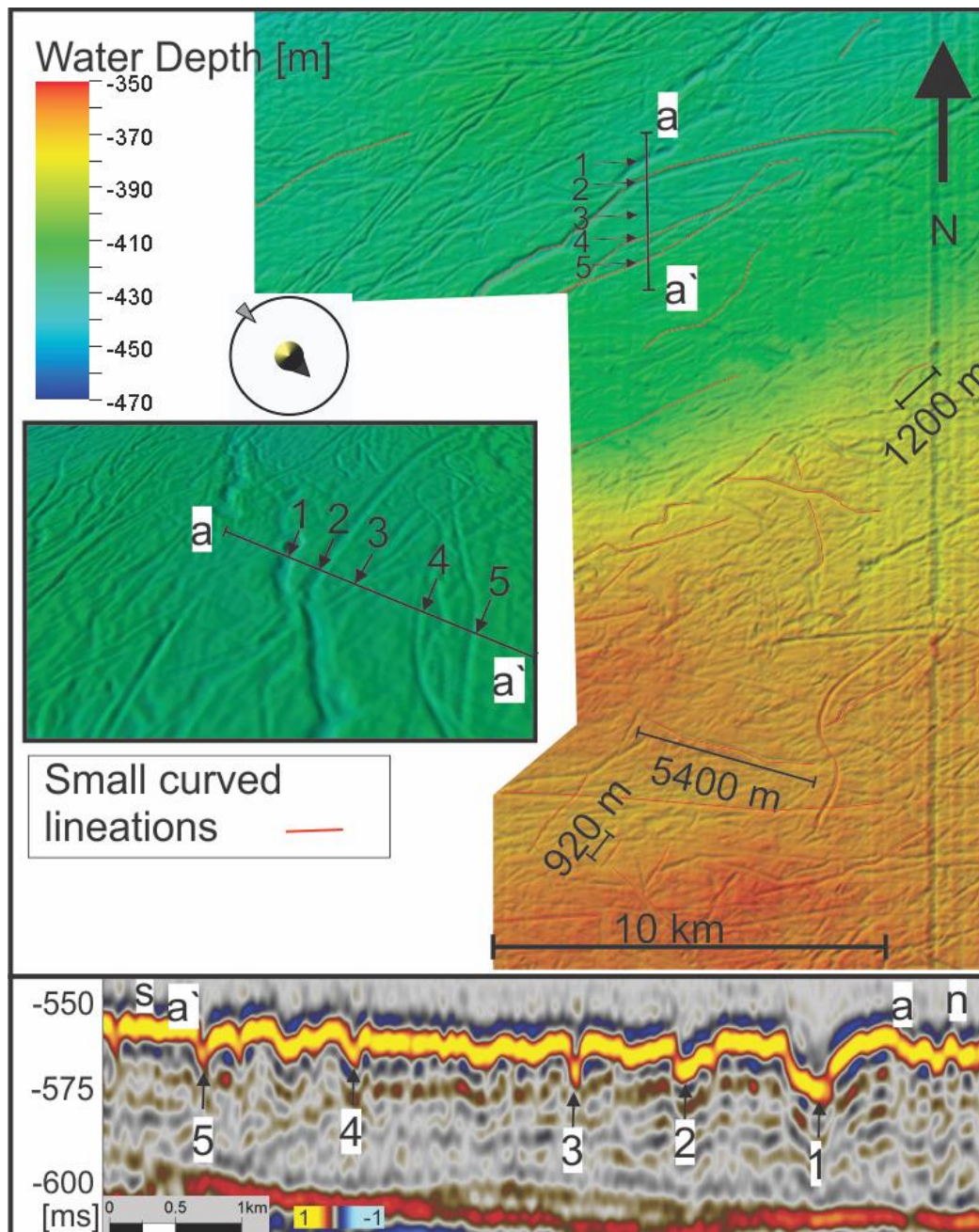


Figure 28 Small curved lineations on the seabed surface. Profile a - a` show a inline profile crossing 5 small curved lineations

Large curved lineations are abundant in areas across most of the seabed surface, but are most abundant in the deepest northern parts. The relief of the large curved lineations is similar to the smaller lineations and observed to be approximately 7 - 35 ms (Figure 29). The length of the large lineations is observed to be longer than 15 km, thus most of these lineations extends beyond the dataset. Their width varies from 200 meters and up to 600 meters (Figure 29). In general, the largest curved lineations is found in the deepest parts (Figure 29). The orientation

of the large lineations is much more consistent compared to the smaller curved lineations. They appear in a north-east, south-west direction with some variations (Figure 29). In the northern parts of the dataset there are two sets of large curved lineations with different orientation resulting in crossing and overprinting of each other (Figure 29). Lineations set 1 is oriented 62 degrees north-east while lineation set 2 is oriented 50 degrees north-east. The widest lineation belong to lineation set 1, and has a width of 600 meters and a length of over 15 km (extends beyond the dataset) (Figure 29). At the base of the largest lineation there are two parallel internal lineations, following its orientation and outline (Figure 29). This lineations overprint lineation set 2 (Figure 29). Lineation set 2 consist of deep lineations with a 50 degrees orientation north-east.

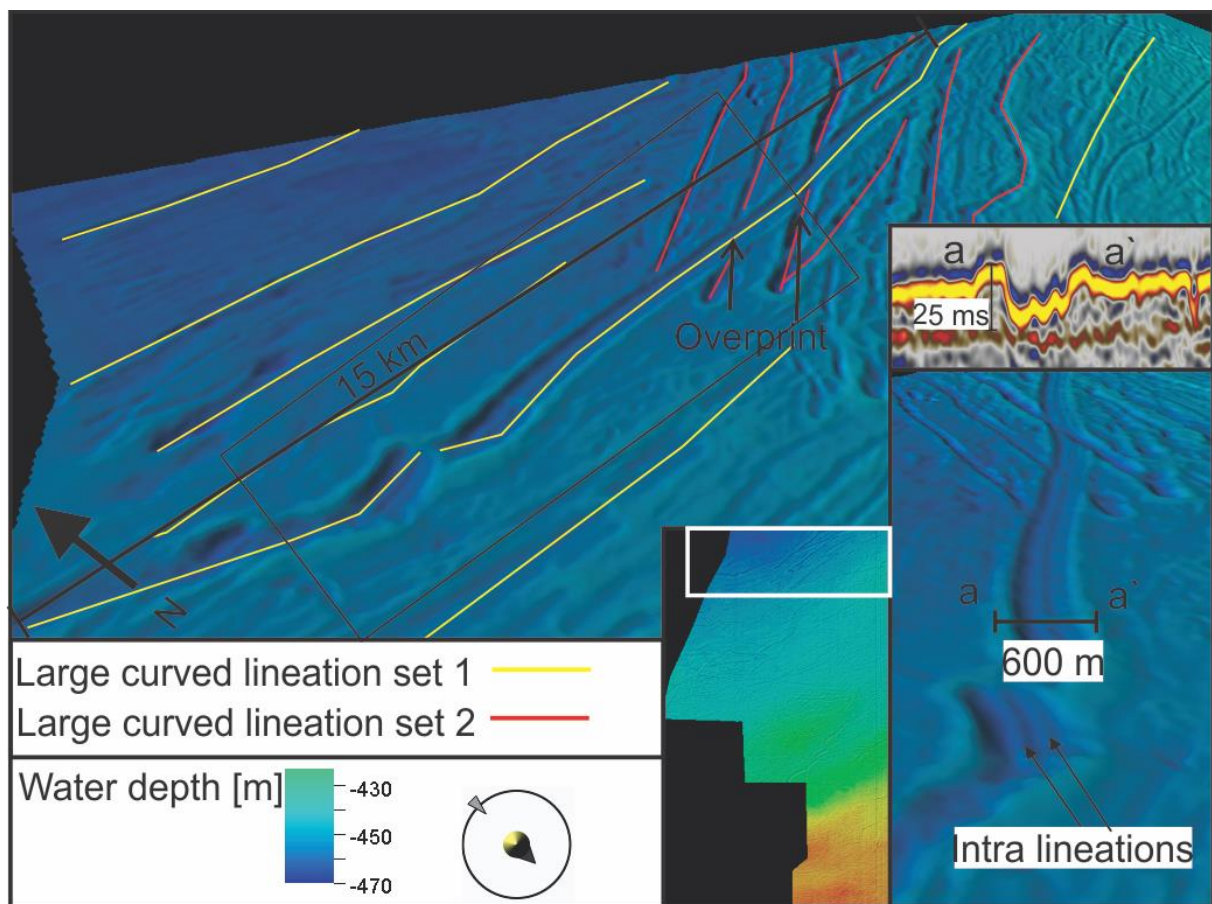


Figure 29 Large curved lineations on the seabed surface.

3.1.2 Curved lineations on the Seabed: interpretation

The curved lineations observed on the seabed ranges in size, shape and orientation, and have been interpreted as iceberg ploughmarks. Their irregular shape and size are typical for ploughmarks found on the Barents Sea continental shelf (e.g. (Shackleton et al., 2020),

(Hogan et al., 2010)). The size of the ploughmarks seems to increase with water depth, with some exceptions. This is because deeper waters require larger icebergs to reach the seabed sediments. In the shallower parts, smaller icebergs will reach the seabed while larger icebergs might get stranded and prevented to reach these areas. The shallow areas are believed to be dominated by smaller ploughmarks for this reason. The ploughmarks in the shallow southern areas are similar to small ice berg ploughmarks described by (Shackleton et al., 2020), in Storfjordrenna just north for Bjørnøyrenna. In the northern parts, the large curved lineations set 1 is interpreted to be from large multiple keel icebergs while the lineation set 2 are formed by large single keel icebergs. Since lineation set 1 is overprinted by lineation set 2, the curved lineation set 1 is believed to be the youngest of the two sets.

3.2 Upper regional unconformity (URU)

The URU reflector is a strong positive reflector, which separates (unconformably) overlying glacial sediments from underlying dipping tertiary sedimentary bedrock. In the dataset the URU surface reaches from -762 ms to -558 ms in depth and is easy to trace in most parts of the dataset with exceptions from the southern parts (Figure 30 and 31). In the same way as the seabed, the depth (two way travel time [ms]) increases from south to north-west of the dataset (Figure 30).

The surface has been divided into three areas which has different characteristics. In the northern parts (Figure 30 a) the surface consists of positive relief ridges with different orientation where high RMS amplitudes are observed along several of these ridges. Towards west, the ridges terminate along a south-west north-east oriented negative relief depression. Within this elongated depression, there are several internal landforms. In the central parts (Figure 30 b)) the URU surface contain curved lineations with different orientation, in addition to circular depressions (Figure 30 b)). Four other circular depressions are found in the north-west and south-east parts of the dataset. In the southern parts, pre-Quaternary strata truncate URU surface, which results in positive interference. This was a challenge while interpreting and may have resulted in “staircase” structures in some areas (Figure 30 c) and 27).

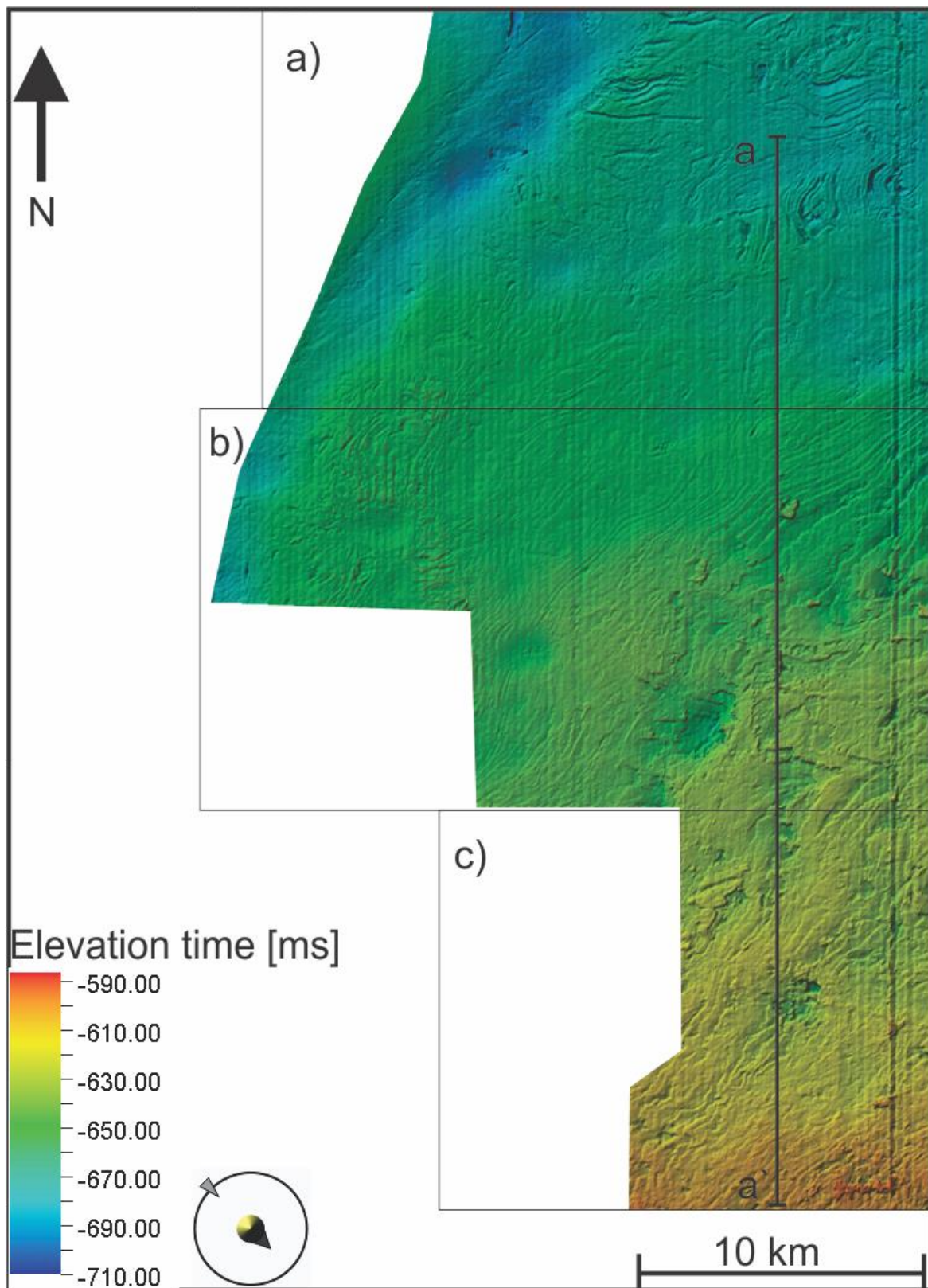


Figure 30 Overview map of the URU surface, inline profile a - a` can be seen in Figure 31. Illumination from north west

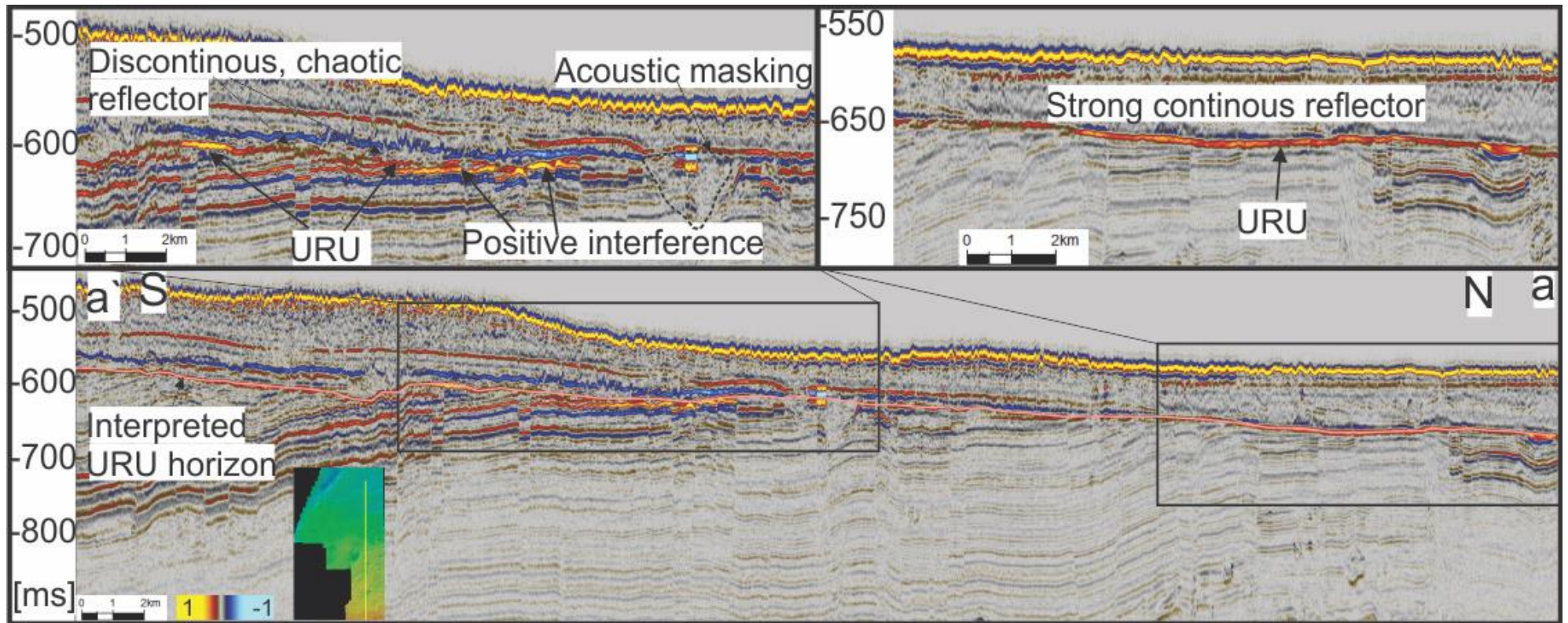


Figure 31 Inline profile, showing how the URU horizon changes along the dataset

3.2.1 Curved ridges: description

Curved ridges are found in the northern parts of the URU surface (Figure 32 a). They range in length from 0,8 to 10 km. The width measured from ridge to ridge (Figure 32 a-a`) varies from 140 meters up to 800 meters. Relief on the curved ridges is about 10 ms (Figure 32 profile a – a`). In relation to each other, they appear sub parallel and can be grouped into two different sets with different orientations. First group has a strike orientation of north-south (Figure 32 profile b – b`), while the second one is east-west striking (Figure 32 and 33 profile c – c`). Viewed in a seismic section (Figure 33 profile c – c`) reflectors from a pre-Quaternary folded strata are truncated by URU and appear as ridges on the surface. The same truncation trend can be seen for the east-west striking ridges (Figure 32 b – b`).

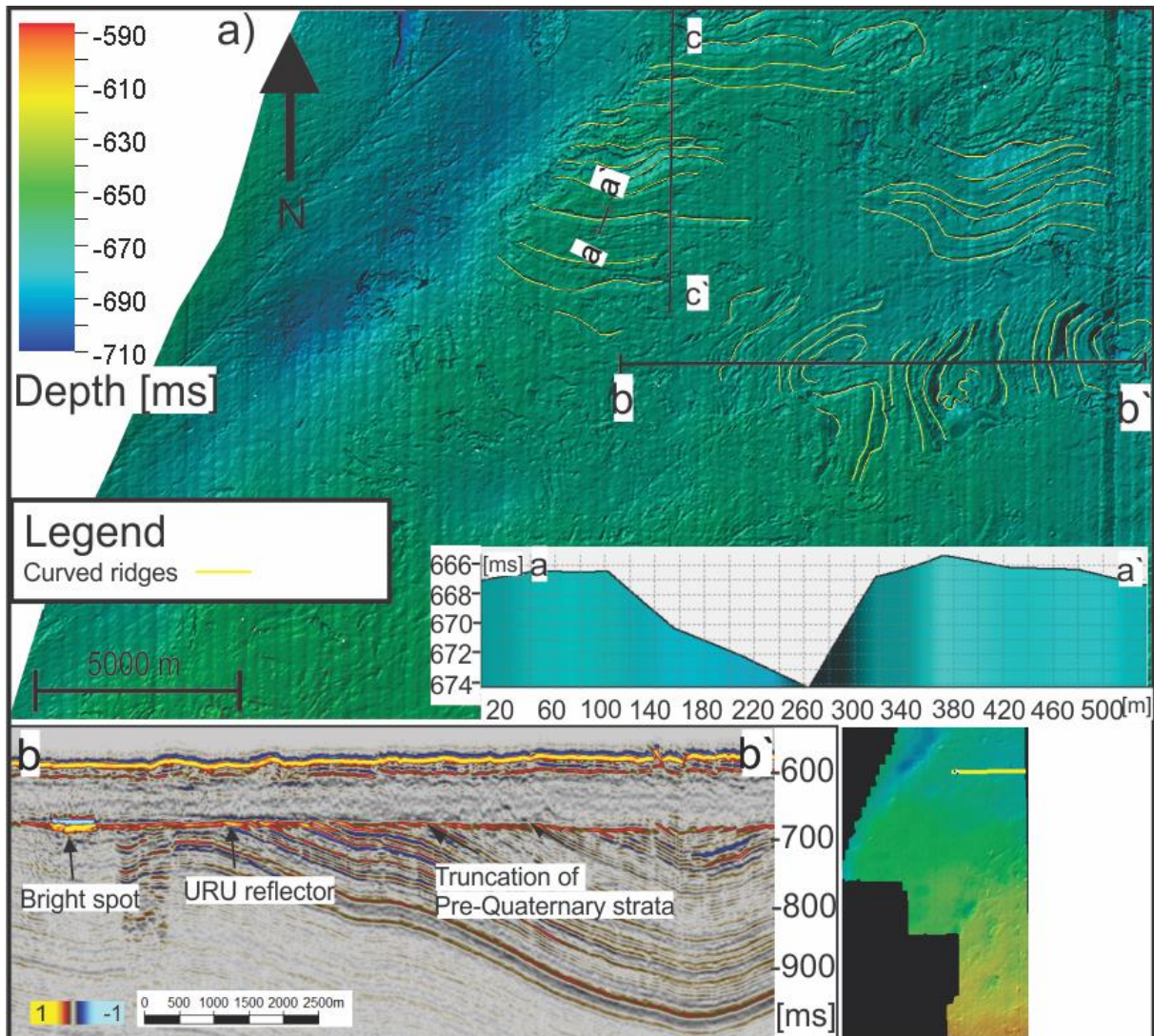


Figure 32 Curved ridges located in the northern parts of the URU surface

3.2.2 Curved ridges on the URU surface: interpretation

The curved ridges are interpreted as bedrock ridges from pre-Quaternary strata. The folded pre-Quaternary stratification in this area is believed to consist of interbeds of soft erodible and harder more erosional resistant bedrock (NPD, 2020). As glacial erosion has cut the folded Pre-Quaternary strata the geological differences between the interbeds of the sedimentary bedrock results in bedrock ridges on the URU surface. The north-south striking ridges are formed by truncation of a syn-form fold, while the east-west striking ridges are from faulted sedimentary bedrock within a syn-form fold (Figure 33 and 32).

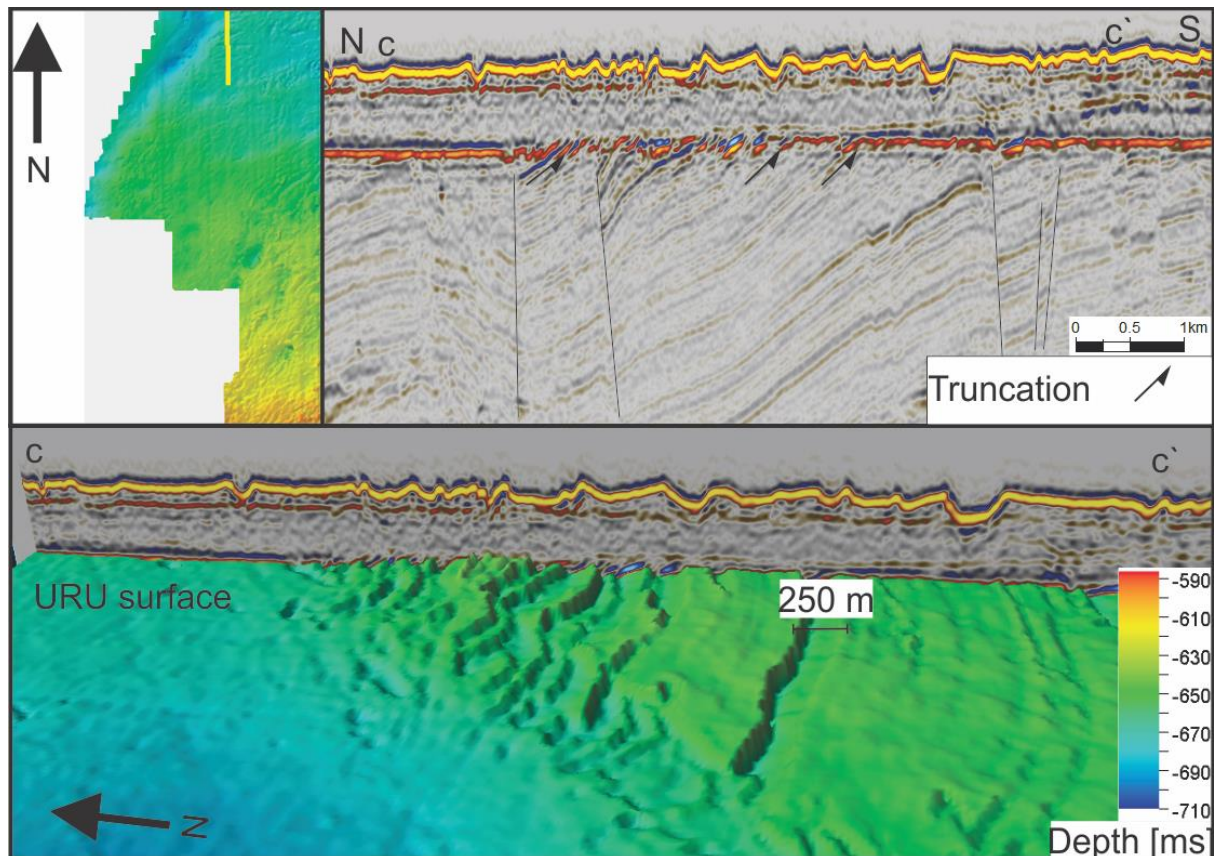


Figure 33 Inline profile c – c', illustrating how syn-form folded Pre-Quaternary strata truncates the URU surface and forms bedrock ridges on the surface.

3.2.3 Elongated depression

A minimum 28 km long elongated depression, oriented south-west to north-east is seen on URU surface (Figure 34). The depression extends beyond the dataset in both north and south so measured here represent a minimum. The depression varies in depth from being deepest in

the north (35 ms relief) and shallowest in the south (8 ms relief). Along the depression the width varies from 3,5 – 10 km where the widest area is in the north and the narrowest is located in the south. On the eastern flank of the depression, the east west striking curved ridges (3.2.1 Curved ridges) terminates along the rim of the depression (Figure 34).

In a seismic profile the URU reflector on the eastern flank of the depression has a greater amplitude compared to the western flank (Figure 34). The URU reflector on the eastern flank is also less continuous compared to the western flank (Figure 34). Underneath the URU reflector, the underlying strata on the western side of the depression show different seismic characteristics compared to the eastern side. On the eastern side of the depression the underlying reflectors are relatively strong and continuous compared to the western flank of the depression where the reflectors are discontinuous and with lower amplitude (Figure 35). The seismic stratigraphy under the base of the elongated depression is chaotic and discontinuous. Along the URU reflector in this area is a large negative amplitude anomaly (Figure 35). This anomaly is located within a circular basin, which will be further discussed (section 3.2.7).

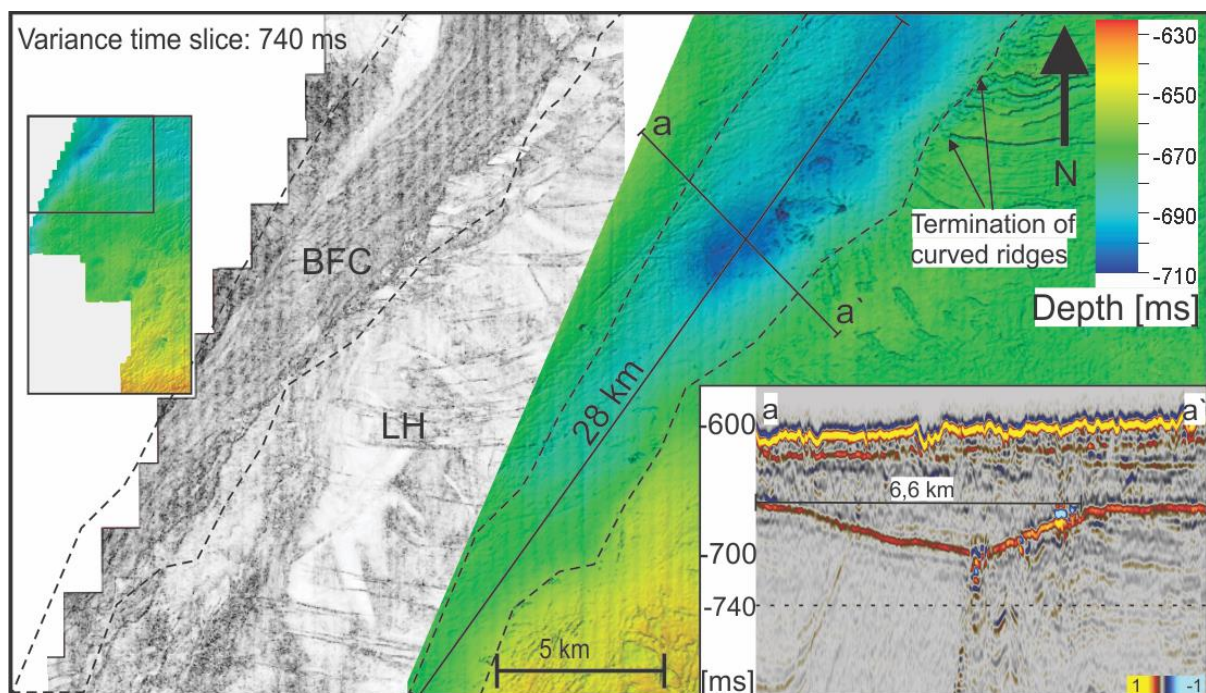


Figure 34 Elongated depression (stippled line) located in the northern parts of the dataset. Variance timeslice from 740 ms (dotted line in profile). Variance maps highlight lateral change in amplitude. Faults appear with high values on a variance map and reveal the Bjørnøyrenna Fault Complex (BFC).

3.2.4 Elongated depression: interpretation

The elongated depression is interpreted as a weakness zone less resistant to glacial erosion. This depression is located on the boundary between the Loppa High (LH) and the Bjørnøya Basin (BB) (Figure 35). From the seismic section (Figure 35) the continuous high amplitude strata in the east (Figure 35) belong to the LH structure, while the discontinuous low amplitude strata in the west (Figure 35) are from BB. Between these structural elements is the BFC. The elongated depression and the BFC share the same north-east south-west orientation and the elongated depression matches the outline of the BFC (Figure 35). It is therefore believed that the BFC work as a weakness zone which has been eroded deeper than the surrounding areas. The BFC reflects a transition zone between LH and the BB and has undergone several reactivations of deep seated faults since the early Mesozoic and throughout the Cenozoic (Gabrielsen et al., 1997). The bedrock in this area is therefore heavily faulted and more prone to glacial erosion than the surrounding.

The difference in amplitude of the URU reflector across the elongated depression is interpreted to be from geological differences between the LH and the BB. After the Late Kimmerian rifting when the BB formed, it was rapidly filled by organic rich mid-Jurassic shale before rapid subsidence then led to infill of early Cretaceous sediments (Faleide et al., 1993). Cretaceous sediments across the Barents Sea shelf are known to easily be eroded by glacier action. The LH however, consist of Triassic strata which is consisting of upward coarsening clay to sandstone, where sandstone is the most dominating grain size near our studyarea (NPD, 2020). The LH hence consist of older and harder rock than the BB and thus

appears as a higher amplitude in the seismic section across the elongated depression (Figure 35).

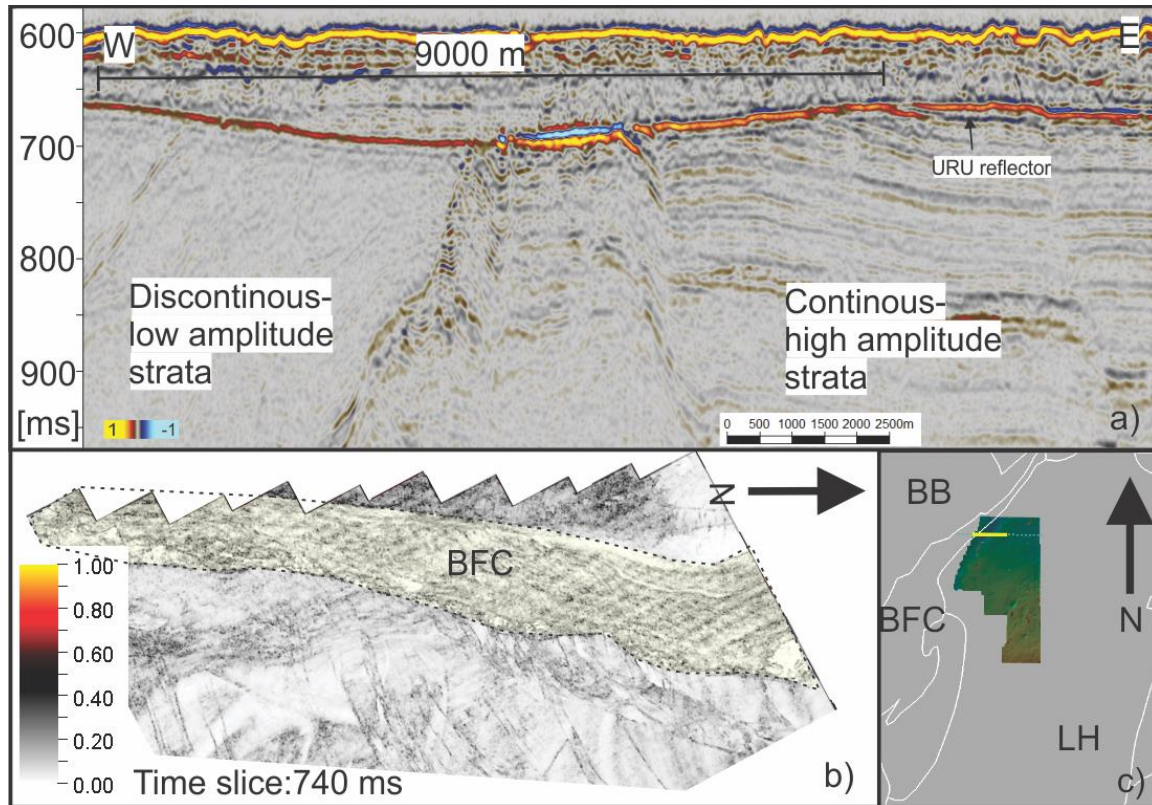


Figure 35 Profile of elongated depression. Section a) crossline cutting the elongated depression from west to east. Section b) Variance time slice from 740 ms showing the Bjørnøyrenna Fault Complex (BFC). Section c), overview maps of the seismic profile in relation to a structure map of the Barents sea provided by NPD.no/factmaps. LH, Loppa High, BFC, Bjørnøyrenna fault complex and BB, Bjørnøya Basin.

3.2.5 Steamlined Lineations within the Elongated: depression

Streamlined lineations are found within and along the flanks of the elongated depression.

These lineations have the same orientation as the depression and vary from 4400 m to more than 5580 m in length. Compared to the curved lineations found on the Seabed surface these are straight and unidirectional (Figure 36). From a profile of one of the lineations, the relief is -4,5 ms and the width is 200 meters with levees on the side (Figure 36 profile a – a`).

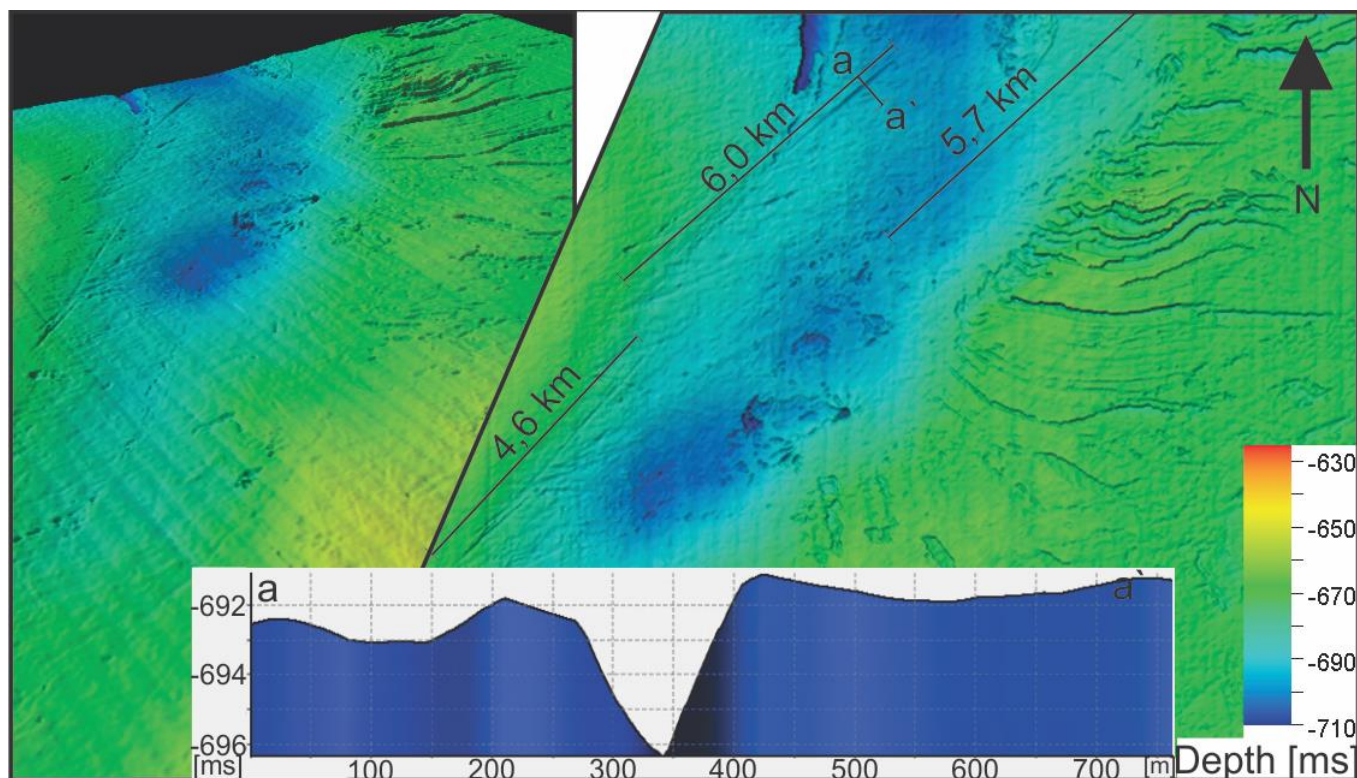


Figure 36 Streamline lineations along the elongated depression.

3.2.6 Streamlined lineations within the Elongated: Interpretation

The streamline lineations on the URU surface have two plausible interpretations. Iceberg ploughmarks and MSGL. The lineations has a V-shaped form and levees on each side which is characteristic for iceberg ploughmarks (Figure 36 profile a- a'). However, iceberg ploughmarks are usually not as straight and unidirectional. If they are iceberg ploughmarks, it would also be expected to find more of them and in the shallower areas as well as the deeper areas: a pattern which is not observed. MSGL are erosive subglacially-formed landform which reflects palaeo-ice flow. Groups of these highly streamlined bedforms have a very consistent orientation. All the streamlined features observed on the URU are oriented in the same north-east south-west direction. Earlier studies from Bjørnøyrenna has described similar oriented MSGL (Andreassen & Winsborrow, 2009) (Piasecka et al., 2016). Their description also fits with the width and length of the lineations in question. However, MSGL are usually located close together and often occupying larger areas of a surface. In this case, only three individual landforms are observed and they are situated several hundred meters to kilometers apart. Despite this, MSGL are the favorable interpretation of the streamlined lineations, and we suggest that other features may have formed but been subsequently eroded or covered in sediment.

3.2.7 Circular basin within the elongated depression: Description

At the base of the elongated depression is a circular negative relief feature. Only one of these features has been observed in the dataset. Its length is 1400 m and width is 1600 m (Figure 37). It is located in the deepest area of the elongated depression in the north western part of the dataset. The topography is uneven, but the deepest part of the basin feature is measured to have 20 ms negative relief in relation to the URU surface. In a seismic profile (Figure 37 profile a – a`), the feature has a steep backwall in the northern end, and is basin shaped in the central parts (Figure 37). Within the basin, there is a high negative amplitude located just above the URU surface (Figure 37 profile a – a`). From a RMS amplitude map extracted 20 ms above and below the URU surface, the anomaly can be seen in the middle of the structure on the URU surface (Figure 37). In the southern end of the seismic section (Figure 37 profile a-a`) the reflector is disturbed and appear as ridges on the surface (Figure 37). The backwall of the basin is south facing, while the basin is more south west oriented.

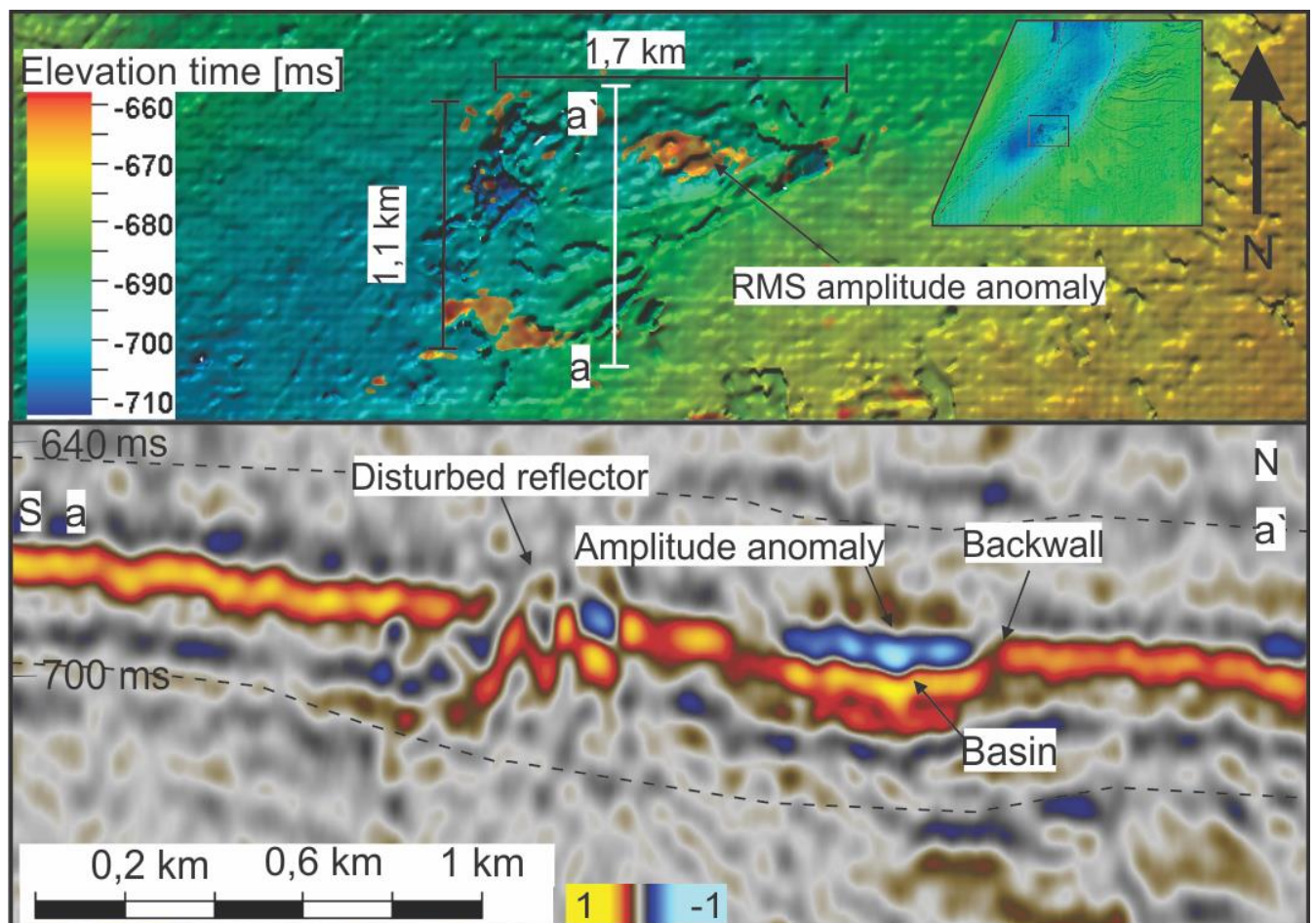


Figure 37 Circular basin on the URU surface. Dotted lines represent 20 ms above and below the URU surface where RMS amplitudes were extracted from.

3.2.8 Circular basin within elongated depression: interpretation

The circular basin located at the floor of the elongated depression is interpreted to be a hill-hole pair. There are several elements from the seismic section that are common with this type of landform. The backwall and the basin together form the lake basin or the hole (Figure 37 and 38), whilst the positive relief ridges located south of the basin (Figure 37 profile a – a`) have the “hills”. These ridges appear similar to glacitectonic ice thrust hills shown in Figure 38 (Evans & Wilson, 2006). These landforms reflect palaeo ice-flow direction. Based on the orientation of the back wall and the ice-thrust hills, the ice-flow direction was approximately north-south. Interestingly, this does not match the orientation of the elongated depression and the streamlined lineations in this area. Compared to MSGs the hill-hole pair is a lot shorter and therefore local subglacial stress unrelated to the large-scale ice-flow direction could form this landform and thus be oriented differently than the ice-flow direction.

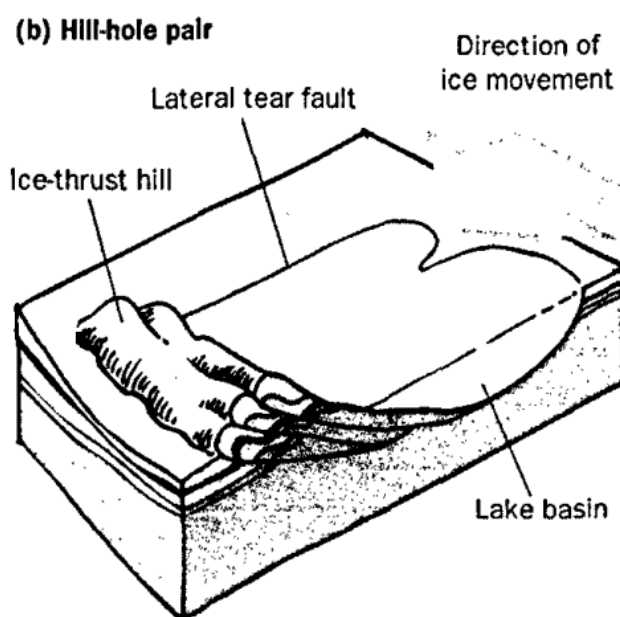


Figure 38 Hill hole pair cartoon, for comparison with the circular basin on URU. Figure from (Evans & Wilson, 2006)

3.2.9 Circular depressions on the URU surface: Description

Five circular depressions are observed on the URU surface (Figure 39). These range in width from ~2 - ~4 km and in depth from 9 – 31 ms. The diameter of all the landforms are measured

from east to west and north to south and listed in Table 2. Of the three horizons interpreted in this study, these features has only been identified on the URU surface.

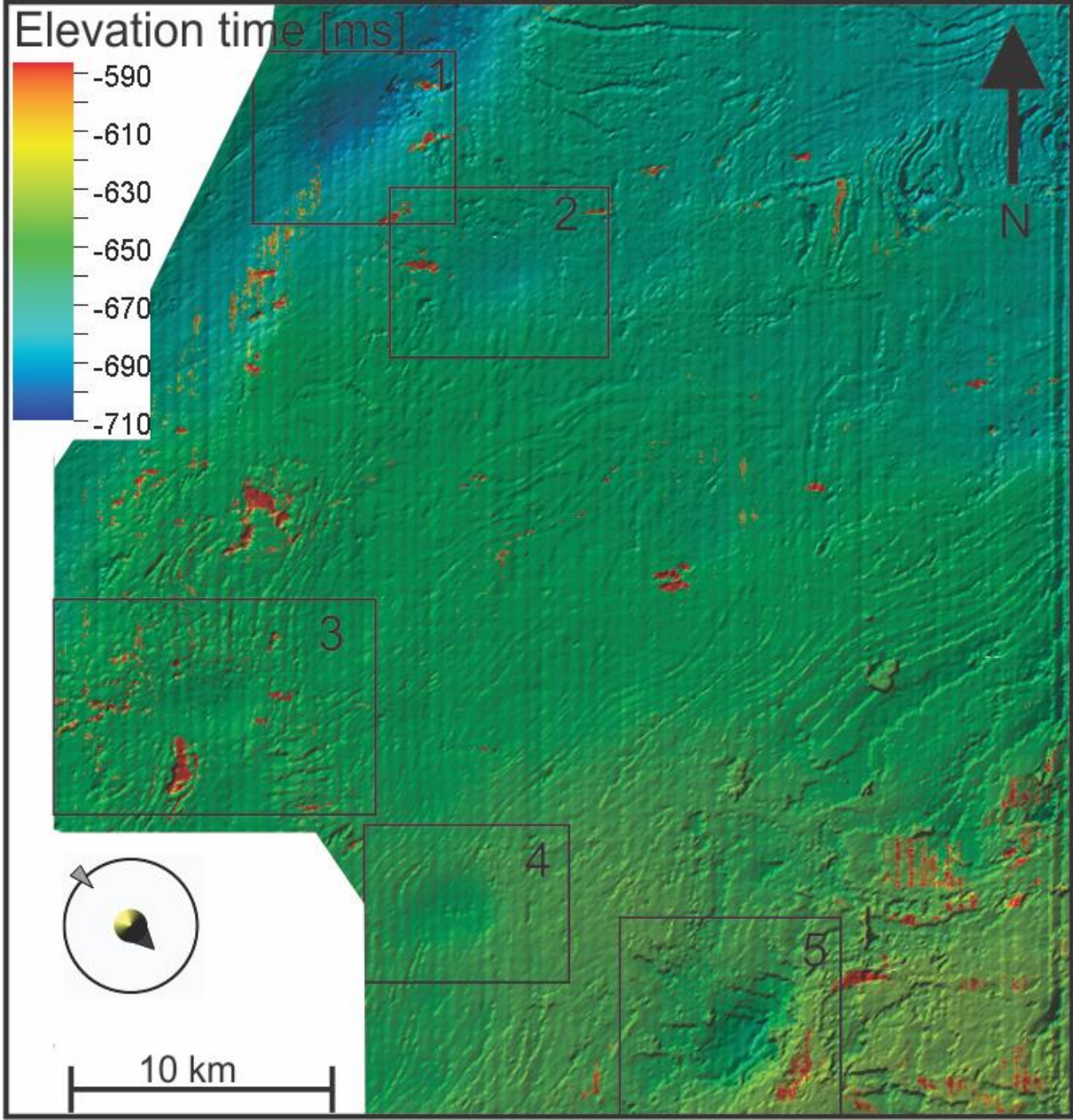


Figure 39 Circular depressions on the URU surface. RMS amplitude anomalies extracted 20 ms above and below the URU surface are added to the map (yellow-red areas).

Table 2 Diameters and relief of circular depressions

Depression	Width (E-W) [m]	Length (N-S) [m]	Relief [ms]
1	3971	2577	25
2	2803	1520	9
3	3801	2491	16
4	2326	1790	8
5	2473	2929	31

Circular depression 3 is measured to be 3801 m in the east-west direction, 2491 m in the north-south direction and has a negative relief of 16 ms. On the rim of the depression there are curved ridges, which all terminates towards the center of the depression. The curved ridges are similar to the once described in section 3.2.1. Along the rim of the depression there are several high RMS amplitudes where the largest one is located in the southern end of the depression (Figure 40). This amplitude anomaly can also be seen in the seismic profile, referred to as a bright spot (Figure 40, profile a-a'). From the same seismic profile (Figure 40 a-a') acoustic masking is seen in the northern end of the depression, below a negative amplitude anomaly. The acoustic masking can be traced from the depression and down to 700 ms. The underlying reflectors below the depression have two different characteristics. From profile a-a' (Figure 40), the underlying reflector is parallel with the shape of the depression, however in profile b-b' (Figure 40) however, the underlying reflectors are truncated by the depression.

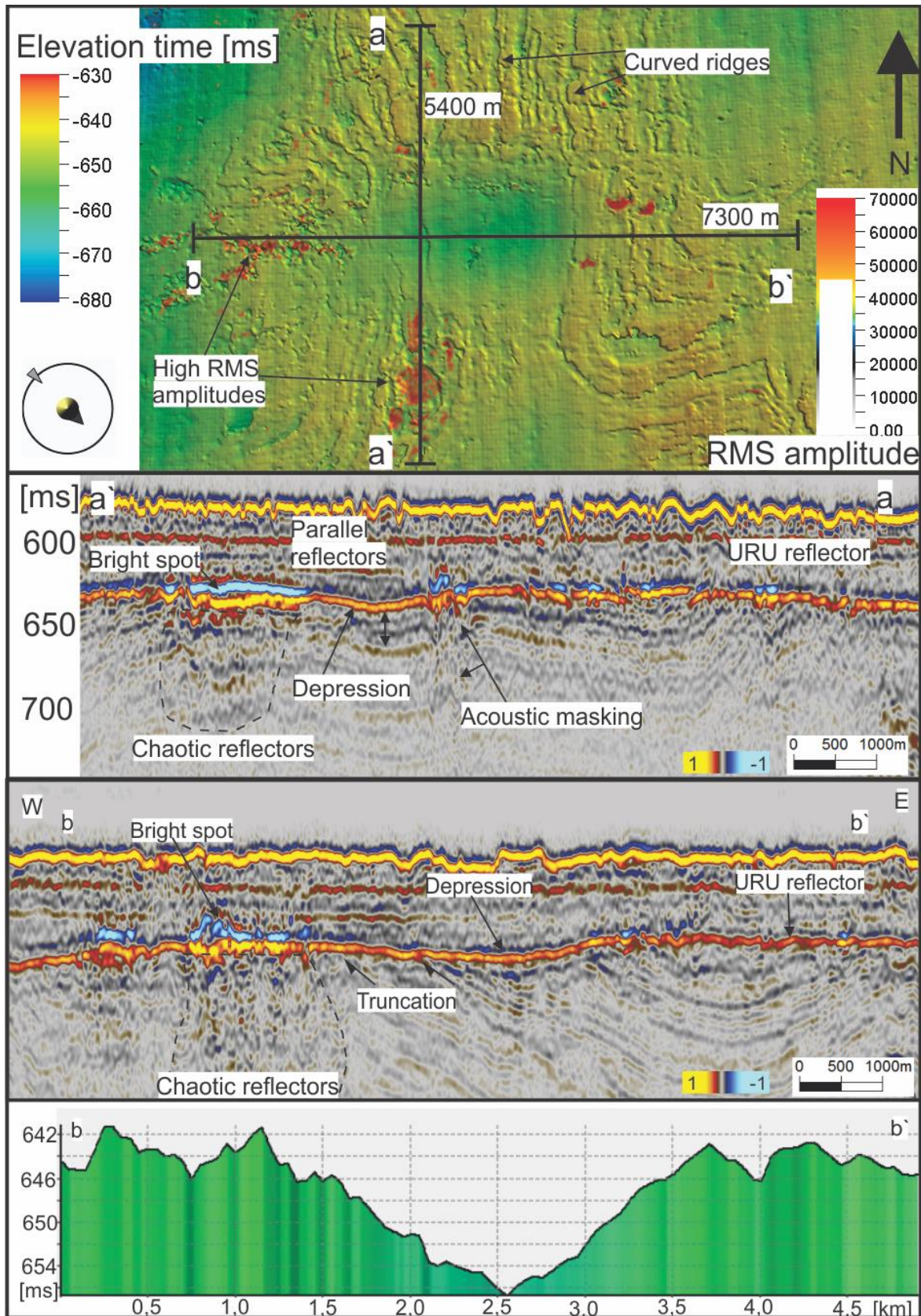


Figure 40 circular depression 3

Located in the southern part of the dataset, circular depression 5 is the deepest of the five identified (Figure 39 and 41). It is situated in an area where the URU horizon is less continuous and harder to trace compared to the northern areas. The depression is measured to be 2,4 km in east-west direction, 2,9 km in north-south direction and with a relief of 31 ms. Similar to depression 3, high amplitude anomalies are found along the rim of the depression 5 (Figure 41). The largest of the bright spots is located on the southern flank of the depression and in a seismic section it can be seen as a negative amplitude bright spot located just above the URU reflector (Figure 41 profile a-a`). Another bright spot is observed on the eastern flank of the depression (Figure 41 profile b-b`). Underlying reflectors are truncated by the depression in all directions (Figure 41 profile a-a` and b-b`). This is unique for circular depression 5, as the other depressions follow underlying strata in one or several directions.

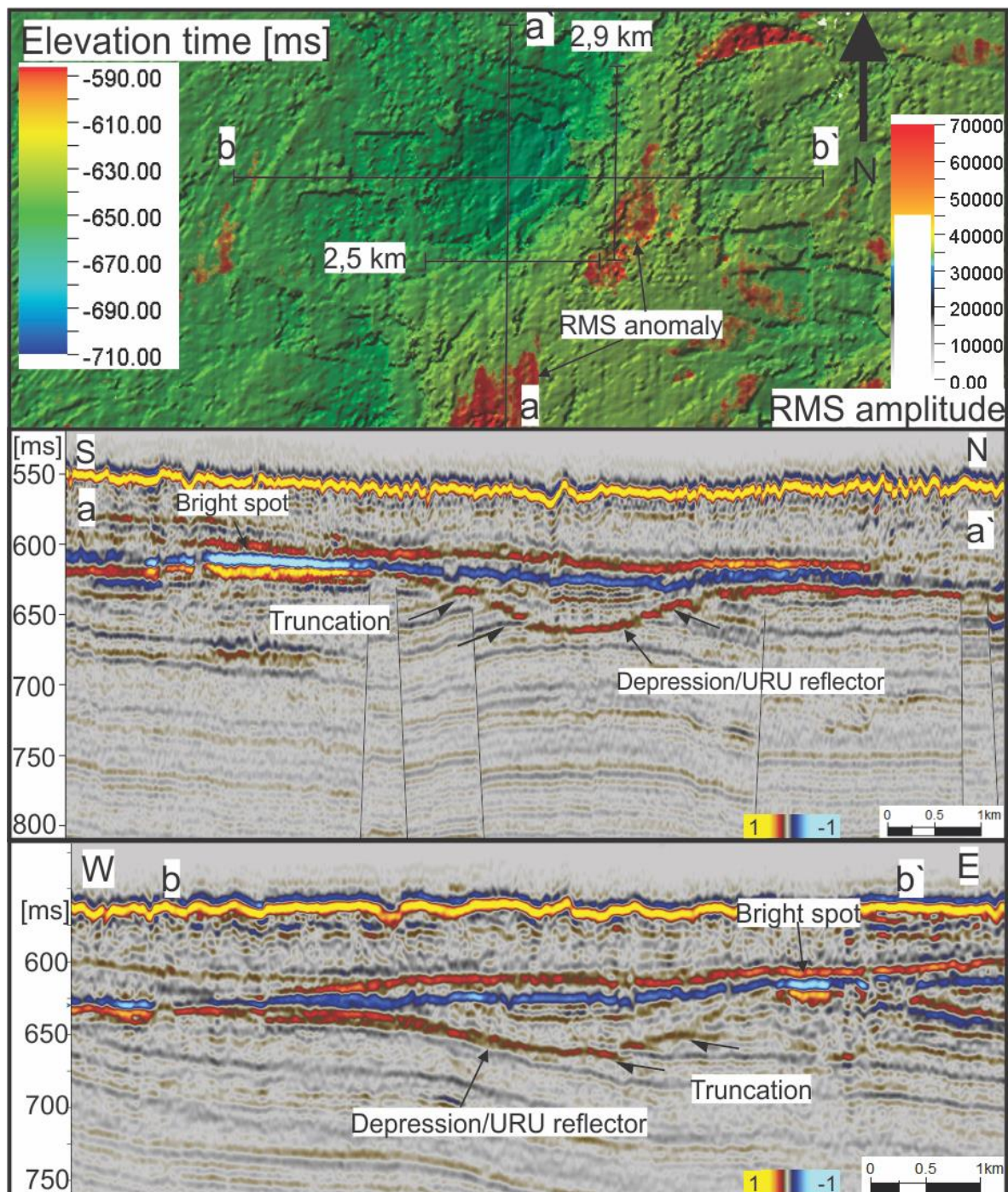


Figure 41 Circular depression 5

3.2.10 Circular depressions on URU: interpretation

The circular depressions on URU are difficult to interpret. I here propose three possible formation mechanisms.

1. Circular depressions due to density differences: The circular depressions are observed on URU, the base of the Quaternary glacial sediment package. Under URU is consolidated Tertiary sedimentary rock. The circular depressions could therefore be related to Tertiary sedimentation processes. Density differences between two layers can result in sinkage and thus form depression features as a post depositional process (Cosgrove & Hillier, 1999). In the seismic profile a-a` (Figure 40), the reflectors under the depression are parallel, consistent with sinkage as a post depositional process.
2. Subglacial pressure points: The subglacial pressure on the bed of an ice stream can vary. For example large sub glacial megablocks can increase subglacial pressure on the bed and could deform pre-Quaternary strata. This would also result in parallel reflectors under the depression as we see in profile a-a` (Figure 40). This process would also displace underlying material, which would form the rim around the depressions.
3. Subglacial lakes: Subglacial meltwater can form channels and lakes under ice sheets and ice streams. The circular depressions could be subglacial lakes. From profile a-a` and b-b` (Figure 41) there are internal reflectors within circular depression 5, which indicate subglacial lacustrine sediments. Similar features have been identified further west in the Barents Sea (Esteves et al., 2017).

3.3 RMS amplitude anomalies along URU surface (bright spots)

RMS amplitudes has been extracted 20 ms above and below the URU surface. This approach highlights anomalously high (or low) amplitudes and thus indicate possible gas or fluid accumulations. These anomalies are referred to as bright spots and are found several places along the URU surface. In the north, several of them are found in relation to the bedrock ridges (section 3.2.1). High amplitudes are also found within and along the flanks of the elongated depression (section 3.2.3). In the central parts of the dataset, bright spots are found along the flanks of the circular depressions (section 3.2.9). In the southern parts of the URU surface, the stratigraphy is heavily affected by faults. Large bright spots are also observed here.

3.3.1 Bright spots along bedrock ridges: description

Curved ridges are interpreted as bedrock ridges from folded Pre-Quaternary strata which are truncated by the URU reflector (section 3.2.1 and 3.2.2). Along the ridges, several bright spots are observed on the RMS amplitude map (Figure 42). They are often positive amplitude bright spots located in the truncation point of the URU and the underlying reflector (Figure 42). Negative amplitude bright spots are also abundant in relation to the bedrock ridges. However, these high amplitudes are not connected to a truncation point from any of the underlying reflectors. From Figure 42, the negative amplitude bright spot is located just above the URU surface and the underlying reflectors are discontinuous and chaotic (Figure 42 profile b-b'). The reflectors are also shifted down under the bright spot (pull-down effect) (Figure 42 b-b').

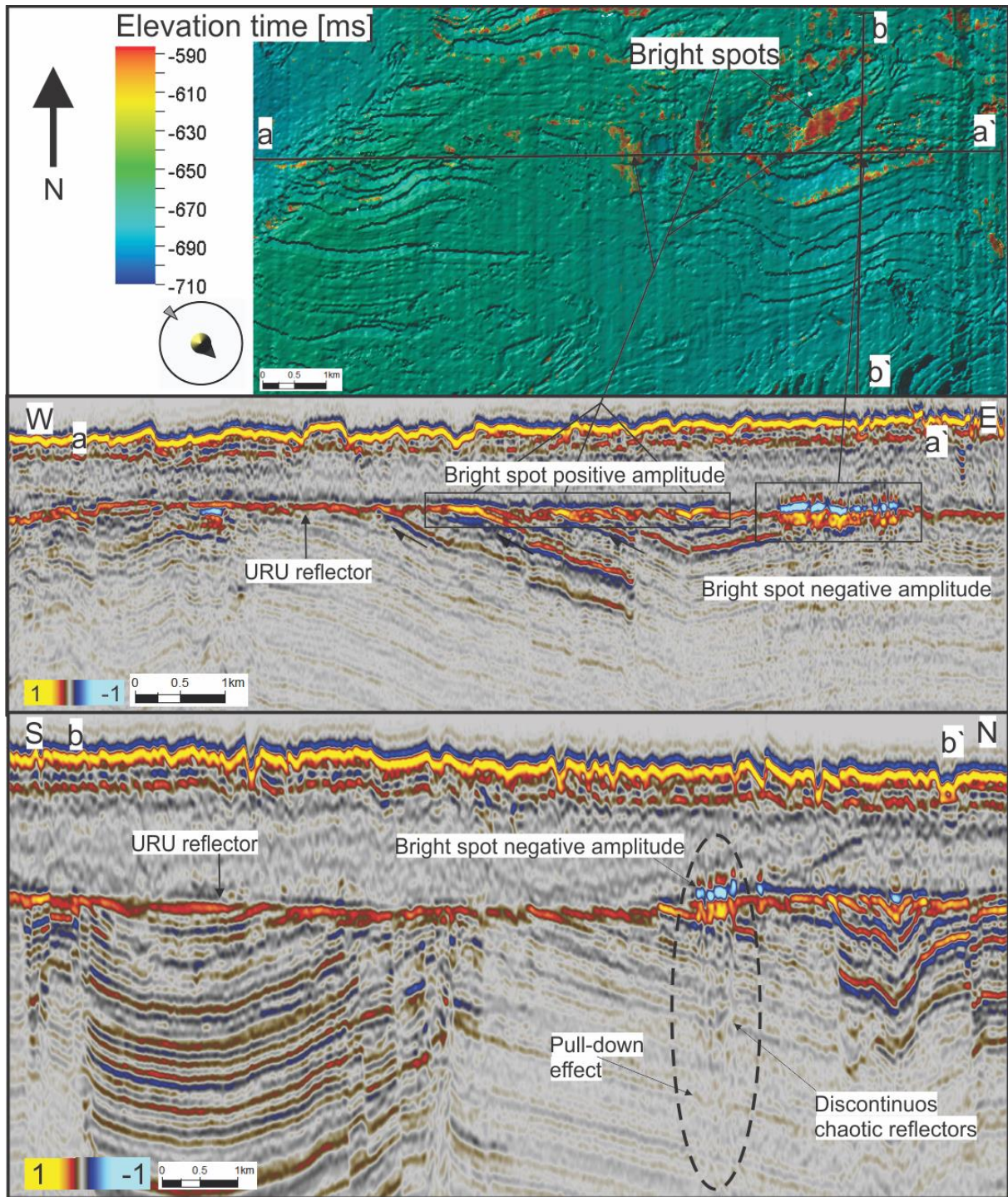


Figure 42 Bright spots associated with the curved ridges on URU

3.3.2 Bright spots along the bedrock ridges: Interpretation

Bright spots are found along several of the bedrock ridges in the north of the dataset. They are often related to underlying reflectors truncating the URU surface and have a positive amplitude. These bright spots are formed by constructive interference between the underlying

reflectors and the URU reflector. This gives the reflector an amplified expression at the truncation point (Figure 42 bright spots positive amplitude).

Negative amplitude bright spots are found in the same areas. However their shape and abundance are different from the positive ones. Negative amplitude bright spots are much less common than the positive ones along the bedrock ridges. They also appear as flat reflectors (Figure 42 bright spot negative amplitude). Figure 42, profile b-b` also shows that the seismic stratigraphy under the negative amplitude bright spots are affected. Discontinuous and chaotic reflectors as well as pull down effect are indicators of gas and the negative amplitude bright spot are therefore interpreted as shallow gas deposits.

3.3.3 Bright spots related to elongated depression: description

Bright spots are observed within and along the flanks of the elongated depression located in the north west of the dataset (Figure 43). In this area, all the bright spots has a negative amplitude and are located just above the URU reflector, similar to the negative amplitude bright spots associated with the curved ridges (section 3.3.1 and 3.3.2). Three of these bright spots will further be described.

Within the center of the circular basin there is a 0,4 * 0,2 km large bright spot (circular basin section 3.2.7). It is located on top of the BFC and between the LH and BB (Figure 44). Under the bright spot, the reflectors are semi-parallel but discontinuous (Figure 44). At the terminations of the bright spots there are two faults (Figure 44).

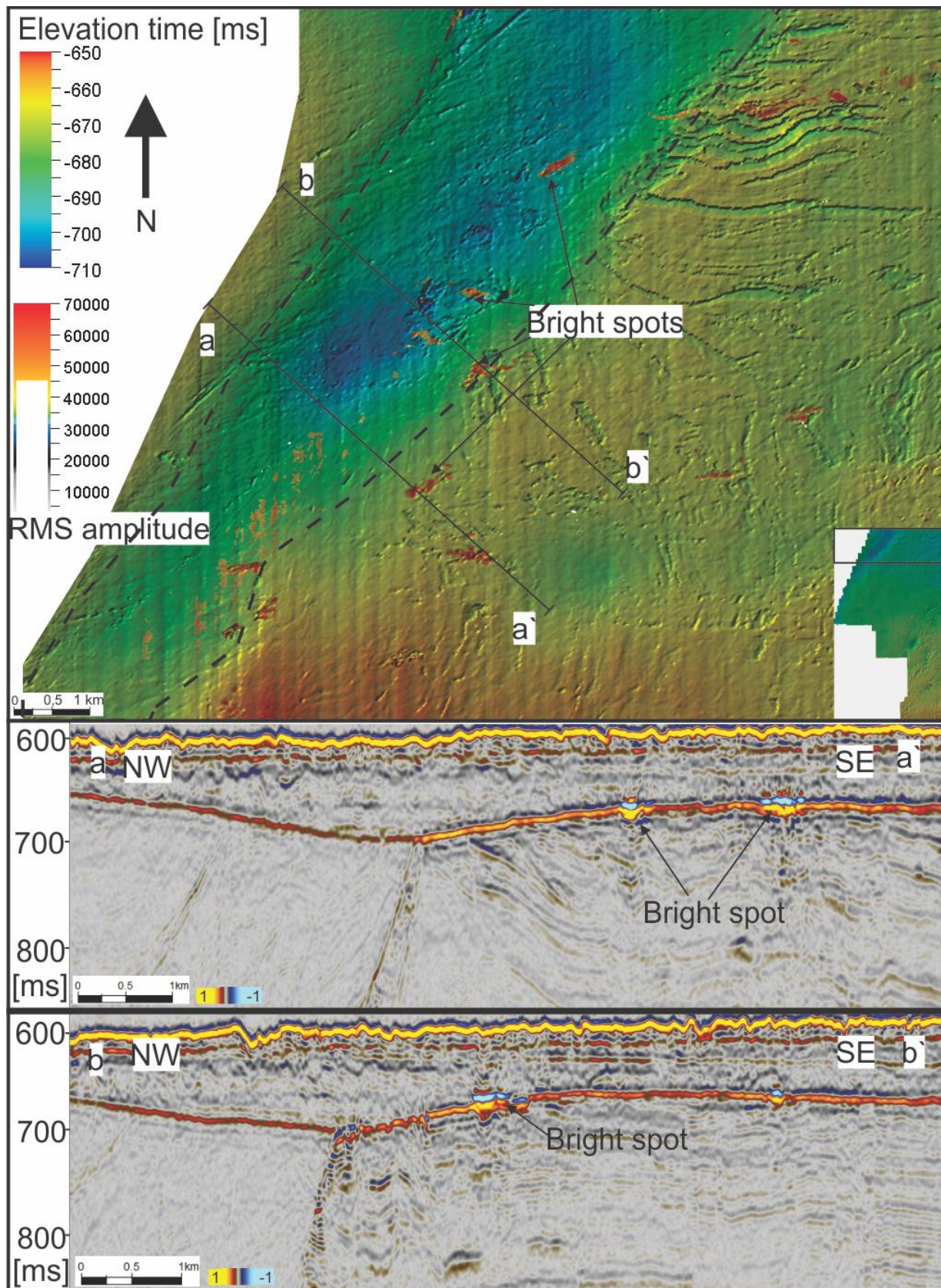


Figure 43 Overview of bright spots along the elongated depression on URU. The dotted line marks the outline of the elongated depression

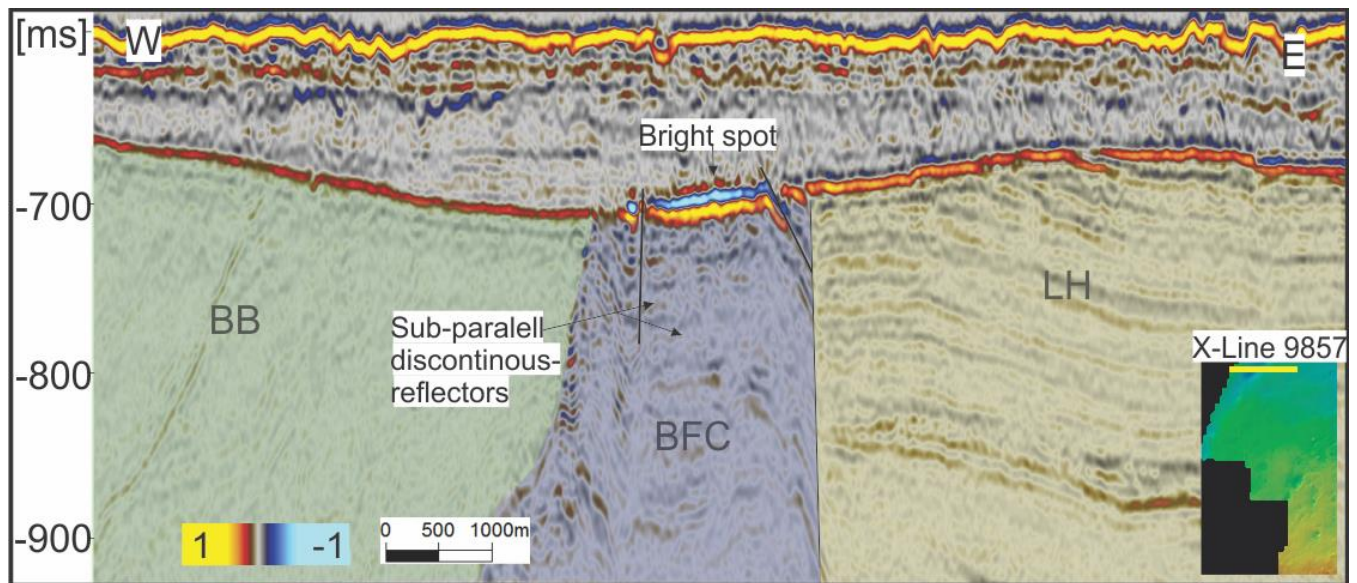


Figure 44 Bright spot at the base of the elongated depression. BB Bjørnøya Basin, BFC Bjørnøyrenna fault complex, LH Loppa High

Further south, two bright spots of negative amplitude are located on the eastern flank of the elongated depression (Figure 43). From a composite line crossing the elongated depression, they are situated on the hinge of the flank. Reflectors from east are leading towards this bright spot (Figure 43).

3.3.4 Bright spots elongated depression: interpretation

All the bright spots associated with the elongated depression have been interpreted as shallow gas deposits migrated from deeper hydrocarbon reservoirs. The strong negative amplitude together with acoustic masking below the bright spots are indicators for hydrocarbon fluids. The location of the bright spots also argues for hydrocarbon deposits. Hydrocarbons will always migrate upwards due to density differences, and in this case all the bright spots are observed in structural highs. Within the circular basin, the bright spot is located on top of the BFC where two faults prevent horizontal migration. On the eastern flank of the elongated depression, the bright spots are all located on the berm of the flank. The berm forms an antiform structure and is therefore a plausible hydrocarbon trap (Figure 43). The pre Quaternary strata on the eastern flank lead up towards URU, and its therefore plausible that permeable interbeds works/have been working as migration pathways for fluids.

3.3.5 Bright spots related to circular depressions: description

Associated with circular depression 1, 2, 3 and 5 are negative amplitude bright spots. Most of these are observed on the rim of the circular depressions (Figure 39). From circular depression 3 (Figure 40 profile a-a`), a large lateral change in amplitude occur from the center of the depression and towards the north and south. Below the negative amplitude bright spot, the reflectors are affected by acoustic masking. The largest bright spot is located just south of circular depression 3. It expands 1800 m in north-south direction and 584 m in east-west direction.

3.3.6 Bright spots related to circular depressions: interpretation

The negative bright spots near the circular depressions are interpreted as shallow gas deposits which have migrated from deeper hydrocarbon reservoirs. This is based on the high negative amplitude reflectors which are characteristic for such deposits. They are also located on the rim of the depressions, which are local structural highs suitable for accumulating fluids. These shallow gas accumulations are not interpreted to be connected to the formation of the depressions but accumulated post formation.

3.4 Intra Quaternary Horizon

The intra Quaternary horizon is a relatively strong positive reflector, stratigraphically situated between the seabed and the URU reflector. It can be traced across much of the dataset, although compared to the seabed and the URU reflector, the intra Quaternary horizon is the weakest reflector and the least continuous. The intra Quaternary horizon follows the same trend as the seabed and the URU surface regarding depth measured in time. The deepest areas are found in the north-west of the dataset (628 ms TWT) and the shallowest areas in the south (530 ms TWT) (Figure 45). In the northern parts, there are curved lineations with similar orientation to the large curved lineation sets 1 and 2 found on the seabed (Figure 29 a)). In the central parts of the intra Quaternary horizon, there are streamlined lineations oriented in a north-east south-west direction (Figure 45 b)). They are located next to an area where the horizon was difficult to interpret and are therefore not interpreted further. In the south, there is a streamlined line of depressions which has a similar north-east south-west direction to the streamlined lineations, just more south facing (Figure 45 c)).

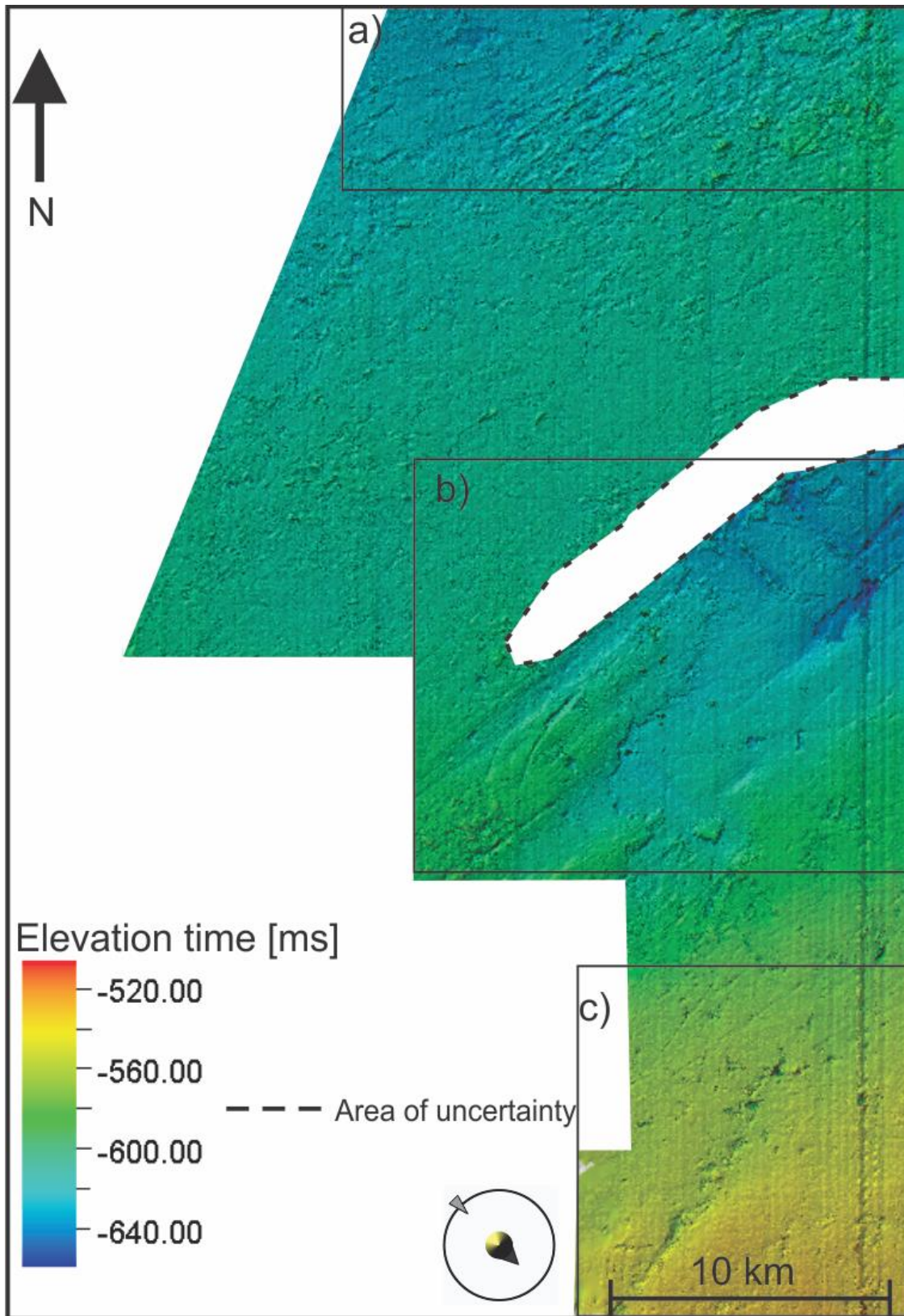


Figure 45 Intra Quaternary horizon surface. Area a) contain curved lineations, b) streamlined lineations and c) line of depressions

3.4.1 Curved lineations on the intra Quaternary horizon: description

Curved lineations are found on the intra Quaternary horizon surface. In general, they have a north-east to south-west orientation with some exceptions. The shortest measured feature is 1300 m and the longest is 1490 m. In width they are typically a few hundred meters, but the largest measured is 600 m. These curved lineations are most abundant in the deepest northern parts. However, some can be seen in the central and the southern parts of the dataset to.

The curved lineations on the intra horizon can be matched with those observed on the seabed surface (Figure 29). These are the large lineation set 1 and 2, which are found in the deepest parts of the dataset on the seabed surface. The same overprinting of the two sets can be seen on the intra-Quaternary surface (Figure 46). The first set of lineations has an orientation of 50 degrees and the second set 62 degrees north-east. Compared to the curved lineations on the seabed surface, these have similar orientation and shape.

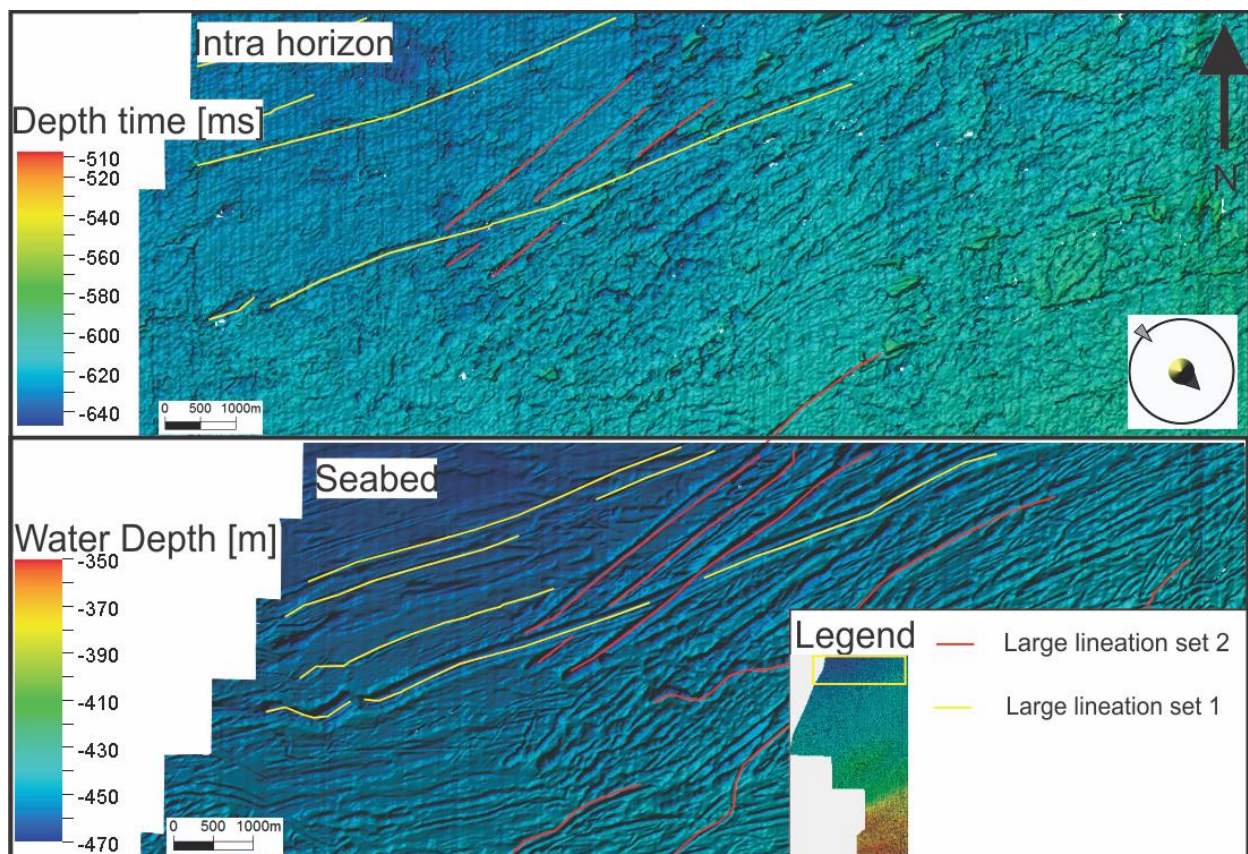


Figure 46 Curved lineations on the intra Quaternary horizon and the seabed. Large lineation set 1 and 2 can be seen on both surfaces

3.4.2 Curved lineations on the intra Quaternary horizon: interpretation

The curved lineations on the intra Quaternary horizon are interpreted to be large iceberg ploughmarks penetrating the sediments from the seabed down to the intra horizon. This is based on the identical shape and orientation of the ploughmarks found on the seabed. Since the same ploughmarks found on the intra Quaternary horizon also are visible on the seabed surface it is suggested that they formed by icebergs ploughing the seafloor surface, but which has deep enough keels to also scour the underlying sediments, to at least a depth of the intra Quaternary horizon. They are therefore likely to relate to the final deglaciation in this area. Figure 47 shows how ploughmarks from the seabed surface have affected the intra-Quaternary surface.

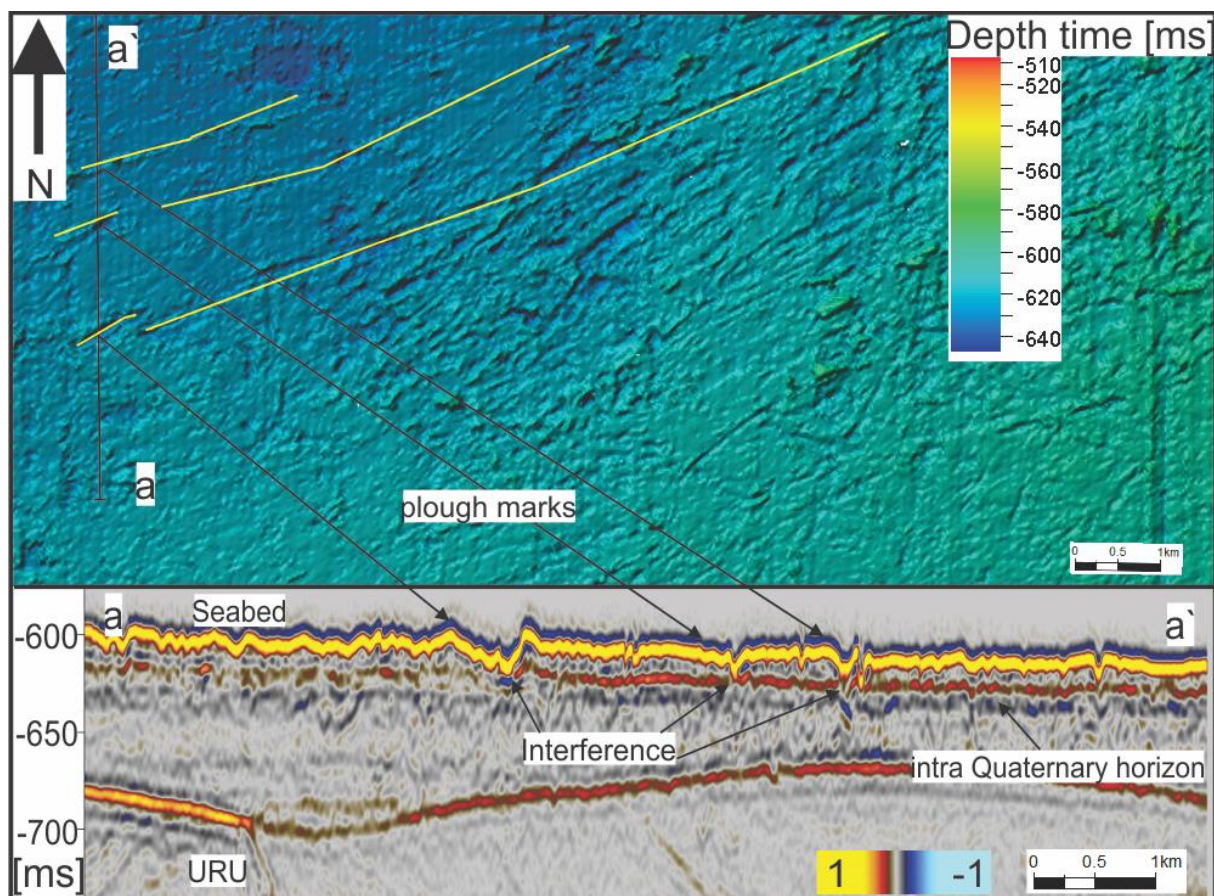


Figure 47 Profile a – a` across curved lineations on the Intra Quaternary surface show how the scour marks on the seabed horizon penetrate the seafloor sediments to such a depth that they also scour the intra Quaternary horizon

3.4.3 Streamlined lineations on the intra Quaternary horizon: description

In the central parts of the intra Quaternary horizon, there are streamlined lineations with north-east to south-west orientation (Figure 48). Unlike the curved lineations described above,

these are unidirectional and parallel to each other. In the north-east end of the features, the horizon is too discontinuous and chaotic to interpret and in the south-west end, they terminate outside of the dataset. The lateral expansion of these features are not possible to determine. However, from what is possible to see on the surface, the lineations vary from 4,8 to 6 km (Figure 48). The width of the lineations are measured from 100 to 250 meters and they have a negative relief of 2 ms. A profile perpendicular crossing the streamlined lineations, reveals that the intra-Quaternary horizon is undulating where the measured amplitude is 10 ms (Figure 48).

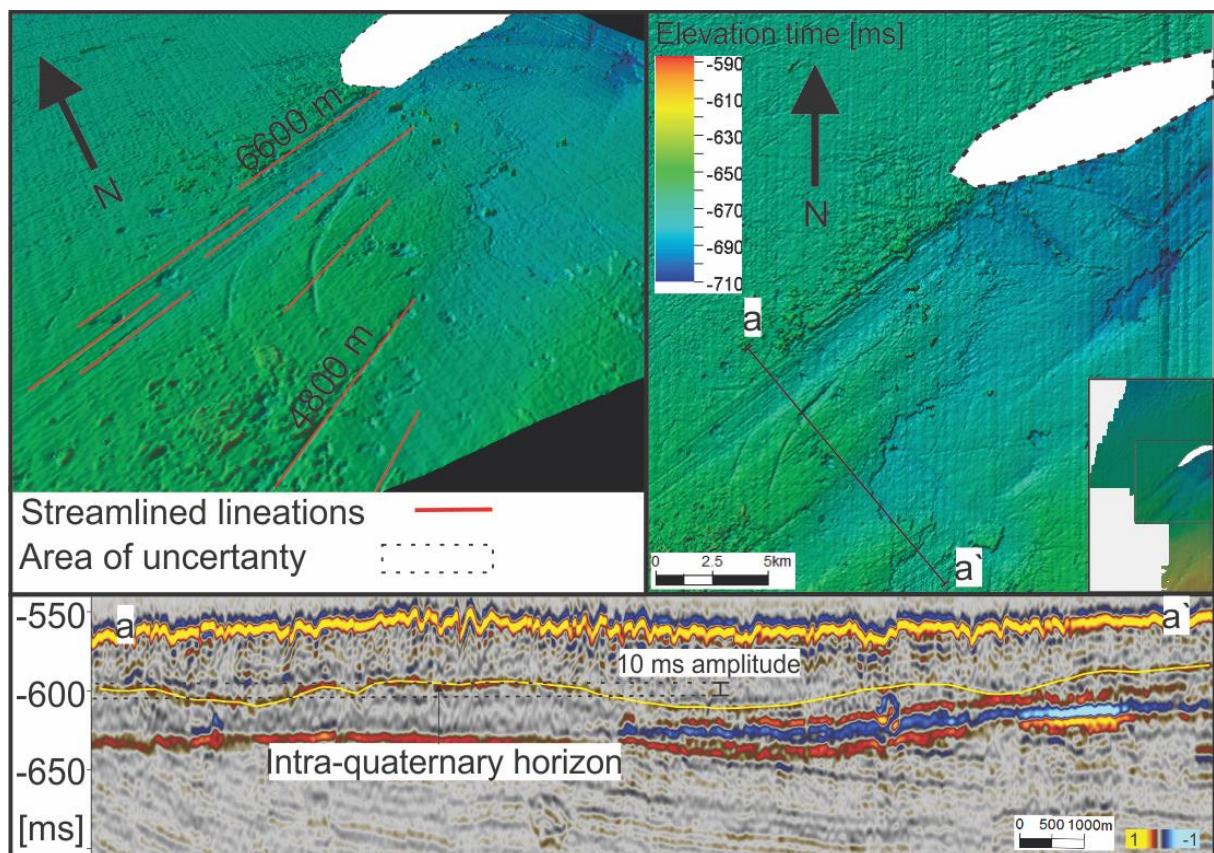


Figure 48 streamlined lineations on the intra-Quaternary horizon

3.4.4 Streamlined lineation on the intra-Quaternary horizon: interpretation

Streamlined lineations on the intra-Quaternary horizon are interpreted to be mega scale glacial lineations. Typical for MSGL are highly elongate parallel negative relief features. These are also several kilometers long and have the same orientation as the other MSGL sets observed about 120 km south from our study area (Andreassen & Winsborrow, 2009). These features will further be compared and discussed in the discussion chapter.

3.4.5 Line of depressions: description

In the southern part of the intra-Quaternary horizon, there is a linear feature consisting of several depressions. The length of this feature is 13,2 km, and it appears as if the feature extends beyond the dataset (Figure 49). The orientation of the feature is south-west to north-east, similar to the streamlined lineations (section 3.3.4), however the line of depressions is slightly more south oriented compared to the streamlined lineations. It consists of several individual and connected depressions those relief are measured to ~16 ms. In width the internal depression of individual features is measured to be 200 – 800 m. A variance time slice map from -670 ms shows that the area below these features is dominated by west, south-west east north-east striking faults (Figure 49). The same faults are observed in a seismic profile along the line where the faults can be traced down to 769 ms (Figure 49). Three different profiles along and beside the line of depressions indicates a clear difference in continuity of the intra-Quaternary horizon. In profile b-b` (Figure 49), the intra-Quaternary horizon is less continuous and interrupted by areas of acoustic masking. Compared to profile a-a` and c-c` where the intra-Quaternary horizon is more continuous and less interrupted by areas of acoustic masking and depressions (Figure 49). In profile b-b` there are several areas of acoustic masking above the intra-Quaternary horizon. The acoustic masking can in some areas be traced all the way to the seabed. In all three profiles in Figure 49 a negative relatively high amplitude reflection is seen just above URU and below the intra Quaternary horizon (Figure 49).

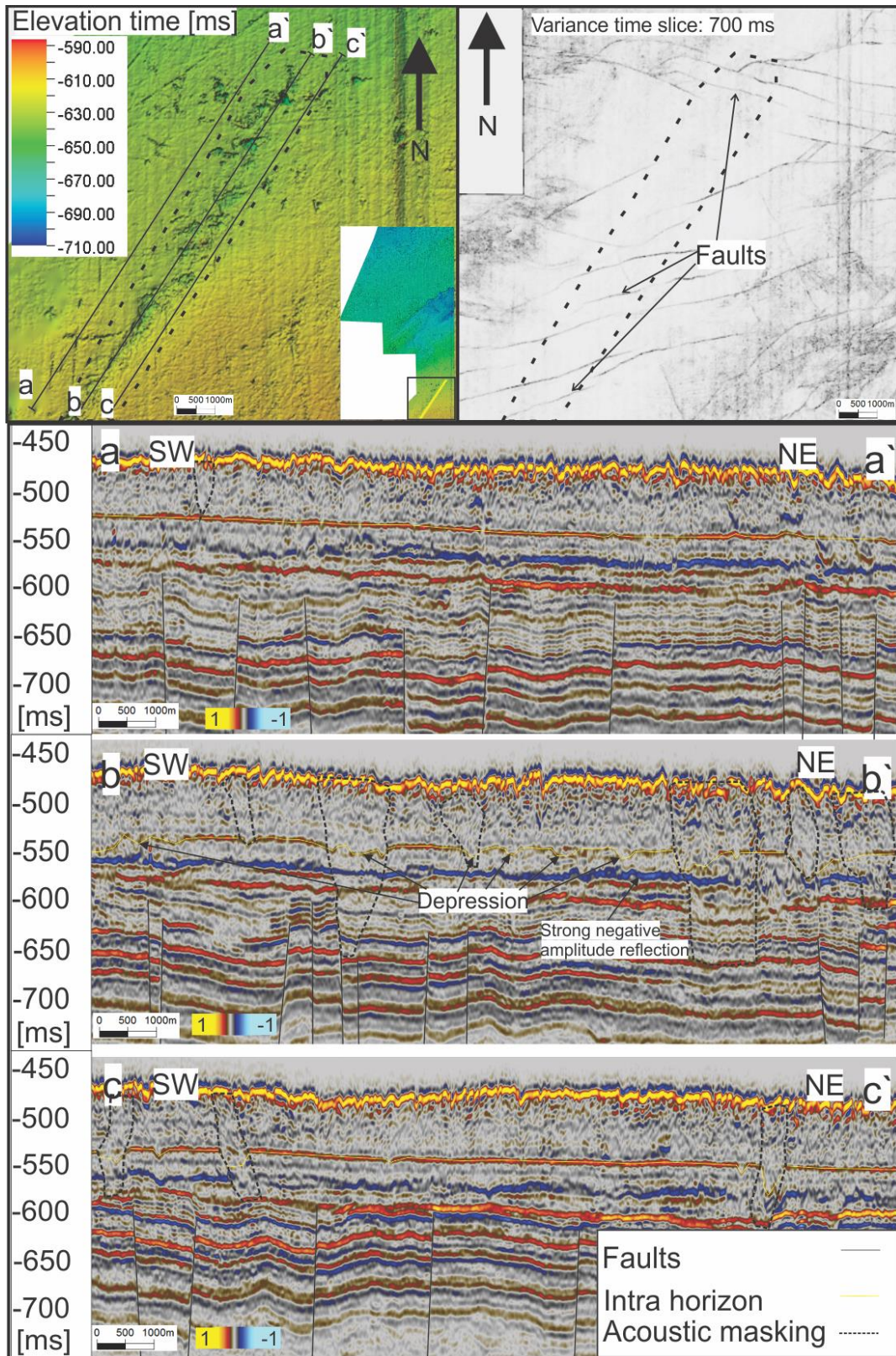


Figure 49 Line of depression on the intra Quaternary surface. Three profiles a-a', b-b' and c-c' are shown next to and along the line of depression to indicate the characteristics of the intra Quaternary horizon at the different areas. A variance time slice from 700 ms reveals faults in the area. The faults can also be seen in the seismic profiles.

3.4.6 Line of depressions: Interpretation

There are two main plausible interpretations for the line of depressions on the intra Quaternary horizon. The line of depressions is observed in an area where the pre-Quaternary bedrock is heavily faulted and there is a high abundance of acoustic masking. Two interpretations of the line of depressions are suggested: (i) Blow-out craters due to melting of gas hydrates or (ii) glaciectonic processes. Both theories include till stiffening due to the abundance of gas hydrates during the late Weichselian glaciation. This will further be discussed in the discussion chapter.

3.5 RMS amplitude anomalies along the intra horizon surface

An RMS amplitude map has been extracted along the intra Quaternary horizon, 20 ms above and below in the same way as with the URU surface. The results show that there are high amplitudes several places along the surface. In the north, they are found in relation to the curved lineations. In the central parts, there are four major bright spots aligned in a north-east south-west orientation near the area where the MSGL are located. In the southern parts where the line of depressions is located there are no bright spots located on the intra Quaternary horizon.

3.5.1 Bright spots related to iceberg ploughmarks: Description

In the northern parts of the study area there are several bright spots, most of which follow the morphology of the iceberg ploughmarks. These bright spots have an unusually high amplitude compared to the ones situated further south on the surface. A profile crossing a bright spot located within an iceberg ploughmark, reveals that the seabed reflector interferes with the intra horizon in these cases (Figure 50).

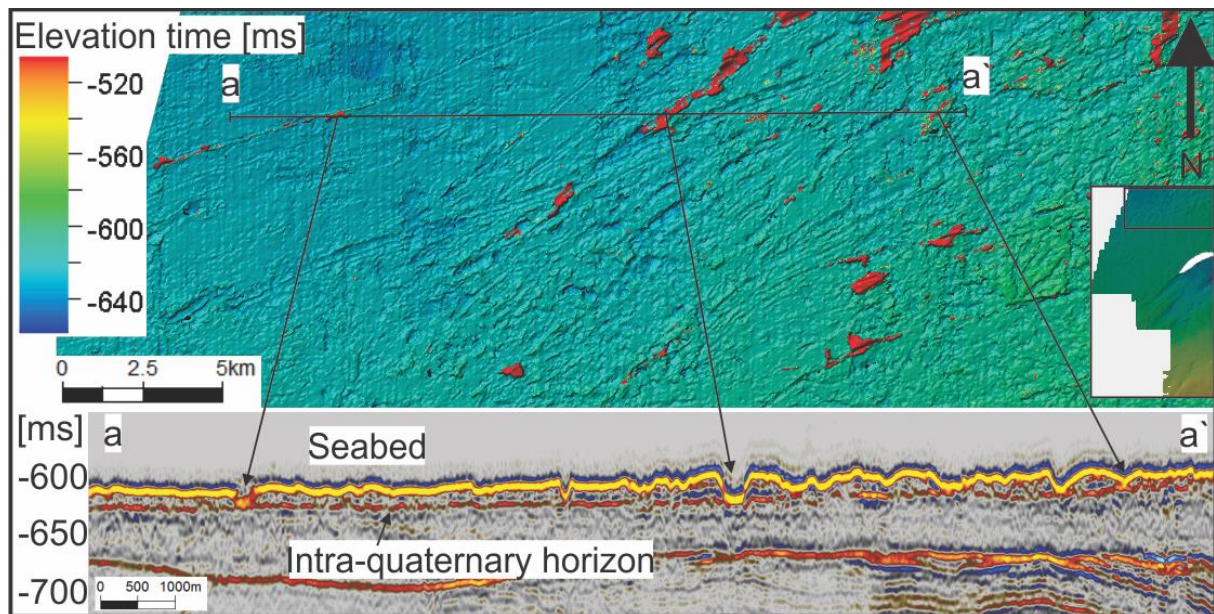


Figure 50 bright spots on intra horizon in the northern parts of the dataset. Arrows points to where the seabed reflector interferes with the intra horizon. Red areas are RMS amplitude anomalies

3.5.2 Bright spots related to iceberg ploughmarks: Interpretation

The bright spots related to iceberg ploughmarks have been interpreted to be interference from the seabed reflector causing high RMS amplitude in these areas.

3.5.3 Bright spots in central parts

In the central parts of the dataset, five relatively large bright spots are located aligned in a north-east to south-west orientation. The orientation is very similar to the orientation of the line of depressions. A profile crossing these bright spots shows that all are negative amplitude bright spots located just below the intra Quaternary horizon. Below the bright spots are faults, which can be traced 1 s (TWT) down in the stratigraphy. Along the faults the reflectors are affected by acoustic masking and pull down effect in certain areas (Figure 51).

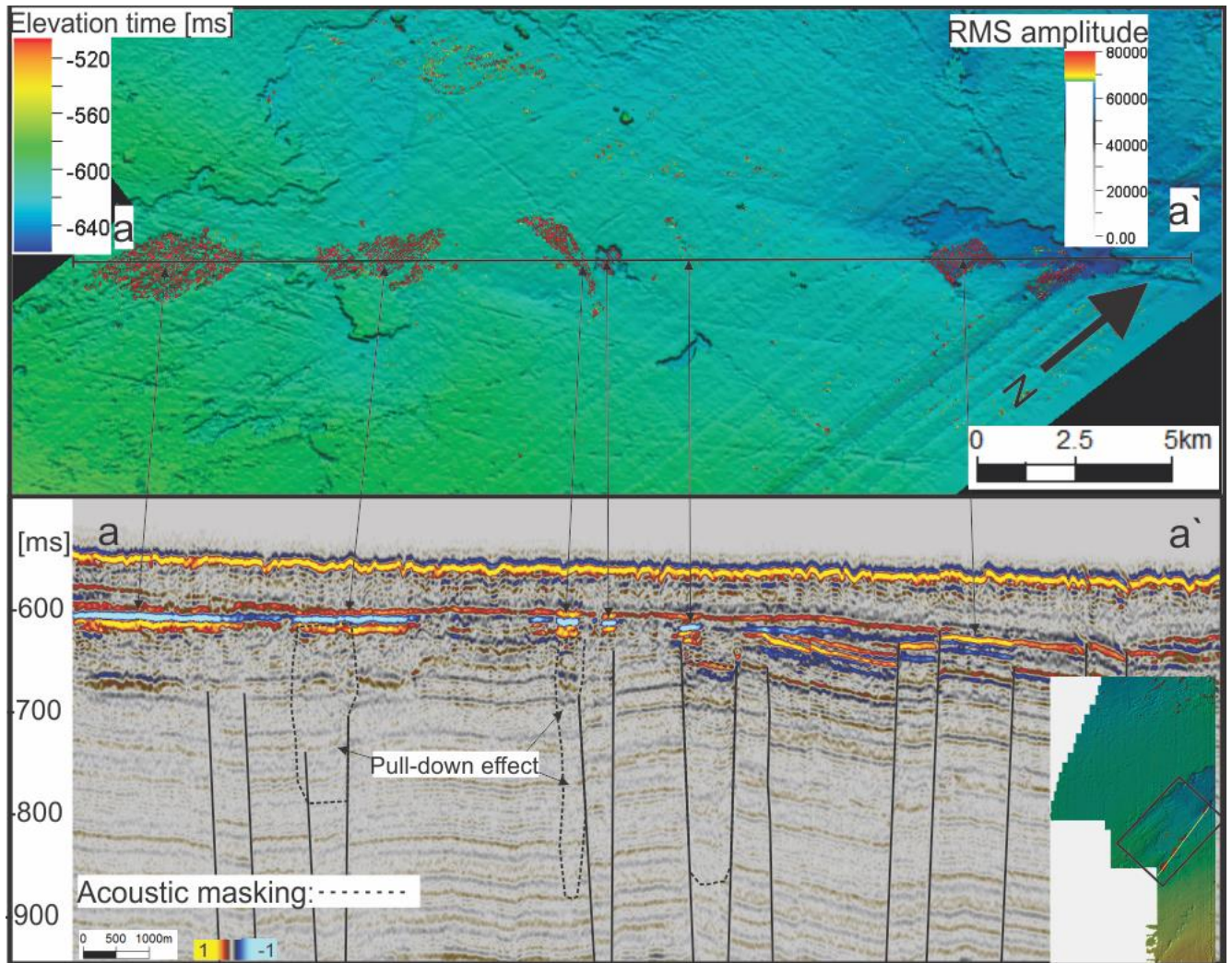


Figure 51 bright spots southern parts of the intra Quaternary horizon. The bright spots on the surface are connected by arrows with the seismic profile.

3.5.4 Bright spots in central parts of the intra Quaternary horizon: Interpretation

The bright spots located in the central parts on the intra Quaternary horizon are interpreted as shallow gas deposits, migrated from deeper hydrocarbon reservoirs. The strong negative amplitudes are typical for gas deposits. All the bright spots have faults leading up to them from deeper stratigraphy. The fact that the reflectors along the faults are affected by acoustic masking is an argument that the faults have worked as migration pathways. Pulldown effect is also seen within the areas of acoustic masking. This indicate slower acoustic velocity, characteristic for gas deposits. It is thus believed that these bright spots on the intra-Quaternary surface are gas deposits which have migrated from deeper hydrocarbon reservoirs.

4 Discussion

The discussion chapter consists of two parts. The first part focuses on the landforms mapped on the URU and the intra Quaternary horizon, in particular evaluating what they may inform on glacial dynamics, fluid flow and connection to gas hydrates in the area. The second part will focus on linking information gained from this study on former ice flow direction and velocity with existing knowledge of regional glacial and deglacial dynamics and chronology of the Bjørnøyrenna ice stream.

4.1 Observed landforms on URU and Intra-Quaternary horizon

4.1.1 Bedrock ridges on URU

The curved ridges observed on the URU surface are interpreted to be bedrock ridges from pre-Quaternary strata (section 3.2.1 and 3.2.2). We propose that the ridges form due to differences in strength between geological beds, resulting in variable response to glacial erosion. As a result, harder beds, more resistive to glacial erosion sticks up as ridges (Figure 52). Similar features have been observed further north within Bjørnøyrenna, where the ridges originate from early Cretaceous bedrock (Bellwald et al., 2019) (Figure 52).

In our study area the bedrock ridges are observed on URU within the Loppa High area at about 650 m below seafloor. An exploration well (Wellbore 7220/2-1) drilled by Statoil Petroleum about 40 km south of our study area drilled through Kapp Formation at 655 m (NPD, 2014). The Kapp formation consist of a number of coarsening upward successions containing shales, siltstones and sandstones from late Triassic to middle Jurassic (NPD, 2020). We therefore suggest that the bedrock ridges consist of upward coarsening successions where the finer, softer clays and silt beds are eroded deeper than the sand rich part of the

succession, resulting in bedrock ridges on URU. However, well boring is needed for certain knowledge of the composition of the bedrock ridges in this area.

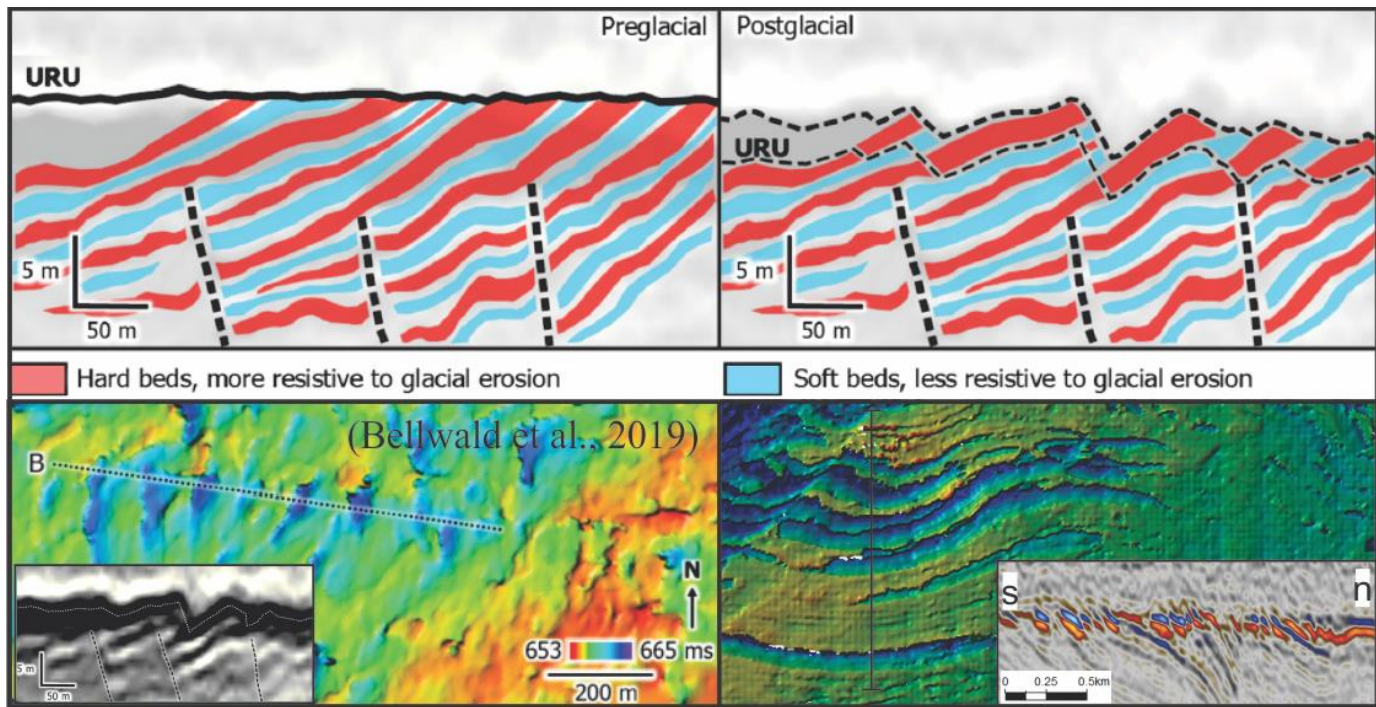


Figure 52 Conceptual model of bedrock ridges and how they form in the top panels Figure from (Bellwald et al., 2019). The lower two panels show a planar view comparison of the ridges observed by Bellwald et al., (2019) (lower left) and bedrock ridges from our study (lower right).

An alternative interpretation of the bedrock ridges could be that they formed post-glacially, as a result of destabilization of gas hydrates. Indications of shallow have has been interpreted in this area (section 3.3.1 and 3.3.2), and these observations are consistent with high abundance of shallow gas and gas hydrates predicted across much of the SW Barents Sea (Vadakkepuliyambatta et al., 2017). Today the gas hydrate stability zone in the Barents Sea region is highly variable, however our study area lies close to where gas hydrates have been observed (Chand et al., 2008). During last glacial maximum and parts of the deglaciation, higher pressures due to ice loading on the shelf and lower temperatures makes it plausible that gas hydrates were stable within our studyarea. During the deglaciation as the ice sheet thinned and retreated, subglacial pressure would decrease and temperature increase, causing destabilization of gas hydrates. Such processes could cause sediments that previously hosted gas hydrates to collapse, forming ridges (Figure 53). This has been suggested to explain the formation of rhombohedral ridges observed on the URU surface in Bjørnøyrenna (Bellwald et al., 2019) (Figure 53). The gas hydrate decomposition ridges identified by Bellwald (2019)

have similar ridge-depression morphology to the bedrock ridges observed in this thesis (Figure 53). However, in our study area the ridges do not have the same rhombohedral shape, and we therefore favor the interpretation that they formed due to differential resistance to glacial erosion.

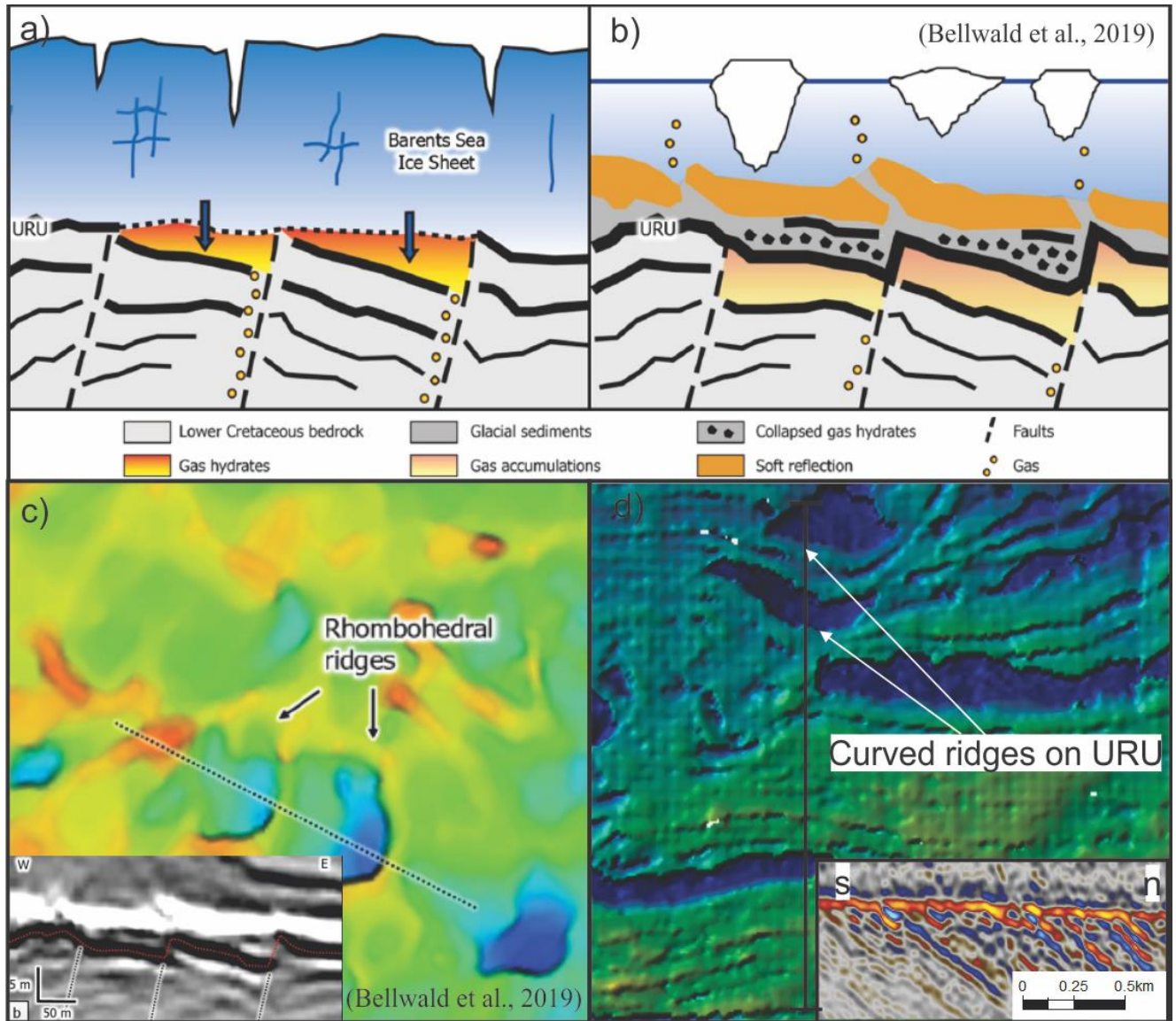


Figure 53 Collapsing of gas hydrates could result in the formation of curved ridges as observed on the URU surface. a) glacial stage were gas hydrates where stable. b) Post glacial period where the gas hydrates collapsed and formed ridge-depression, rhombohedral ridges on URU. c) Observed rhombohedral ridges on URU by Bellwald et al, 2019. d) Observed curved ridges on URU in our study area. Figure modified from Bellwald et al., (2019)

4.1.2 Elongated depression on URU

A prominent elongated depression is observed in the northern parts of the URU. The depression has about 35 ms of negative relief and is measured to be over 28 km long. Within

the elongated depression there are observed MSGL, a landform indicative of fast flowing ice (Figure 34) (Stokes & Clark, 1999).

The depression follows the outline of the BFC which is proposed to have acted as a weakness zone, prone to more intense glacial erosion than the surroundings (section 3.2.3 and 3.2.4) therefore forming a smooth elongated depression along in the direction of ice flow. The lower basal drag within the depression would have promoted fast flowing ice (Winsborrow et al., 2016).

Subglacial meltwater could also have contributed to the formation of the elongated depression and to the acceleration of ice flow within it once formed. A similar feature has been interpreted to exist at the base of the Greenland Ice Sheet and is suggested to be a paleofluvial mega-canyon (Bamber et al., 2013). The mega-canyon is at least 750 km long, ~ 800 m deep and ~10 km wide and has a meandering path. It has been described to be similar to the Grand Canyon, just half the depth in some areas. Interpreted to have acted as a mega subglacial channel, this feature would have efficiently drained meltwater from the base of the Greenland Ice Sheet over the full glacial cycle (Bamber et al., 2013). The meltwater canyon has therefore been active both during glacial and interglacial periods and has played an important role in draining meltwater from the Greenland ice sheet.

The elongated depression in our study is measured to be > 28 km long, 6,6 km wide and a negative relief of 35 ms (~ 35 meter) and therefore has a similar scale to the mega-canyon described by Bamber et al., (2013). Also, they both appear in a glaciated environment on continental shelves and have a similar cross profile. Unlike the mega channel described by Bamber et al, (2013), we observe landforms associated with glacial erosion within and along the elongated depression (section 3.2.5 and 3.2.6), and therefore link its formation to glacial erosion, rather than pre-glacial fluvial erosion as in the Greenland example. The elongated depression follows the outline of the BFC, a natural location for a meltwater channel as it is a weakness zone and thus prone to erosion compared to the surroundings. It is therefore suggested that the weakness zone of the BFC started as a small depression, the excavation of which was thereafter accelerated by subglacial meltwater and glacial erosion and formed the elongated depression on URU.

High water-pressure fluctuations underneath glaciers have also been suggested to accelerate rock fracturing (Iverson, 1991). This would give a positive feedback for glacial erosion within the elongated depression and thus contributed to a higher rate of erosion. Warm based glacier with subglacial water has been suggested contribute to less basal friction and increased ice flow velocity (Weertman & Birchfield, 1982).

4.1.3 Contrasting ice flow velocities on URU

The landforms that we observed on URU provide evidence for variations in ice flow velocity at the bed of the Bjørnøyrenna ice stream. The bedrock ridges mapped across the eastern parts of the dataset represent a relatively rough ice stream bed with relatively high frictional resistance to ice flow. We see no landforms indicative of streaming ice flow associated with these bedrock ridges. It is therefore proposed that this area experienced slower ice flow velocities (Figure 54 and 55). In contrast, the bathymetry within the elongated depression is more smooth, providing less basal frictional resistance to ice flow. Evidence for fast ice flow in this area is also provided by the presence of MSGs, which have been observed forming beneath contemporary ice streams (King et al., 2009). We therefore suggest that streaming flow velocities operated within the elongated depression (Figure 54 and 55).

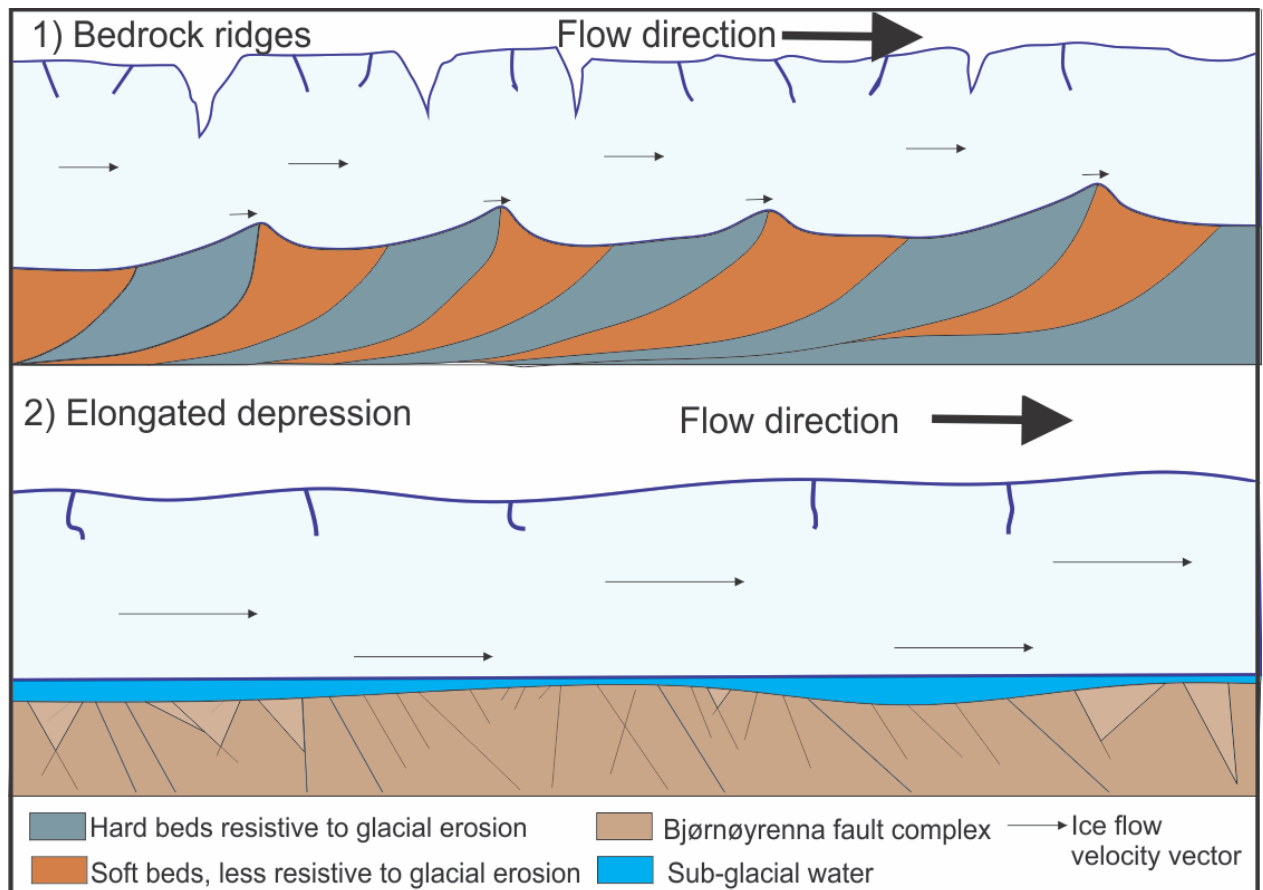


Figure 54 Conceptual model illustrating difference in ice flow velocity over 1) bedrock ridges vs 2) the elongated depression

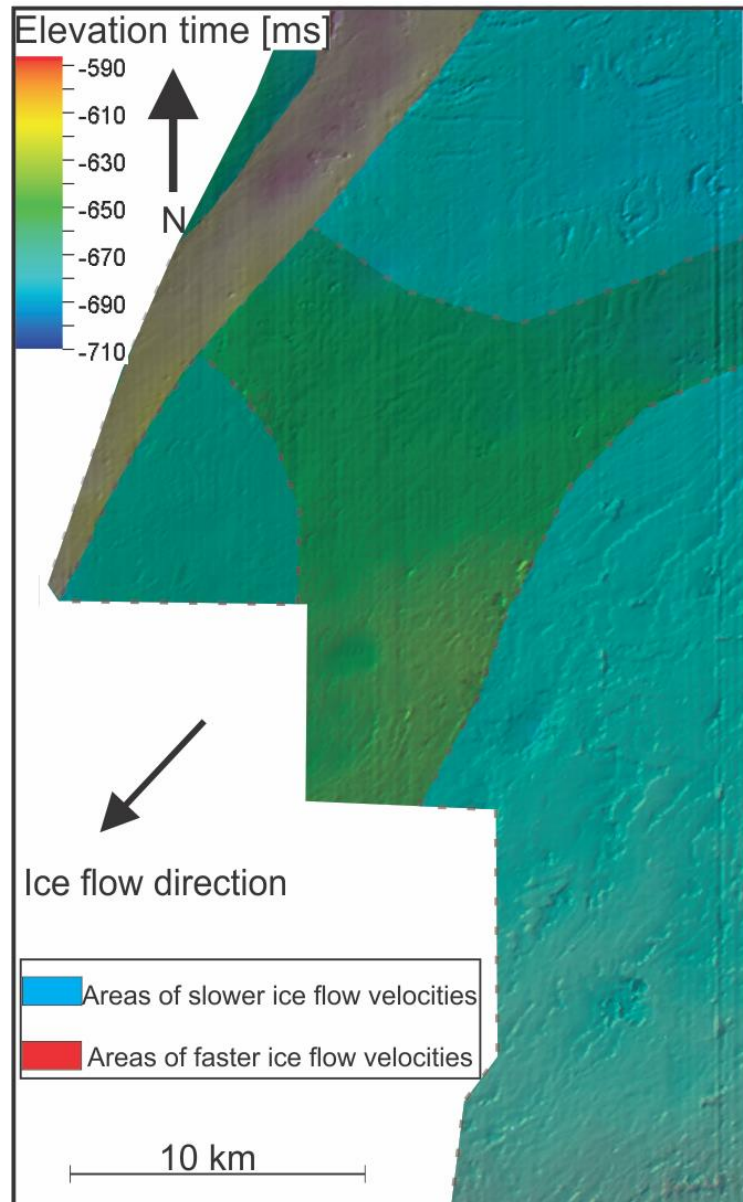


Figure 55 Conceptual model of ice flow velocities on the URU surface

4.1.4 Line of depressions and MSGL on the Intra Quaternary horizon

We suggest two possible formation mechanisms for the line of depressions mapped on the intra Quaternary horizon (section 3.4.6): glacitectonic erosion or blow-out craters from gas hydrate destabilization.

The first interpretation of the line of depressions are from glacitectonic processes.

Glacitectonic processes are defined as the large scale displacement of sub and pro glacial material, where both ductile and brittle deformation of sediment and/or bedrock may occur (Benn & Evans, 2014). Rafts and megablocks are slabs of unconsolidated strata, transported

from their original position by glacier erosion and could be a plausible explanation for this feature. For this process to happen, freezing-on of sediments and/or bedrock to the glacier bed is required. In this case the formation of gas hydrates under the glacier has been suggested to cause freeze-on of subglacial sediments which have been plucked from the URU and deposited further down-stream. Observed under the line of depressions are several areas of acoustic masking as well as a strong negative amplitude reflector (Figure 49). Acoustic masking is an indication of fluid migration and the strong negative amplitude is characteristic for hydrocarbon deposits. These observations are consistent with till stiffening due to the formation of gas hydrates and freeze-on of gas hydrate hosting sediments and bedrock to the base of the ice sheet. Similar depressions have been observed on intra Quaternary horizons interpreted by Andreassen & Winsborrow, (2009) (Figure 57), in outer Bjørnøyrenna, close to the palaeo-shelf break. Here a -4 km wide 12 km long zone of depressions, orientated in a north-east to south-west direction has been mapped (Andreassen & Winsborrow, 2009) (Figure 57). These are comparable in size and form to the line of depression we see on the intra Quaternary horizon which is 13,2 km long and up to 1,2 km wide. It also has a similar north-east south-west orientation (Figure 49). Andreassen and Winsborrow (2009) interpret the depressions to be areas where subglacial sediment blocks and rafts have been removed glacitectonically and deposited further downstream. They propose that the freezing of necessary to induce glacitectonic erosion was triggered by sediment dewatering. We believe a similar mechanism was responsibility for the formation of the line of depressions in our dataset, however we propose that subglacial gas hydrate formation was responsible for the freeze-on of sediments/bedrock to the base of the glacier in our case.

Till stiffening and freeze-on due to gas hydrate formation are proposed due to indications of hydrocarbons and fluid flow associated with the depressions. Due to higher pressure and lower temperatures during glacial events described in section 4.1.1 (bedrock ridges on URU) it is likely that this area held gas hydrates when Bjørnøyrenna was glaciated. The gas hydrates then froze on to the base of the ice sheet and large chunks of the sedimentary bedrock were plucked and transported further downstream as the ice stream moved on. The fact that the depressions are oriented in a line could be due to local fluid flow along underlying pre-existing faults (Figure 49), or could merely reflect the direction of ice flow. If so, this could then resulted in depressions within a line on the Intra-Quaternary horizon. As the ice sheet melted and thinned, the stability conditions for subglacial gas hydrates would reduce, with

increasing temperatures and decreasing pressure. Subglacial gas hydrates may have destabilized, giving the situation we see today with free gas seeping through the Quaternary sediment package which can be seen as acoustic masking in the seismic profile (Figure 49 profile b-b').

The second possible formation mechanism relates to blow-out craters following gas hydrate destabilization. Such craters have been described to form during and after a glacial event. At a glacial stage, gas hydrates form under the ice sheet due to the right temperature and pressure, as well as free gas migration from deeper reservoirs. As the ice sheet melts, the gas hydrate stability zone gets thinner, but free gas continues to migrate upwards toward the gas hydrates. Pressurized gas accumulates and may form a gas hydrate pingo. A crater may form when the pressure of the free gas exceeds the strength of the gas hydrate causing an explosive blow-out (Andreassen et al., 2017). Such blow-out craters have been observed on the seafloor on the northern flank of Bjørnøyrenna about 300 km upstream from our study area. The features have similarities to the depressions observed on the intra Quaternary horizon (Figure 56). The craters observed in Bjørnøyrenna are described to be from 300 to 1000 m in diameter and up to 30 m deep (Andreassen et al., 2017) incised into soft bedrock. The depressions found on the intra Quaternary horizon in our study area are measured to be from 200 – 800 m in diameter and 16 ms (~16 m) deep. 16 ms translate to 16 m assuming the acoustic velocity in quaternary sediments to be 2000 m/s (Andreassen et al., 2007). On a seismic profile along the depressions, similar seismic facies and indications for gas can be seen. We observe bright spots and areas of acoustic masking associated with the depressions (Figure 45 profile b-b'). From Karin Andreassen et al., (2017) high amplitude and chaotic reflectors have been interpreted as gas chimneys underneath the blow-out craters (Figure 56). In addition, they observe gas seepage in the water column, which confirms the gas content within the underlying sediments (Figure 56). Different from the blow-out craters of Andreassen et al (2017) is that the depressions we observe on the intra Quaternary horizon collectively form a linear pattern which is consistent with palaeo- ice flow direction (Table 2). However the blow-out craters observed on the seabed by K Andreassen et al., (2007) are spread randomly over a larger area and do not indicate any linear flow direction. The two landforms have geometrical similarities and similarities regarding seismic facies, however the linear appearances of the line of depressions favor a glacitectonic formation mechanism rather than blow-out craters.

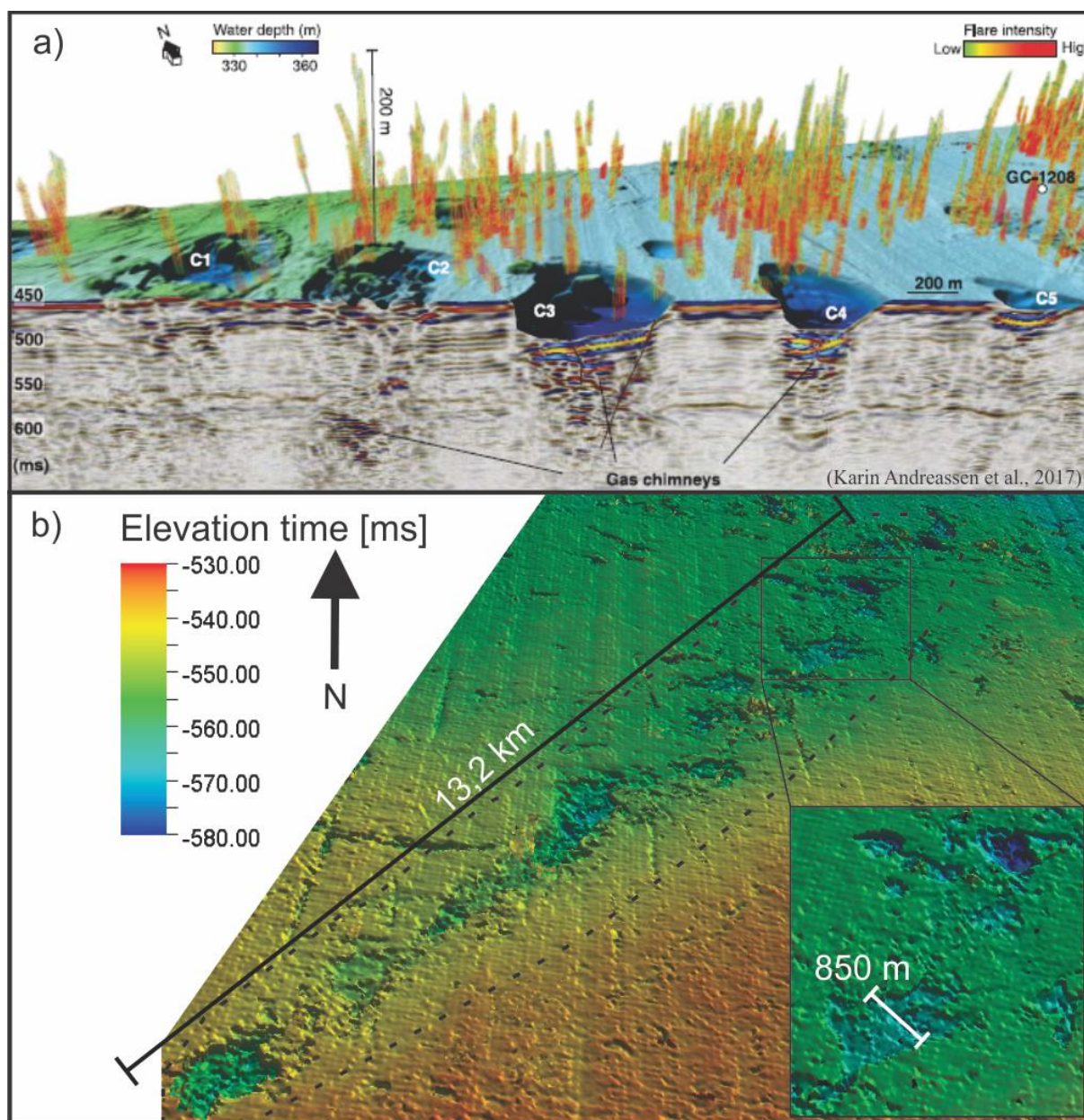


Figure 56 Blow-out craters observed on the seabed of Bjørnøyrenna (Andreassen et al., 2017) compared to the line of depressions on the intra Quaternary horizon within the study area. See Figure 49 for seismic profiles along the line of depressions.

Regarding glacier dynamics and ice flow velocities, both these theories suggest that there were gas hydrates abundant during LGM and parts of the deglaciation. If the hydrates were frozen to the base of the ice stream, this means that there was a cold basal regime in this area of the ice stream for at least part of its operation (Figure 58).

Located about 10 km north from the line of depressions are north-east to south-west oriented streamlined bedforms interpreted to be MSGL (section 3.4.3 and 3.4.4) (Figure 48). The MSGL have a similar orientation to the line of depressions, just more oriented towards south (Figure 57). MSGL has been observed within Bjørnøyrenna in several other studies e.g (Andreassen & Winsborrow, 2009) (Patton et al., 2017) (Rüther et al., 2011). MSGL with the same orientation as observed on the intra Quaternary horizon in this thesis have been mapped on a intra Quaternary horizon on the shelf break within Bjørnøyrenna (Figure 57, lineation set 2) (Andreassen & Winsborrow, 2009). This paper also observed a zone of depressiona with the same orientation as MSGL set 2 (Figure 57 zone of depressions). The zone of depressions are overlain by MSGL, and they suggest that this pattern indicate that a slowdown or quiescence was followed by reactivation and fast flowing ice (Andreassen & Winsborrow, 2009). The same has been observed on the intra Quaternary horizon in this thesis. The MSGL are observed just 10 km away from a line of depressions. However, the line of depression sis not overlain by MSGL and thus the chronology of the two landforms cannot be determined. The two landforms do however indicate constrasts in basal thermal regime and ice flow velocities (Figure 58) and we suggest that area with MSGL hs experienced fast flowing ice, while the line of depressions indicate a cold base regime and therefore indicate slower or standstill ice (Figure 58).

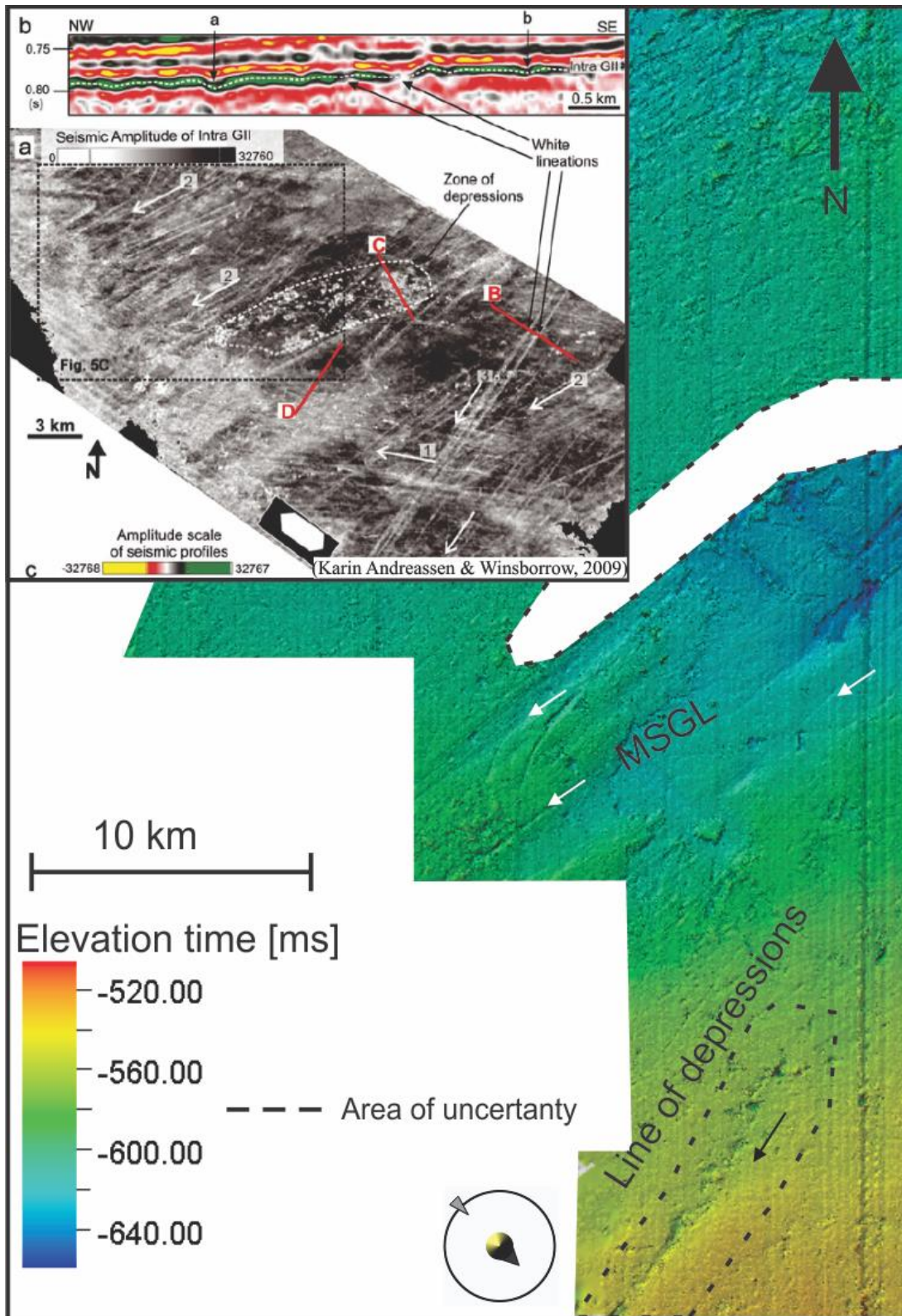


Figure 57 MSGL and line of depressions on the intra Quaternary horizon compared to MSGL and zone of depressions mapped by (Andreassen & Winsborrow, 2009). Lineation set 2 has the same orientation as the mapped MSGL on the intra Quaternary horizon.

To summarize the intra Quaternary horizon, the area containing MSGL has been suggested to reflect high ice flow velocities (Figure 58: warm base regime). The line of depressions located 10 km south of the MSGL is interpreted to be an area with slower ice flow velocities or even standstills (Figure 58: cold base regime). The difference in orientation might indicate that they formed at different times (Figure 58). For the rest of the intra Quaternary horizon surface there are no landforms reflecting ice flow velocity. However, in the northern parts of the surface there is observed curved lineations interpreted as iceberg ploughmarks. These have been linked to identical ploughmarks observed on the seabed surface. It could therefore be that ploughmarks have overprinted other landforms reflecting glacial dynamics for the rest of the intra Quaternary horizon surface.

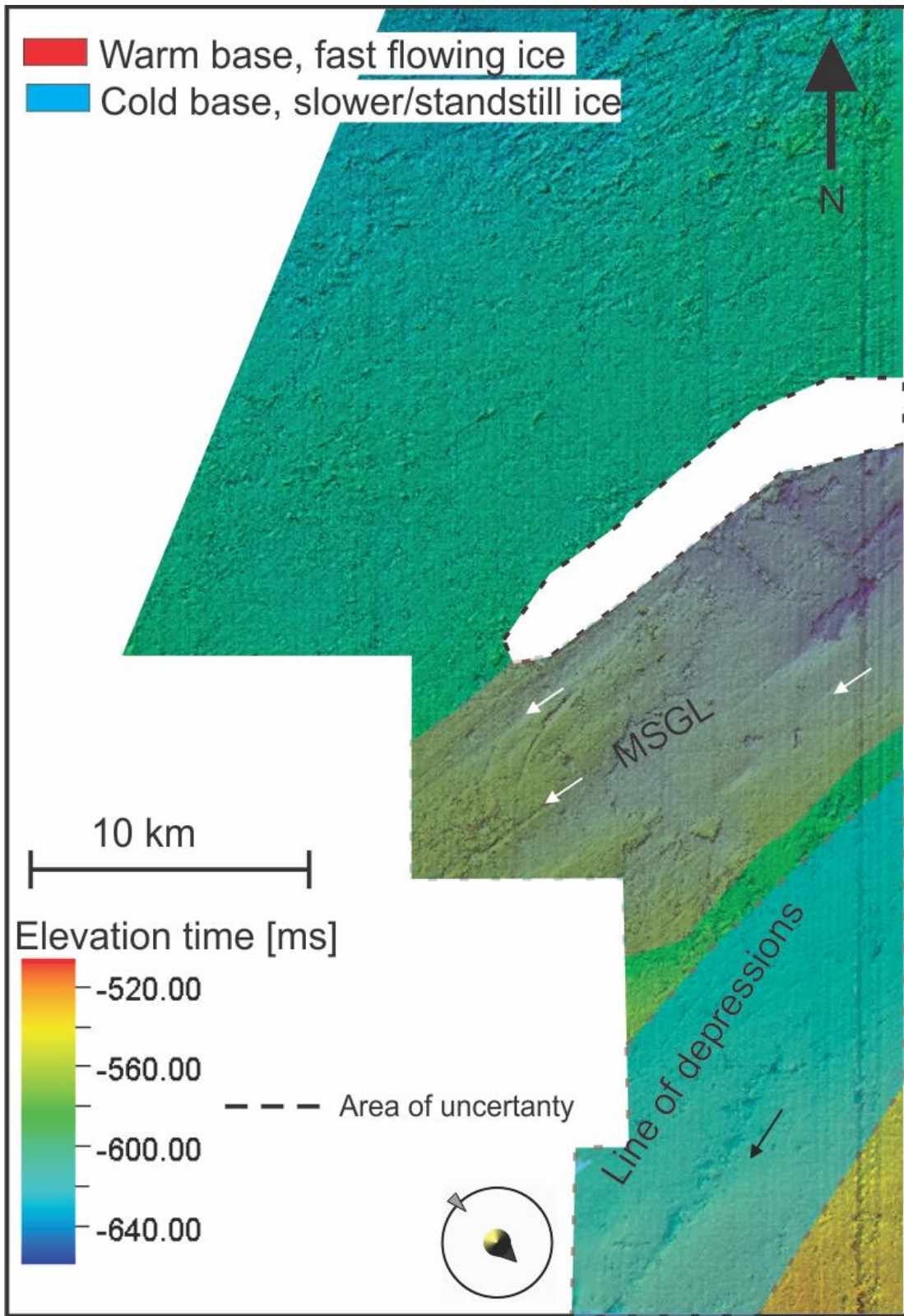






Figure 58 Conceptual model of ice flow and thermal regimes on the intra Quaternary horizon

4.2 Regional ice dynamics of the Bjørnøyrenna ice stream

In this chapter, the mapped landforms of the study area will be compared to earlier studies on glacier dynamics and deglaciation of the Bjørnøyrenna ice stream. A schematic table of the mapped landforms has been made to be able to compare ice flow direction on the different surfaces to earlier studies (Table 3). Within the study area, the seabed surface is intensely iceberg scoured and no landforms providing evidence for ice flow directions were mapped. The seabed surface is therefore not included in the interpretation of ice flow direction of the study area.

Tabell 3 Landforms indicating ice flow directions on the different surfaces

Landform	Surface	Indication of ice flow direction	Thermal regime
Ice berg scour marks	Seabed	No landforms reflecting ice flow direction	
MSGSL	Intra-Quaternary Horizon		Warm
Line of depressions	Intra-Quaternary Horizon		Cold
Elongated - depression	URU		Warm
Streamlined Lineations	URU		Warm

4.2.1 URU

On the URU surface, two of the mapped landforms indicated ice flow direction. These are the elongated depression and the streamlined lineations interpreted as MSGSL. Both landforms have the same orientation north-east to south-west (Table 3). MSGSL with similar orientation have been observed on URU about 50 km up stream in Bjørnøyrenna (Piasecka et al., 2016).

In that dataset five sets of MSGL were mapped on URU, two of which have a very similar orientation to those mapped in URU within our datasets, where flow set two has the most similar orientation to those mapped on the URU surface in this thesis (Figures 59 and 60). Piasecka et al. (2016) interpreted the oldest MSGLs (flow set 1) to have formed during the LGM, when the Bjørnøyrenna ice stream reached its maximum extent, terminating at the shelf edge. They interpreted, MSGL flow sets 2 – 5 as ephemeral periods of ice streaming prior to the beginning of the deglaciation, when the position of the ice stream fluctuated slightly within Bjørnøyrenna (Piasecka et al., 2016). The MSGLs and elongated depression observed on URU in this thesis have an orientation very similar to flow set 2 of Piasecka et al. (2016), and we therefore interpreted these landforms to have formed during the initial phase of deglaciation of the Bjørnøyrenna ice stream, when it experienced initial rapid retreat from its maximum shelf edge position about 19 Ka BP.

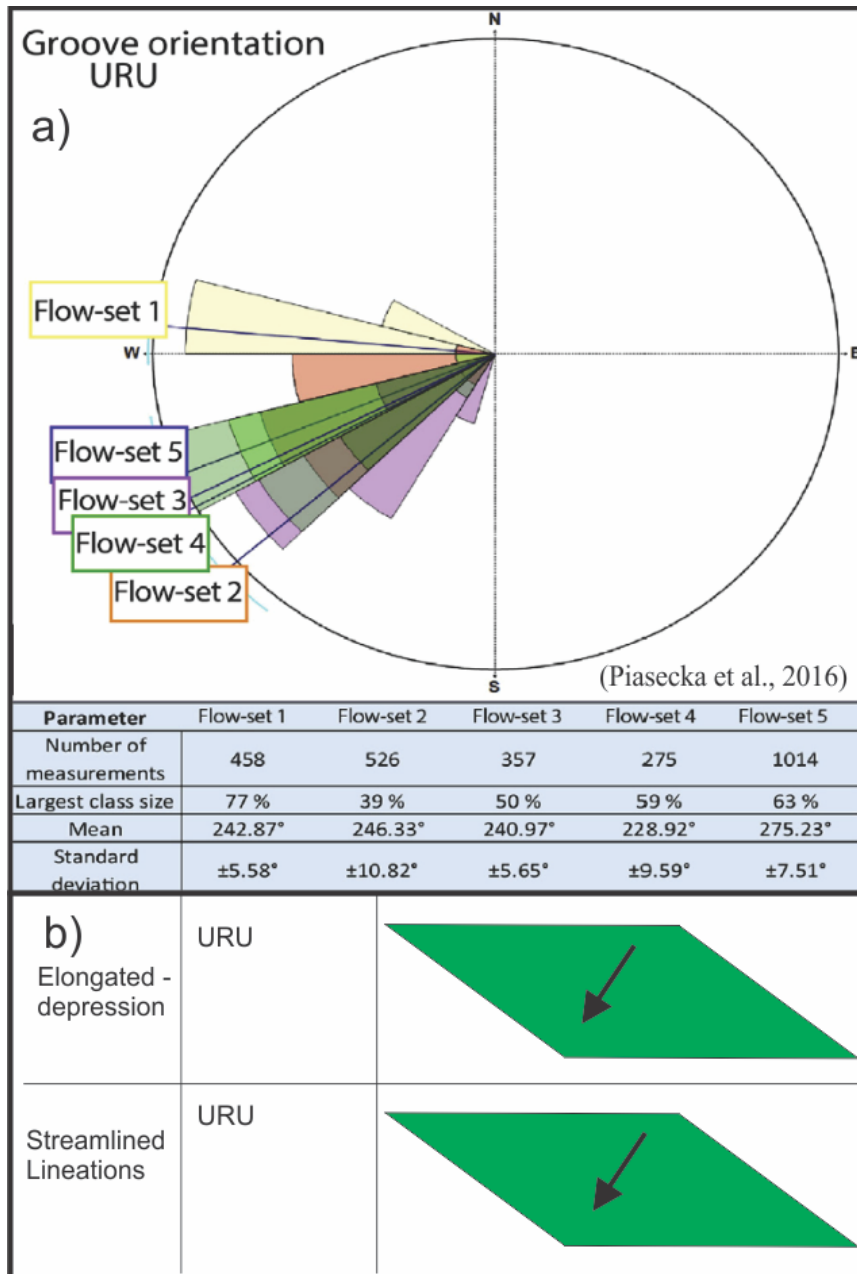


Figure 59 comparing MSGL flowsets interpreted by Piasecka et al. (2016) (a) and ice flow direction of the mapped landforms on URU in our study area (b). Figure modified from Piasecka et al., (2016)

4.2.2 Intra Quaternary horizon:

On the intra Quaternary horizon there are two landforms indicating ice flow direction. MSGL and the line of depressions. However, different from the URU surface, these two landforms indicate slightly different flow directions and different basal thermal regimes (Table 3). The MSGL and the line of depressions observed on the intra Quaternary horizon have similarities to two other observed MSGL sets within the Bjørnøyrenna ice stream.

On the southern flank of the Bjørnøyrenna trough mouth fan three intra Quaternary horizons which were located on the palaeo-shelf, have been mapped where several sets of MSGL and megablocks and rafts have been observed with different orientations (Figure 57) (Andreassen & Winsborrow, 2009). MSGL set 2 from this study are observed on a buried seismic horizon GII (Figure 57). They have the same north east to southwest orientation as the MSGL observed on the intra Quaternary horizon (Figure 57). As mentioned in section 4.1.4 a zone of depressions is observed on the same GII surface as the MSGLs, interpreted by Karin Andreassen & Winsborrow, (2009). On the intra Quaternary horizon in our study, MSGL and a line of depressions are also observed together on the same horizon similar to the observation by Karin Andreassen and Winsborrow, (2009). These two horizons thus show similar content of landforms and could therefore indicate similar or the same ice streaming conditions. However, horizon GII is interpreted to have formed between 1,3 Ma – 200 Ka BP (Andreassen & Winsborrow, 2009), and they represent flow conditions of a pre-Late Weichselian Bjørnøyrenna ice stream. The MSGL and line of depressions we observe are located on an intra Quaternary horizon on the Barents Sea shelf within Bjørnøyrenna ice stream and interpreted to be formed post LGM (~22 Ka BP). However, what is interesting is that the same composition of landforms are found on the two different horizons and with similar orientation. This indicates that Bjørnøyrenna ice stream have had similar orientation and ice streaming pattern over multiple glacial advances.

MSGL interpreted by Winsborrow et al. (2010) on the seabed surface of the outer parts of the Bjørnøyrenna ice stream show similar flow direction as we observe on the intra Quaternary horizon. Here flow set 13 matches the orientation of the MSGL and the line of depressions observed on the intra Quaternary horizon in our dataset (Figure 60). From Figure 60 flowset 13 terminates outside of our area of this thesis (Figure 60). Higher rates of sedimentation may have buried the MSGL in this area, and is therefore seen on a buried surface (intra Quaternary horizon) instead of the seabed. Flow set 13 has similar orientation to the orientation of the line of depression and the MSGL on the intra Quaternary horizon (Figure 60). Flow set 13 overprint and terminate at the outer grounding zone wedge of Bjørnøyrenna and have been interpreted to represent stage 2 of the deglaciation (~17 cal ka BP), characterized by retreat and subsequent readvance of the Bjørnøyrenna ice stream to the outermost ground zone wedge (Winsborrow et al., 2010). The line of depressions which has been suggested to represent a cold base thermal regime and standstill/slow ice flow velocities and can therefore

be linked to a period of standstill during stage 2 of the deglaciation, perhaps associated with the formation of the grounding zone wedge. Whilst the MSGL could relate to the readvance preceding the stillstand. However, the MSGL we observe on the intra Quaternary horizon appear on a different horizon than flow set 13 and it is also plausible that they represent different ice streaming events. If that is the case, the MSGL observed in this thesis are then older than flow set 13 interpreted by Winsborrow et al., (2010).

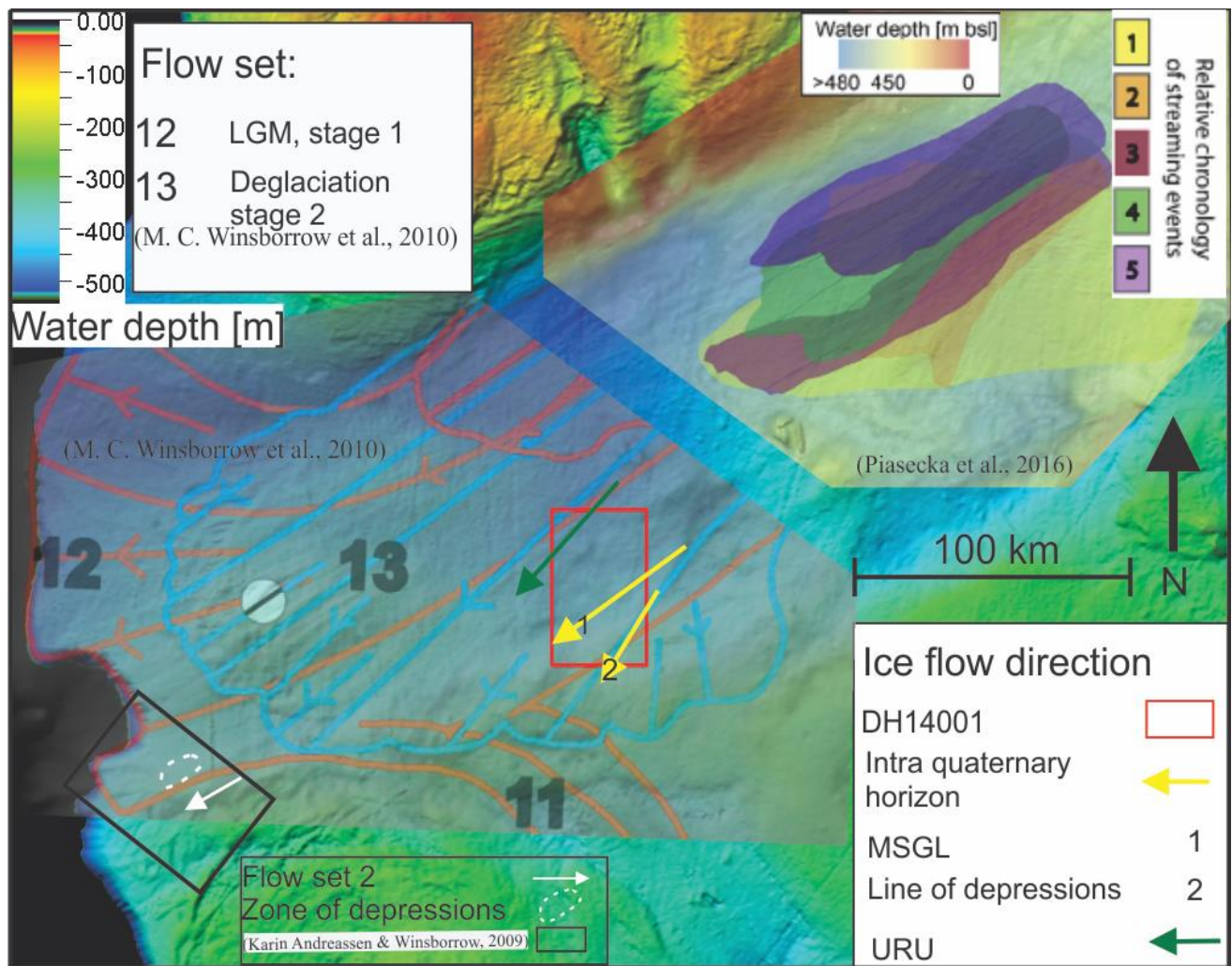


Figure 60 Ice flow direction from the mapped landforms on URU and the Intra Quaternary horizon surface compared to (Winsborrow et al., 2010), (Andreassen & Winsborrow, 2009) and (Piasecka et al., 2016). Ice flow direction of the URU is linked to flow set 2 mapped on URU (Piasecka et al., 2016). Ice flow direction on the Intra Quaternary horizon is linked to flow set 13 from (Winsborrow et al., 2010) and flow set 2 from (Andreassen & Winsborrow, 2009). Flow set 2 and zone of depression by Andreassen & Winsborrow, (2009) is viewed in Figure 57.

Regarding the deglaciation of our study area, marine based ice streams in the Arctic have been described to be rapid but with readvances and standstills (Rebesco et al., 2011). This has been recorded by core sampling and mapping of landforms in fjords that hosted marine based

glaciers during the LGM and the deglaciation (Hughes et al., 2016). In Bjørnøyrenna, mapping of several sets of MSGL and GZW led to the suggestion that the deglaciation of SW Barents Sea and Bjørnøyrenna happened in five stages (section 1.4.4) (Winsborrow et al., 2010). The 3D seismic dataset used in this thesis lies in between two of the grounding zone wedges in Bjørnøyrenna. These two grounding zone wedges are suggested to represent the ice front at stage 2 and 3 of the deglaciation which are inferred to be between ~17 and 16 cal ka BP (Winsborrow et al., 2010).

A different study combined empirical data from various studies to reconstruct the deglaciation of the last Eurasian ice sheet suggested that Bjørnøyrenna ice stream deglaciated between ~18 – 16 Ka years ago (Hughes et al., 2016). On the seabed surface of the 3D seismic dataset there are no landforms that suggest a standstill or readvance. It is therefore believed that the study area was deglaciated relatively rapid and continuous between stage 2 and 3 somewhere between ~18 and 16 ~ cal ka BP.

5 Conclusion

3D seismic data from Bjørnøyrenna has been used to study glacier dynamics and to assess any connections to fluid flow, shallow gas accumulations and gas hydrate formation. Three seismic surfaces were interpreted: URU, an Intra Quaternary horizon and the seafloor. Based on mapping of landforms identified on these surfaces, and the investigation of seismic attributes, the following conclusions were made:

- Mega scale glacial lineations (MSGSL) are observed both on URU and the Intra Quaternary horizon. These were interpreted to indicate, different ice streaming events in Bjørnøyrenna, at different times. On URU the lineations are oriented north-east to south-west and are suggested to have been formed during the initial deglaciation, at about 19 ka BP. On the intra Quaternary horizon the mega scale glacial lineations are also oriented broadly north-east to south-west, but more towards west compared to those we see on URU. These lineations have been proposed to have formed when the Bjørnøyrenna Ice Stream terminated at the outer grounding zone of Bjørnøyrenna which is dated to 17 ka BP.
- On the intra Quaternary horizon, MSGSL and a line of depressions are observed within a distance of 10 km. The line of depressions has been interpreted to have formed glacitectonically. These landforms therefore reflect different glacial thermal regimes (MSGSL: warm-based ice and line of depression: cold-based ice) and also respectively indicate fast flowing ice and slower ice.
- An elongated depression following the outline of the Bjørnøyrenna Fault Complex on URU is suggested to have worked as a subglacial meltwater channel during glacial periods. It is also suggested that basal drag was lower within the meltwater channel increasing ice flow velocities in this area compared to the surroundings.
- Circular depressions have been observed on URU. Three interpretations have been suggested:
 1. Circular depressions formed by density differences as a post depositional process
 2. Subglacial pressure points
 3. Subglacial lakes
- Indications of shallow gas have been observed on both URU and the intra Quaternary horizon. These are interpreted to indicate fluid flow, migrating from deeper

hydrocarbon reservoirs. On URU, indications of shallow gas are associated with circular depressions and along the flanks of the elongated depression. On the Intra Quaternary horizon indications of fluid migration are associated with the line of glacitectonic depressions oriented in the palaeo-ice flow direction.

- Due to higher pressure and lower temperature during glacial events, gas hydrates are suggested to have formed in the study area during the late Weichselian glaciation and could have had an effect on glacier dynamics. Gas hydrate formation is suggested to have played a role in the creation of the line of depressions on the intra Quaternary horizon. Two potential formation mechanisms are proposed: blow-out craters formed by the depressurization of gas hydrates on deglaciation, or glacitectonic processes facilitated by subglacial gas hydrate formation.

References

- Andreassen, K., Hubbard, A., Winsborrow, M., Patton, H., Vadakkepuliymbatta, S., Plaza-Faverola, A., . . . Mattingsdal, R. (2017). Massive blow-out craters formed by hydrate-controlled methane expulsion from the Arctic seafloor. *Science*, *356*(6341), 948-953.
- Andreassen, K., & Winsborrow, M. (2009). Signature of ice streaming in Bjørnøyrenna, Polar North Atlantic, through the Pleistocene and implications for ice-stream dynamics. *Annals of Glaciology*, *50*(52), 17-26.
- Andreassen, K., Ødegaard, C., & Rafaelsen, B. (2007). Imprints of former ice streams, imaged and interpreted using industry three-dimensional seismic data from the southwestern Barents Sea. *Geological Society, London, Special Publications*, *277*(1), 151-169.
- Badley, M. E., & Gibson, B. (1987). Practical Seismic Interpretation by Michael E. Badley. In: Acoustical Society of America.
- Bamber, J. L., Siegert, M. J., Griggs, J. A., Marshall, S. J., & Spada, G. (2013). Paleofluvial mega-canyon beneath the central Greenland ice sheet. *Science*, *341*(6149), 997-999.
- Bellwald, B., Planke, S., Lebedeva-Ivanova, N., Piasecka, E. D., & Andreassen, K. (2019). High-resolution landform assemblage along a buried glacio-erosive surface in the SW Barents Sea revealed by P-Cable 3D seismic data. *Geomorphology*, *332*, 33-50.
- Benn, D., & Evans, D. J. (2014). *Glaciers and glaciation*: Routledge.
- Bennett, M. R. (2003). Ice streams as the arteries of an ice sheet: their mechanics, stability and significance. *Earth-Science Reviews*, *61*(3-4), 309-339.
- Brendryen, J., Hafliðason, H., Yokoyama, Y., Haaga, K. A., & Hannisdal, B. (2020). Eurasian Ice Sheet collapse was a major source of Meltwater Pulse 1A 14,600 years ago. *Nature Geoscience*, 1-6.
- Brown, A. R. (2011). *Interpretation of three-dimensional seismic data*: Society of Exploration Geophysicists and American Association of Petroleum . . .
- Butt, F., Elverhøi, A., Solheim, A., & Forsberg, C. (2000). Deciphering Late Cenozoic development of the western Svalbard Margin from ODP Site 986 results. *Marine Geology*, *169*(3-4), 373-390.
- Butt, F. A., Drange, H., Elverhøi, A., Otterå, O. H., & Solheim, A. (2002). Modelling Late Cenozoic isostatic elevation changes in the Barents Sea and their implications for oceanic and climatic regimes: preliminary results. *Quaternary Science Reviews*, *21*(14-15), 1643-1660.
- Chand, S., Mienert, J., Andreassen, K., Knies, J., Plassen, L., & Fotland, B. (2008). Gas hydrate stability zone modelling in areas of salt tectonics and pockmarks of the Barents Sea suggests an active hydrocarbon venting system. *Marine and Petroleum Geology*, *25*(7), 625-636.
- Chand, S., Thorsnes, T., Rise, L., Brunstad, H., Stoddart, D., Bøe, R., . . . Svolsbru, T. (2012). Multiple episodes of fluid flow in the SW Barents Sea (Loppa High) evidenced by gas flares, pockmarks and gas hydrate accumulation. *Earth and Planetary Science Letters*, *331*, 305-314.
- Chopra, S., & Marfurt, K. J. (2005). Seismic attributes—A historical perspective. *Geophysics*, *70*(5), 3S0-28S0.
- Cosgrove, J. W., & Hillier, R. D. (1999). Forced-fold development within Tertiary sediments of the Alba Field, UKCS: evidence of differential compaction and post-depositional sandstone remobilization. *Geological Society, London, Special Publications*, *169*(1), 61-71.

- Dowdeswell, J., & Fugelli, E. (2012). The seismic architecture and geometry of grounding-zone wedges formed at the marine margins of past ice sheets. *Bulletin*, 124(11-12), 1750-1761.
- Esteves, M., Bjarnadóttir, L. R., Winsborrow, M. C., Shackleton, C. S., & Andreassen, K. (2017). Retreat patterns and dynamics of the Sentralbankrenna glacial system, central Barents Sea. *Quaternary Science Reviews*, 169, 131-147.
- Evans, D. J., & Wilson, S. B. (2006). Scottish Landform example 39: The lake of Menteith glacitectonic hill - hole pair. *Scottish Geographical Journal*, 122(4), 352-364.
- Faleide, J. I., Gudlaugsson, S. T., & Jacquart, G. (1984). Evolution of the western Barents Sea. *Marine and Petroleum Geology*, 1(2), 123-150.
- Faleide, J. I., Vågnes, E., & Gudlaugsson, S. T. (1993). Late Mesozoic-Cenozoic evolution of the south-western Barents Sea in a regional rift-shear tectonic setting. *Marine and Petroleum Geology*, 10(3), 186-214.
- Gabrielsen, R. H., Grunnaleite, I., & Rasmussen, E. (1997). Cretaceous and tertiary inversion in the Bjørnøyrenna Fault Complex, south-western Barents Sea. *Marine and Petroleum Geology*, 14(2), 165-178.
- Hogan, K., Dowdeswell, J., Noormets, R., Evans, J., Cofaigh, C. Ó., & Jakobsson, M. (2010). Submarine landforms and ice-sheet flow in the Kvitøya Trough, northwestern Barents Sea. *Quaternary Science Reviews*, 29(25-26), 3545-3562.
- Hughes, A. L., Gyllencreutz, R., Lohne, Ø. S., Mangerud, J., & Svendsen, J. I. (2016). The last Eurasian ice sheets—a chronological database and time - slice reconstruction, DATED - 1. *Boreas*, 45(1), 1-45.
- Iverson, N. R. (1991). Potential effects of subglacial water-pressure fluctuations on quarrying. *Journal of Glaciology*, 37(125), 27-36.
- Jakobsson, M., Andreassen, K., Bjarnadóttir, L. R., Dove, D., Dowdeswell, J. A., England, J. H., . . . Jennings, A. (2014). Arctic Ocean glacial history. *Quaternary Science Reviews*, 92, 40-67.
- Kearey, P., Brooks, M., & Hill, I. (2013). *An introduction to geophysical exploration*: John Wiley & Sons.
- King, E. C., Hindmarsh, R. C., & Stokes, C. (2009). Formation of mega-scale glacial lineations observed beneath a West Antarctic ice stream. *Nature Geoscience*, 2(8), 585-588.
- Knies, J., Matthiessen, J., Vogt, C., Laberg, J. S., Hjelstuen, B. O., Smelror, M., . . . Vorren, T. O. (2009). The Plio-Pleistocene glaciation of the Barents Sea–Svalbard region: a new model based on revised chronostratigraphy. *Quaternary Science Reviews*, 28(9-10), 812-829.
- Kvenvolden, K. A. (1988). Methane hydrate—a major reservoir of carbon in the shallow geosphere? *Chemical geology*, 71(1-3), 41-51.
- Kvenvolden, K. A., & McMennamin, M. A. (1980). Hydrates of natural gas: a review of their geologic occurrence.
- Landvik, J. Y., Bondevik, S., Elverhøi, A., Fjeldskaar, W., Mangerud, J., Salvigsen, O., . . . Vorren, T. O. (1998). The last glacial maximum of Svalbard and the Barents Sea area: ice sheet extent and configuration. *Quaternary Science Reviews*, 17(1-3), 43-75.
- Lasabuda, A., Laberg, J. S., Knutsen, S.-M., & Safronova, P. (2018). Cenozoic tectonostratigraphy and pre-glacial erosion: A mass-balance study of the northwestern Barents Sea margin, Norwegian Arctic. *Journal of Geodynamics*, 119, 149-166.

- Liner, C. L. (1999). *Treatise of Petroleum Geology/Handbook of Petroleum Geology: Exploring for Oil and Gas Traps*. Chapter 12: Interpreting Seismic Data.
- Løseth, H., Gading, M., & Wensaas, L. (2009). Hydrocarbon leakage interpreted on seismic data. *Marine and Petroleum Geology*, 26(7), 1304-1319.
- MacAyeal, D. R., Bindschadler, R. A., & Scambos, T. A. (1995). Basal friction of ice stream E, West Antarctica. *Journal of Glaciology*, 41(138), 247-262.
- NPD. (2014). Exploration Well 7220/2-1. Retrieved from <https://factpages.npd.no/nb-no/wellbore/pageview/exploration/all/7558>
- NPD. (2018). Gotha discovery. Retrieved from <http://factpages.npd.no/ReportServer?/FactPages/PageView/discovery&rs:Command=Render&rc:Toolbar=false&rc:Parameters=f&NpdId=23761885&IpAddress=129.242.206.149&CultureCode=en>
- NPD. (2020). Kapp formation. Retrieved from <https://factpages.npd.no/nb-no/strat/pageview/litho/groups/79>
- Paterson, W. S. B. (2016). *The physics of glaciers*: Elsevier.
- Patton, H., Hubbard, A., Andreassen, K., Auriac, A., Whitehouse, P. L., Stroeven, A. P., . . . Hall, A. M. (2017). Deglaciation of the Eurasian ice sheet complex. *Quaternary Science Reviews*, 169, 148-172.
- Petersen, C. J., Bünz, S., Hustoft, S., Mienert, J., & Klaeschen, D. (2010). High-resolution P-Cable 3D seismic imaging of gas chimney structures in gas hydrated sediments of an Arctic sediment drift. *Marine and Petroleum Geology*, 27(9), 1981-1994.
- Piasecka, E. D., Winsborrow, M. C., Andreassen, K., & Stokes, C. R. (2016). Reconstructing the retreat dynamics of the Bjørnøyrenna Ice Stream based on new 3D seismic data from the central Barents Sea. *Quaternary Science Reviews*, 151, 212-227.
- Pigott, J. D., Kang, M.-H., & Han, H.-C. (2013). First order seismic attributes for clastic seismic facies interpretation: Examples from the East China Sea. *Journal of Asian Earth Sciences*, 66, 34-54.
- Ramberg, I. B., Bryhni, I., & Nøttvedt, A. (2007). *Landet blir til: Norges geologi*: Norsk geologisk forening.
- Rebesco, M., Liu, Y., Camerlenghi, A., Winsborrow, M., Laberg, J. S., Caburlotto, A., . . . Wardell, N. (2011). Deglaciation of the western margin of the Barents Sea Ice Sheet—A swath bathymetric and sub-bottom seismic study from the Kveithola Trough. *Marine Geology*, 279(1-4), 141-147.
- Rüther, D. C., Mattingsdal, R., Andreassen, K., Forwick, M., & Husum, K. (2011). Seismic architecture and sedimentology of a major grounding zone system deposited by the Bjørnøyrenna Ice Stream during Late Weichselian deglaciation. *Quaternary Science Reviews*, 30(19-20), 2776-2792.
- Shackleton, C. S., Winsborrow, M. C., Andreassen, K., Lucchi, R. G., & Bjarnadóttir, L. R. (2020). Ice - margin retreat and grounding - zone dynamics during initial deglaciation of the Storfjordrenna Ice Stream, western Barents Sea. *Boreas*, 49(1), 38-51.
- Sheriff, R. (1985). Aspects of seismic resolution: Chapter 1.
- Stickley, C. E., St John, K., Koç, N., Jordan, R. W., Passchier, S., Pearce, R. B., & Kearns, L. E. (2009). Evidence for middle Eocene Arctic sea ice from diatoms and ice-rafted debris. *Nature*, 460(7253), 376.
- Stokes, C. R. (2018). Geomorphology under ice streams: Moving from form to process. *Earth Surface Processes and Landforms*, 43(1), 85-123.
- Stokes, C. R., & Clark, C. D. (1999). Geomorphological criteria for identifying Pleistocene ice streams. *Annals of Glaciology*, 28, 67-74.

- Sættem, J. (1990). Glaciotectonic forms and structures on the Norwegian continental shelf: observations, processes and implications. *Norsk geologisk tidsskrift*, 70(2), 81-94.
- Sættem, J., Poole, D., Ellingsen, L., & Sejrup, H. (1992). Glacial geology of outer Bjørnøyrenna, southwestern Barents Sea. *Marine Geology*, 103(1-3), 15-51.
- Vadakkepuliyambatta, S., Chand, S., & Büinz, S. (2017). The history and future trends of ocean warming - induced gas hydrate dissociation in the SW Barents Sea. *Geophysical Research Letters*, 44(2), 835-844.
- Vorren, T., Lebesbye, E., Andreassen, K., & Larsen, K.-B. (1989). Glacigenic sediments on a passive continental margin as exemplified by the Barents Sea. *Marine Geology*, 85(2-4), 251-272.
- Vorren, T. O., & Laberg, J. S. (1996). Late glacial air temperature, oceanographic and ice sheet interactions in the southern Barents Sea region. *Geological Society, London, Special Publications*, 111(1), 303-321.
- Vorren, T. O., Landvik, J. Y., Andreassen, K., & Laberg, J. S. (2011). Glacial history of the Barents Sea region. In *Developments in Quaternary Sciences* (Vol. 15, pp. 361-372): Elsevier.
- Vorren, T. O., Lebesbye, E., & Larsen, K. B. (1990). Geometry and genesis of the glacigenic sediments in the southern Barents Sea. *Geological Society, London, Special Publications*, 53(1), 269-288.
- Weertman, J., & Birchfield, G. (1982). Subglacial water flow under ice streams and West Antarctic ice-sheet stability. *Annals of Glaciology*, 3, 316-320.
- Winsborrow, M., Andreassen, K., Hubbard, A., Plaza-Faverola, A., Gudlaugsson, E., & Patton, H. (2016). Regulation of ice stream flow through subglacial formation of gas hydrates. *Nature Geoscience*, 9(5), 370.
- Winsborrow, M. C., Andreassen, K., Corner, G. D., & Laberg, J. S. (2010). Deglaciation of a marine-based ice sheet: Late Weichselian palaeo-ice dynamics and retreat in the southern Barents Sea reconstructed from onshore and offshore glacial geomorphology. *Quaternary Science Reviews*, 29(3-4), 424-442.
- Winters, W. J., Pecher, I. A., Waite, W. F., & Mason, D. H. (2004). Physical properties and rock physics models of sediment containing natural and laboratory-formed methane gas hydrate. *American Mineralogist*, 89(8-9), 1221-1227.
- Worsley, D. (2008). The post-Caledonian development of Svalbard and the western Barents Sea. *Polar Research*, 27(3), 298-317.